STUDY OF PENETRATION PERFORMANCE OF OXIDE DISPERSION STRENGTHENED TUNGSTEN HEAVY ALLOYS FABRICATED BY CONVENTIONAL SINTERING

M.Tech Thesis

By

NISMATH V H

DEPARTMENT OF METALLURGY ENGINEERING AND MATERIALS SCIENCE

INDIAN INSTITUTE OF TECHNOLOGY INDORE

June 2022

STUDY OF PENETRATION PERFORMANCE OF OXIDE DISPERSION STRENGTHENED TUNGSTEN HEAVY ALLOYS FABRICATED BY CONVENTIONAL SINTERING

A Thesis

Submitted in partial fulfillment of the requirements for the award of the degree

of

Master of Technology

by

NISMATH V H

DEPARTMENT OF METALLURGY ENGINEERING AND MATERIALS SCIENCE

INDIAN INSTITUTE OF TECHNOLOGY INDORE

June 2022

INDIAN INSTITUTE OF TECHNOLOGY INDORE

CANDIDATE'S DECLARATION

I hereby certify that the work which is being presented in the thesis entitled "**Study of penetration performance of oxide dispersion strengthened tungsten-heavy alloys fabricated by conventional sintering"** in the partial fulfillment of the requirements for the award of the degree of **MASTER OF TECHNOLOGY** and submitted in the **DEPARTMENT OF METALLURGY ENGINEERING AND MATERIALS SCIENCE, Indian Institute of Technology Indore**, is an authentic record of my own work carried out during the time period from August 2021 to May 2022 under the supervision of Dr. Ram Sajeevan Maurya, Assistant Professor, Department of Metallurgy Engineering and Materials Science and Dr. Girish Verma, Assistant Professor, Department of Mechanical Engineering.

The matter presented in this thesis has not been submitted by me for the award of any other degree of this or any other institute.

27/05/2022

Nismath V H

This is to certify that the above statement made by the candidate is correct to the best of my/our knowledge.

27/05/2022 27/05/22

Dr. Ram Sajeevan Maurya **Dr. Girish Verma**

NISMATH V H has successfully given her M.Tech. Oral Examination held on **02/06/2022**

Signatures of Supervisors: Convener, DPGC

06/06/2022 07/06/2022 07/06/2022

Signature of PSPC Member:

Dr.Sumanta Samal

07/06/2022

Signature of PSPC Member:

Dr.Dan Sathiaraj

07/06/2022

ACKNOWLEDGMENT

I take this opportunity to express my deep sense of respect and gratitude to my project guide, **Dr. Ram Sajeevan Maurya**, Assistant Professor, Department of Metallurgy Engineering and Materials Science, and co-guide, **Dr. Girish Verma,** Assistant Professor, Department of Mechanical Engineering, for trusting me to complete this project under their supervision. Their continual support, thoughtful discussions, and ongoing reviews have enabled this work to progress to its current state. I am very thankful to my PSPC members, Dr. Sumanta Samal and Dr. Dan Sathiaraj, for their periodic evaluation of my research and their advice and valuable suggestions.

I would also extend my sincere gratitude to Mr. Suman Vadla, Ph.D. scholar at NIT Rourkela, for his continuous support and appreciable input for my research project.

I am also thankful to the faculties, research scholars, and lab assistants of the MEMS Department and Mechanical Engineering Department of IIT Indore for their support and for allowing me to use their lab facilities, without which I would not be able to move forward in my research.

It is a pleasure to acknowledge the moral support and help extended by my fellow lab mates in the Advanced Powder Technology Laboratory and Metallurgy Engineering MTech -2022 batch colleagues.

I cannot end these prefatory words without expressing my heartfelt gratitude and devotion to my beloved parents for their blessings and encouragement to keep my spirits up throughout my work. I want to convey my deepest gratitude to everyone who assisted me directly or indirectly during this whole project.

With regards,

Nismath V H

ABSTRACT

The behavior of structures under ballistic impact is of significant interest in the defense industry. Kinetic energy penetrators have been widely used to destroy tanks, armored vehicles, and other armored targets. With the increase in armor thickness and improvements in armor protection technology, the armor-piercing capacity of rod penetrators needs to be further improved. Research currently focuses on tungsten heavy alloy (WHA) penetrators, as the conventionally used depleted uranium alloys are hazardous for use on battlefields. Tungsten-heavy alloys are a potentially suitable candidate for penetrator application, even though it has a comparatively lower penetration performance than depleted uranium alloys because of their high density, strength, ductility, etc. Studies have focused on improving tungsten-heavy alloys' mechanical properties and penetration capabilities for the past two decades. Developments in processing methods, alloying, strengthening, etc., are proposed as effective solutions from past research.

This research project investigates the penetration performance, and dynamic deformation behavior of some newly developed oxide dispersion strengthened tungsten heavy alloys (ODS-WHA) fabricated through conventional sintering. Several studies have shown that the oxide dispersion strengthened tungsten heavy alloys have better penetration performance than conventional ones. The suitability of the novel alloys as penetrator materials is studied after evaluating the high strain rate deformation behavior by performing the Split Hopkinson Pressure Bar (SHPB) test under various strain rates. The Johnson-Cook material and damage model describes the deformation behavior during the ballistic impact. ABAQUS explicit dynamic simulation software is used to model the ballistic impact test. The penetration performance of new alloys is studied from the simulation results.

TABLE OF CONTENTS

LIST OF FIGURES

LIST OF TABLES

ACRONYMS

WHA	Tungsten Heavy Alloy
ODS	Oxide Dispersion Strengthened
KEP	Kinetic Energy Penetrator
SHPB	Split Hopkinson Pressure Bar
RPM	Rotations Per Minute
FEA	Finite element Analysis
FEM	Finite Element Method
JC	Johnson-Cook
A	Yield strength
B	Coefficient of strain hardening
n	Strain hardening exponent
C	Coefficient of strain rate hardening
m	Thermal softening exponent
RHA	Rolled Homogeneous Armor
Tm	Melting point temperature

Chapter 1 INTRODUCTION

The penetrator is the central lethal part of an armor-piercing projectile used to destroy tanks, armored vehicles, and other armored targets. The penetration performance of these kinetic energy penetrators depends on the properties of the material used as the penetrator core. Depleted uranium and tungsten heavy alloys (WHAs) are used mainly as penetrator cores due to their high density. Penetrator materials should have high density, high strength, good ductility, and 'self-sharpening' ability, ensuring good penetration performance. However, the WHAs resist self-sharpening due to their poor susceptibility to adiabatic shear band formation during high strain rate dynamic deformation. Recent studies on this topic have focused on improving the penetration performance of WHAs, by developing the self-sharpening capability. WHAs are conventionally processed by powder metallurgy routes. Alternatives are being studied to enhance the mechanical properties of these materials. Also, alloying and strengthening the WHAs to improve penetration capability is also attaining a research focus. Fine-grained WHAs and oxide dispersion strengthened WHAs are proved to have higher penetration performance than the conventional ones [1].

1.1. Kinetic Energy Penetrators (KEPs)

Kinetic energy penetrators (KEPs) are ammunitions that penetrate through an armored vehicle by inflicting local damage to the targeted area. The long rod design and the high density of materials employed as the core enable the projectile to bring considerable kinetic energy to bear upon a minimal size of the target. The impact velocity of these projectiles lies between 1-2 km/sec. The conditions at the head of the penetrator will be very severe, involving high temperature (~2000°C) and high strain rate (up to 10^6 per sec) and under a remarkably high hydrostatic pressure (2-6 GPa) [2]. Hence the deformation of penetrator and armor materials occurs at extremely high strain rates allowing little time for the conduction and dissipation of the generated heat. This causes an adiabatic heating condition, which results in substantial plastic deformation at the penetrator's head. The deformation sometimes causes the penetrator head to form a mushroom-like shape, which eventually reduces the penetration depth due to an increase in the diameter of the penetrator's head. The penetration performance of a long rod penetrator is measured in terms of depth of penetration and crater hole diameter on the target. A larger depth of penetration and smaller crater hole diameter is desirable.

1.2. Tungsten Heavy Alloys (WHAs)

Tungsten is a refractory metal with the highest melting point of 3420°C, high-temperature strength, creep resistance, thermal conductivity, electrical resistance, and lowest thermal expansion coefficient. Its major disadvantages are very high brittleness and oxidation. To increase its plastic characteristics and to increase strength, it can be alloyed in three different ways [3]:

1. Solid Solution alloys
2. Heterogeneous alloys (Dispersion hardening alloys)
3. Precipitation hardening alloys

Tungsten Heavy Alloys (WHA) typically contain about 80-98wt.% tungsten and low melting point transition elements like nickel, cobalt, copper, and iron [4]. The spherical W particles will be embedded in the low melting element matrices. W and its alloys are usually manufactured through powder metallurgy routes. The common melting alloys aid liquid phase sintering slightly above their melting temperature, increasing the densification and microstructural homogeneity, resulting in near-total density after sintering. WHAs have a high density (16000-18000 kg/m^3), high strength (1000-1700 MPa), high flexibility (10-30%), and good corrosion resistance [5].

WHAs are widely used in the defense industry as kinetic energy penetrator materials and counterbalance weights for gyroscopes. Even though it has high oxidation sensitivity, they are being used in engines, rockets, and plasma-facing material in nuclear reactors by alloying with aluminum, silicon, and chromium. They prevent oxidation by forming an oxide layer by forming Al_2O_3, SiO_2, and Cr_2O_3 [6].

1.3. Conventional Sintering of Powders

In the powder metallurgy process, element powders are compacted and sintered at high temperatures. The different powder metallurgy processes are Conventional Sintering, Spark Plasma Sintering (SPS), Microwave Sintering, Powder Injection molding, Ball milling, Mechanical alloying, etc.

Conventional sintering uses three major steps to compact near full-density alloys. The first step is to blend the powders to increase the homogeneity of elemental powders. Usually, ball mills are used for this mixing, and it is reported that mechanical alloying happens because of adhesion and neck formation between the powder particles [7]. The second step is compaction of the mixed powders in a die or mold at high pressure or load. After this step, a green compact with a relatively low density than the final product will be produced. The third and final step is sintering, where the green compact is heated in a controlled atmosphere to bond the powders metallurgically. Conventional sintering is highly efficient for making WHAs, as it creates a liquid phase sintering scenario with W and other low melting transition elements. The green compact will be heated above the melting point of these transition elements. They will melt, creating a soft, ductile matrix in which W particles will be embedded. In some cases, W can dissolve in the matrix. The properties of sintered products mainly depend on the sintering time and temperature. Prolonged milling time and heating can result in deterioration of properties.

1.4. Split Hopkinson Pressure Bar (SHPB) Test

Mechanical properties of materials are generally strain rate dependent. Materials behave entirely differently in both quasi-static and dynamic conditions. Split Hopkinson Pressure Bar tests are usually used to determine the deformation behavior of materials under higher strain rates of around 100 – 10000/sec. The mechanism used in the SHPB test is the propagation of a stress wave along a long thin bar. The specimen deformed by this technique undergoes a uniaxial stress deformation [8].

SHPB uses the one-dimensional wave propagation principle. The main components in the SHPB setup are a striker bar, an incident bar, and a transmission bar. All the bars will be of the same material and diameter. A gas gun will be facilitated with a barrel, where the striker bar will be placed temporarily. The specimen will be placed between the incident and transmission bars, and the striker will hit the other end of the incident bar by the pressure given through the gas gun. The schematic diagram of the SHPB test setup is shown in figure 1.1. The elastic compression wave will propagate through the incident bar to the specimen, and then a part will be transmitted to the transmission bar. A portion of the propagated wave will be reflected into the incident wave. The sample will get plastically deformed due to this repeated wave propagation. The transmitted and reflected pulses will be captured using strain gauges placed on transmission and incident bars. The elastic strain recorded by the strain gauges can be used to calculate the required stress and strain data. The equations for finding strain rate, strain, and stress from SHPB output, based on the one-dimensional wave theory, are given below:

Strain, $\epsilon = \frac{-2Cb}{ls} \int_0^t \epsilon\mathrm{R}\, dt$

Strain rate, $\acute{\varepsilon} = \frac{-2Cb\in R}{ls}$

Stress, $\sigma = \frac{\text{Eb } \epsilon\text{tAb}}{\text{As}}$

Where C_b = Bar wave speed

ϵ_R= Reflected strain signal measured at the incident bar

l_s = Specimen length

E_b = Bar elastic modulus

A_b = Bar cross-sectional area

A_s = Specimen cross sectional area

ϵ_T = Transmission bar signal

These relations assume uniform deformation under a high strain rate. The force at both ends of the specimen is supposed to be in equilibrium [9].

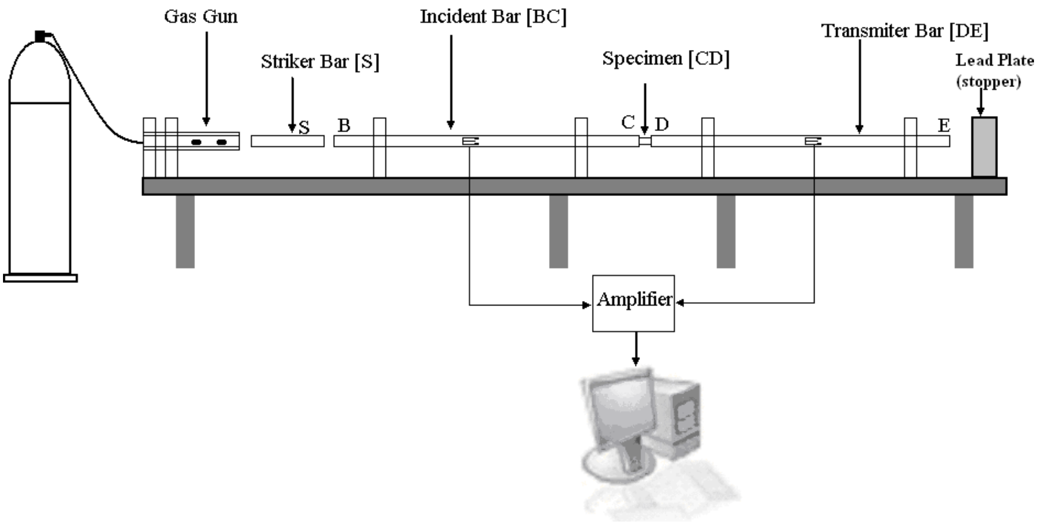

Figure 1.1: Schematic of SHPB test setup [8]

1.5. Organization of Thesis

Chapter 1: Brief introduction of Kinetic Energy Penetrators, Tungsten heavy alloys, Convention sintering of powders, and Split Hopkinson Pressure Bar test.

Chapter 2: A literature review of past research works, research gap identification, and setting the objectives for current research.

Chapter 3: Experimental procedures, including materials selection and preparation, Split Hopkinson Pressure bar test, and metallurgical characterization

Chapter 4: Numerical modeling of ballistic impact described using different modules in ABAQUS.

Chapter 5: Results and discussion of experimental and simulation works

Chapter 6: Conclusions from current research

Chapter 7: Future scope of recent work

Chapter 2 LITERATURE REVIEW AND OBJECTIVES

The scientific community has far acknowledged the application of tungsten heavy alloys as KEP material in the last two decades. As a result, several compositions of WHAs have been proposed for this application, and the search for new alloys is still in progress. Optimization in the fabrication of these long rod projectiles also demands more research and development.

2.1. Application of Tungsten Heavy Alloys as Kinetic Energy Penetrators.

Until the last few decades, the Depleted uranium alloys were commonly used as kinetic energy penetrators till the previous few decades, due to their high density. They penetrate through a minimum area of armored targets with high efficiency. But due to the fatality of using Depleted Uranium (DU) alloys on the battlefield, which affects both humans and the environment, nowadays, research is concentrating on other metal and ceramics alternatives. Figure 2.1 compares some of the candidates for KEP material according to their densities and limits velocities.

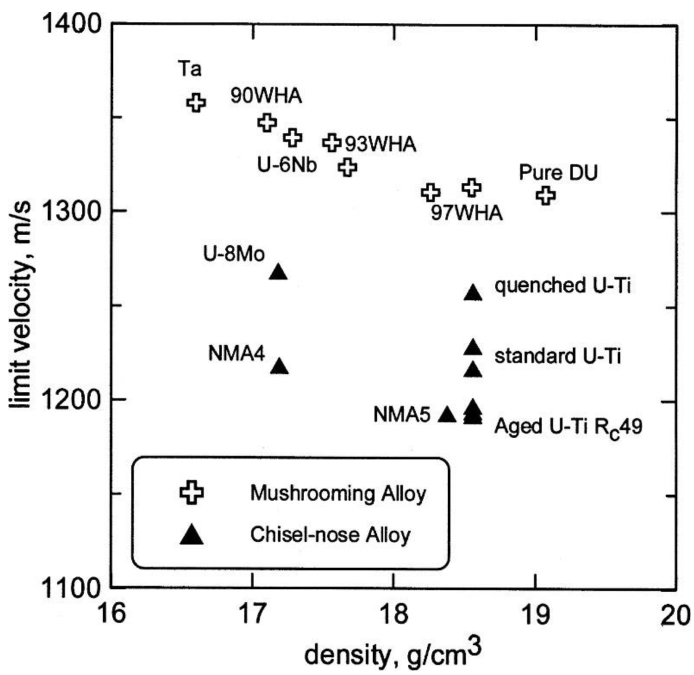

Figure 2.1: Different KEP candidate materials comparison with their densities and limit velocities

WHAs have high density, comparable to the DU alloys, and high strength and ductility. Depleted uranium alloys develop flow softening at deficient strain itself and cause adiabatic shear failure. The shear banding results in the arrow-like head formation, reducing the crater diameter and increasing penetration depth. This effect is called “self-sharpening,” highly desired for penetrator materials. Upadhyaya A (2001) states that “the onset of localized plastic instability leading to shear banding is necessary for improved KEP performance.” So, to increase the penetration performance, promoting localized adiabatic shear banding at lower strains is desired. The essential properties required for a penetrator material are given in Table 1 [3].

Attribute	Function
High density	Impart high impact energy
High strength	For greater heat generation for a given strain
Low heat capacity	The heat generated results in rapid temperature rise.
Low work hardening rate	Easier flow softening
Low strain hardening rate	Shear localization occurs at a lower strain.
High thermal softening rate	Shear banding initiated at a lower temperature

Table 2.1: Requirements of an ideal KEP material

WHAs require much higher plastic deformation (higher strains) to override strain and strain rate hardening mechanisms due to low thermal softening rates. So, during impact, they will deform and form a mushroom or rounded head, which increases the crater diameter and decreases the penetration depth, and consumes considerable kinetic energy for penetration. The deformation on both DU alloys and WHAs is shown in figure 2.2.

To improve the penetration capability of WHAs by promoting self-sharpening ability, research is focusing on two main areas, alloying and different processing routes. Alloying with low melting point soft, ductile elements are proved to increase the ductility. Ramesh and Coates have conducted many experiments on W alloys using compression Kolsky bars at very high strain rates and concluded that the dynamic deformation behavior of these alloys is controlled by the W grains. In contrast, they do not influence W alloys' compressive stress, strain hardening, and strain rate sensitivity [10]. In WHAs, promoting shear band formation can increase the penetration performance by initiating cracks through shear localized sites, thus creating a chisel-like head. The W-W interfaces restrict the shear band formation, and hence reducing the W-W contiguity is a possible solution [11]. But reducing the W content will reduce the density and kinetic energy, resulting in poor penetration.

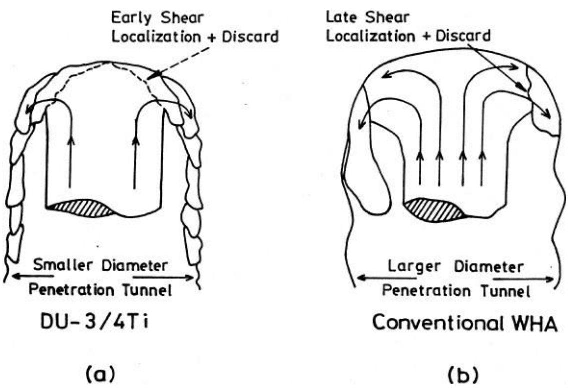

Figure 2.2: Deformation at the DU alloy and WHA penetrator head [12]

Rabin et al. have shown that the tensile strength and ductility of WHAs increase with reduced contiguity [13]. Lankford et al. also confirmed that the lower W-W contiguity would increase shear band formation capacity [14]. The dynamic deformation behavior of oxide dispersion strengthened WHA has shown the possibility of adiabatic shear band formation [15]. Fine-grained WHA, 95W–3.75Ni–1.25Fe, was found to have higher penetration performance than conventional coarse-grained WHA in the ballistic impact test by Rongmei Luo et al. [16]. Acute head formation in this fine-grained alloy facilitated around a 10.5% increase in penetration depth and an 8.2% decrease in crater diameter. SHPB results have shown failure at lower strain rates than conventional WHA. Similarly, X. Gong et al. [17] have also demonstrated that the fine-grained WHAs exhibit low-rate sensitivity and strain hardening. They observed adiabatic shear band formation in high strain rate experiments. Hence, to promote the adiabatic shear band formation and thereby increase the self-sharpening behavior of WHA, fine-grained WHAs and reduced W-W contiguity proved efficient. But in some studies, penetration performance was reported as unchanged even after reducing the grain size and contiguity [18]. In work by J.L. Fan et al., Y_2O_3 dispersed fine-grained WHA has shown adiabatic shear band formation at strain rates of around 1900/sec [19]. Y_2O_3 dispersoids will promote interfacial debonding between W particles, thus improving penetration performance without adiabatic shear banding and reducing the grain size without increasing the interfacial area [20]. The brittle fracture nature of W and its alloys can be changed into a ductile fracture by adding oxide dispersoids [21].

The improvements in fabrication methods are also under research. WHAs subjected to hot hydrostatic extrusion and hot torsion and WHAs prepared by infiltration method has better self-sharpening capacity than sintered samples [22], [23].

2.2. Numerical Modelling of ballistic impact.

The complex nonlinear phenomena and dependency on many parameters make complex events like ballistic impact be analyzed and solved using analytical methods. Nowadays, dynamic simulation software coupled with the primary finite element method of problem formulation and solution is gaining popularity. Anderson et al. Conducted a brief review of numerical and analytical approaches to modeling ballistic impact [24]. Gupta et al. [25] studied the effect of nose and target geometry and impact velocity on aluminum plates using the ABAQUS finite element code. The numerical modeling matched the experimental results. Similarly, M A Iqbal et al. studied the effect of target configuration and span. Using ABAQUS, and results complemented the experiment [26]. Tiwari et al. proved that the boundary conditions variations are insignificant in ballistic simulations using numerical modeling [27]. Many works have already been performed and confirmed that the dynamic behavior of penetrators and targets could be effectively modeled using FEA tools [28] – [31]. The Johnson-Cook material and failure model models the deformations involving strain, strain rate, and thermal softening. This model is proved to be highly efficient in sporting high strain rate dynamic events like vehicle crashes, ballistic impact, drop tests, etc.

2.3. Identified research gaps from the literature review.

Research on the dynamic deformation behavior and the mechanism of failure of the WHAs is essential for alloy design, fabrication process, and microstructural modification to improve the dynamic properties and the penetration performance. However, they have not been actively pursued, demanding profound studies on various existing and newly developed alloys. Some researchers have shown that yttrium dispersoids promote penetration performance by interfacial debonding between tungsten particles. But the studies lack clarity about the high strain rate dynamic deformation tests that were not performed and analyzed on ODS alloys properly. Therefore, determining the penetration performance and high strain rate deformation behavior of novel ODS tungsten heavy alloys is vital in ballistic applications.

2.4. Objectives of the research

From the literature survey on tungsten heavy alloys in kinetic energy penetrator application, a necessity for more concise and evident research about the oxide dispersion strengthened tungsten heavy alloys in the above said application domain seems inadequate. Oxide dispersion strengthened tungsten heavy alloys (ODS-WHA) have better penetration performance and superior mechanical properties. So, a study on its penetration performance can be initiated by putting forward some novel ODS-WHA as potential kinetic energy penetrator candidates.

Considering the research gap, the objective of this research project is to study the penetration performance of some novel ODS-WHA fabricated through conventional sintering. The project aims to find the suitability of the newly developed ODS-WHAs as kinetic energy penetrator materials. Split- Hopkinson Pressure Bar test can be carried out to determine the deformation behavior at very high strain rates. Ballistic impact test simulations can analyze the penetration performance in terms of impact velocity, crater diameter, and penetration depth.

Chapter 3 EXPERIMENTAL PROCEDURES

3.1. Material Selection

From the extensive literature survey, it has been identified that material should have high density, strength, ductility, and hardness for the kinetic energy penetrator application. Silicon (Si) addition improves the sintered density of several alloys and reduces the oxidation behavior at higher temperatures. Tungsten and its alloys are usually manufactured through powder metallurgy routes because of their high melting point. Nickel (Ni) will act as a binder phase in WHAs, and it improves the ductility of the alloy considerably. Cobalt (Co) helps strengthen the W-binder interfacial strength through solid solution strengthening. It improves the elasticity and stability of the alloy. The addition of a small amount of Yttria (Y_2O_3) dispersion enhances the hardness and strength of the alloy. Based on these factors, the following compositions were selected to manufacture through the mechanical alloying and pressure-less conventional sintering process.

Alloy 1: 98.7W-1Si-0.3Y_2O_3 (WSY)

Alloy 2: 88.7W-10Ni-1Si-0.3Y_2O_3 (WNSY)

Alloy 3: 85.7W-10Ni-3Co-1Si-0.3Y_2O_3 (WNCSY)

The powders used for manufacturing the alloys are given below:

1. W powder (99.5% purity, -325 mesh)
2. Si powder (98.5% purity, 200 mesh)
3. Y_2O_3 powder (99.995% purity, 20-50 nm)
4. Ni powder (99.8% purity, -100+325 mesh)
5. Co powder (99.8% purity, -100+352 mesh)

3.2. Mechanical alloying and Conventional Sintering

As a part of an ongoing project at NIT Rourkela[6] to study the effect of Si and Y_2O_3 addition on WHAs, samples were prepared. The powders were blended to make the 0.3 wt.% nanoscale Y_2O_3 dispersed W-1Si, W-10Ni-1Si, and W-10Ni-3Co-1Si alloy compositions. The planetary ball mill with 10 mm diameter tungsten carbide (WC) balls and a 1.5-liter capacity WC jar was used to mill the blended powders. At a ball to powder ratio of 10:1, wet milling was performed in toluene medium for 10 hours at 300 RPM.

After milling, the powders were compacted using a uniaxial press by giving a uniform pressure of 500 MPa for 5 minutes into 10 mm diameter pellets. The pellets were subjected to conventional pressureless sintering at 1500°C for 2 hours. Sintering is performed in a hydrogen atmosphere to prevent oxidation, W, and other powders.

The percentage relative density, microhardness values, and the quasi-static compression test (at strain rate = 0.1/min) data were taken from the study of V. Suman et al. Archimedes' principle was used for measuring bulk density, Vickers microhardness tester was used for hardness measurement, and Universal Testing Machine was used to study the compression strength in work mentioned above.

3.3. Split Hopkinson Pressure Bar Test

3.3.1. Test Setup

The SHPB test was performed on a Miniature SHPB apparatus in the Mechanics of Materials laboratory, IIT Indore. The setup consists of a striker bar, an incident bar, and a transmission bar made of maraging steel (grade 350) with and diameter of 3 mm. The length of the incident and transmission bars is 600 mm, and that of the striker bar is 60 mm. Strain gauges were connected at the center of the incident and transmission bars. The bars are supported on a bushing on steel rods, and they move independently in a longitudinal direction within the bushing. The image of the Miniature SHPB facility is shown in figure 3.1. The data is collected from the strain gauges connected to a transducer amplifier unit and a Tektronix TBS2000B digital storage oscilloscope connected to a computer. The oscilloscope is a 5M point record length, 200 MHz bandwidth, and 2GS/s sample rate capture and displays significantly more signal to debug and validate designs faster.

3.3.2. Sample preparation

The sample sizes demanded by the test setup are 1mm diameter cylindrical specimens with 0.5 mm or less than 0.5 mm thickness. The sintered samples were cut into 1 mm diameter cylinders using ECOCUT CNC Wire EDM machine and then sliced into <=0.5 mm thick samples using a diamond blade cutter. Each alloy was decided to be tested under 2, 4, and 6 bar pressures and three trials for each pressure.

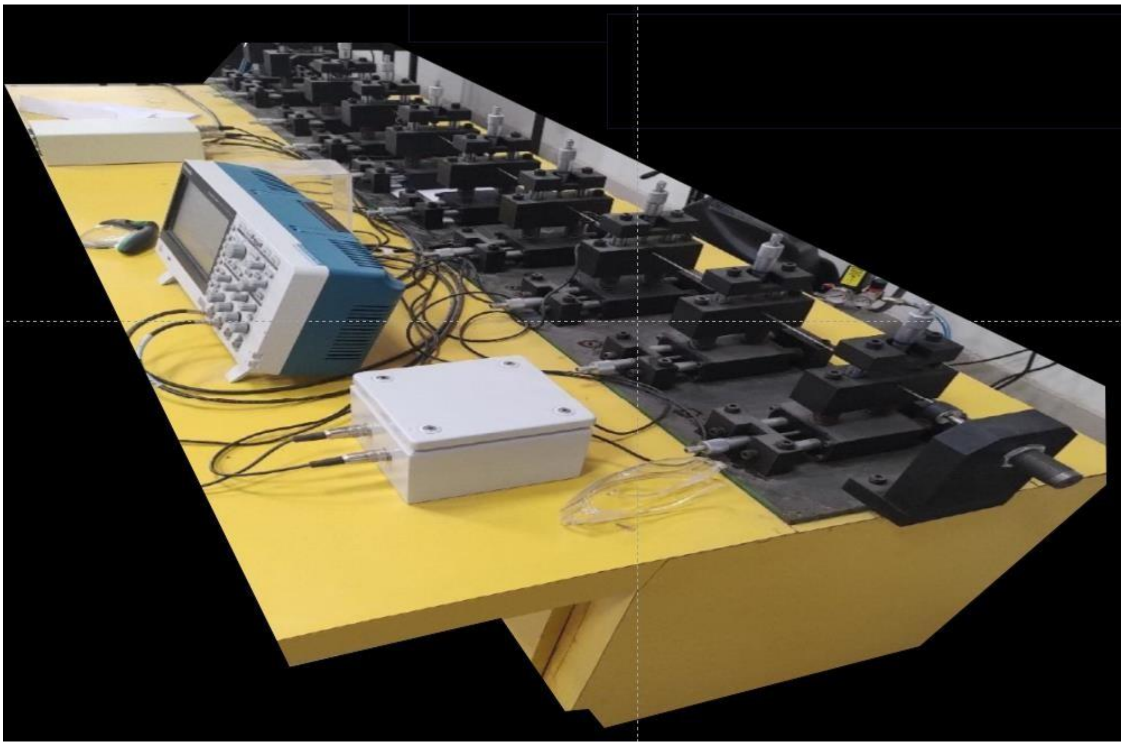

Figure 3.1: Miniature SHPB test apparatus

was performed. So, nine samples were prepared for each alloy in the desired dimensions. The samples were then roughly polished to remove burrs and unequal surfaces.

3.3.3. Calculations from test data

The data obtained from the strain gauge will be in voltage vs. time, which needs to be converted to strain–time data using relations between the output voltage and strain. An open-source SHPB analysis tool written using MATLAB, developed by D.K. Francis et al. [32] issued for this purpose. The changes in force, displacement, stress, and strain can be visualized in a user-friendly interface from the raw voltages, geometries, and properties of bars and specimens. The stress-strain curves with an averaged strain rate can be plotted. Basic steps to use the SHPB open tool are given below:

1. Import the voltage-time data from the test to the user interface. The user interface of the tool is shown in figure 3.2.

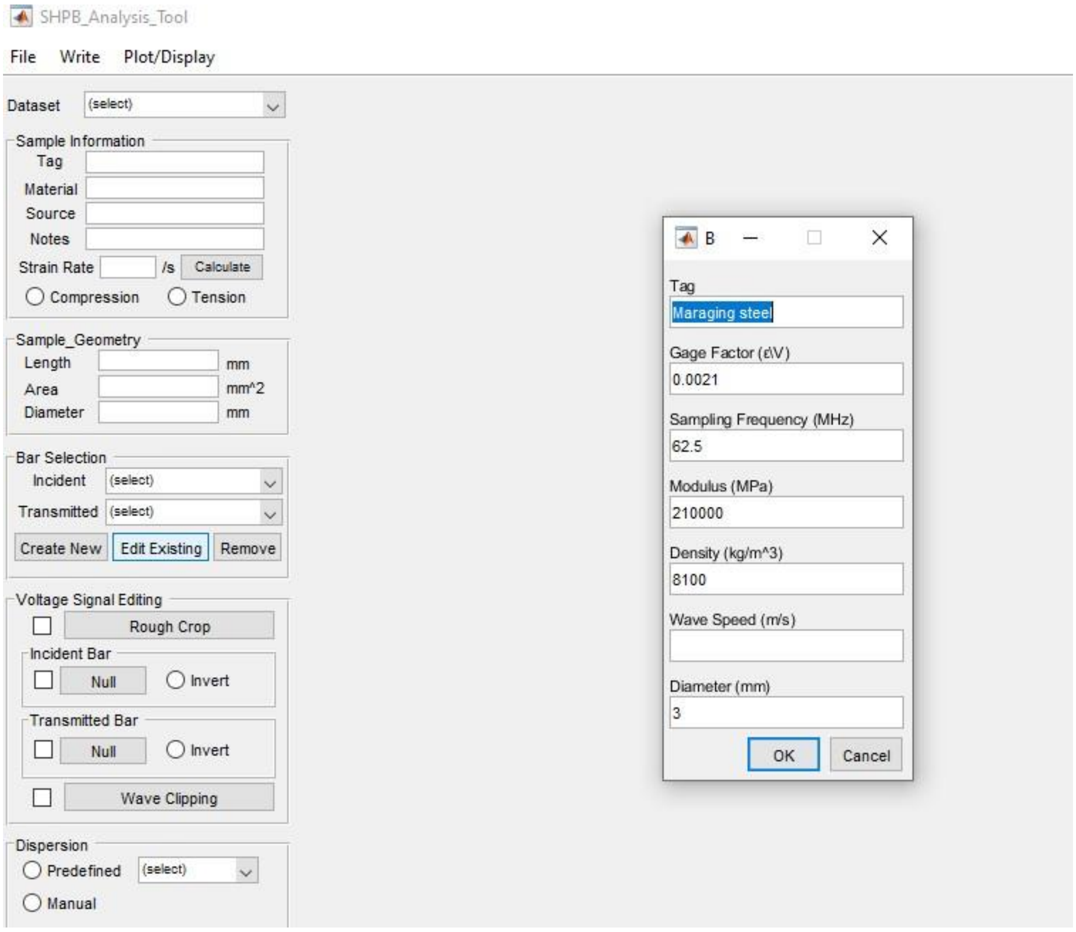

Figure 3.2: The user interface of the SHPB output analysis tool

2. Determine the null space in the signal to zero the voltage accurately. The window for rough cropping the signal and null defining null space is shown in Figures 3.3 and 3.4.

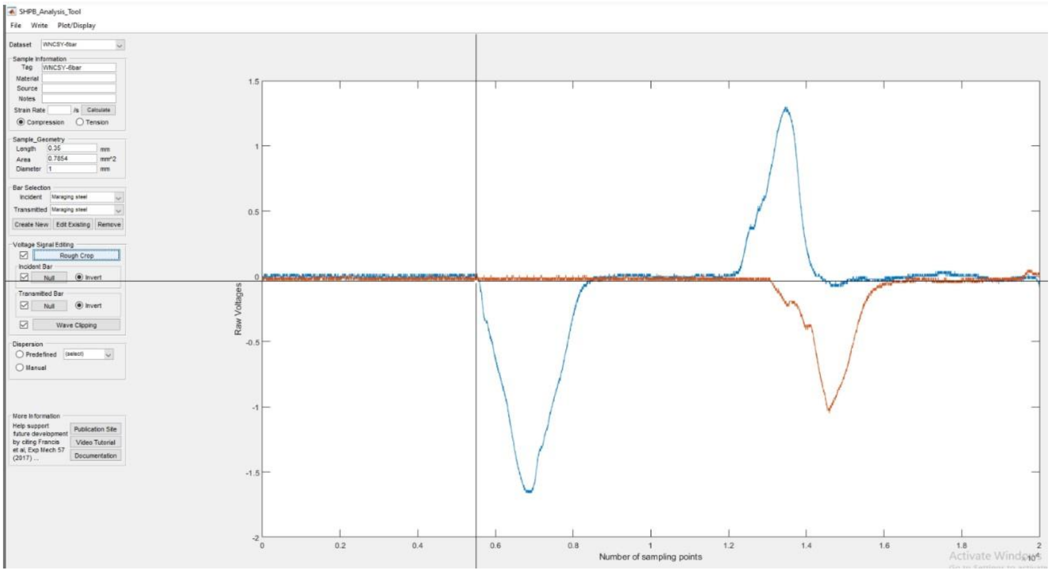

Figure 3.3:The window in the SHPB output analysis tool for rough cropping the voltage signal

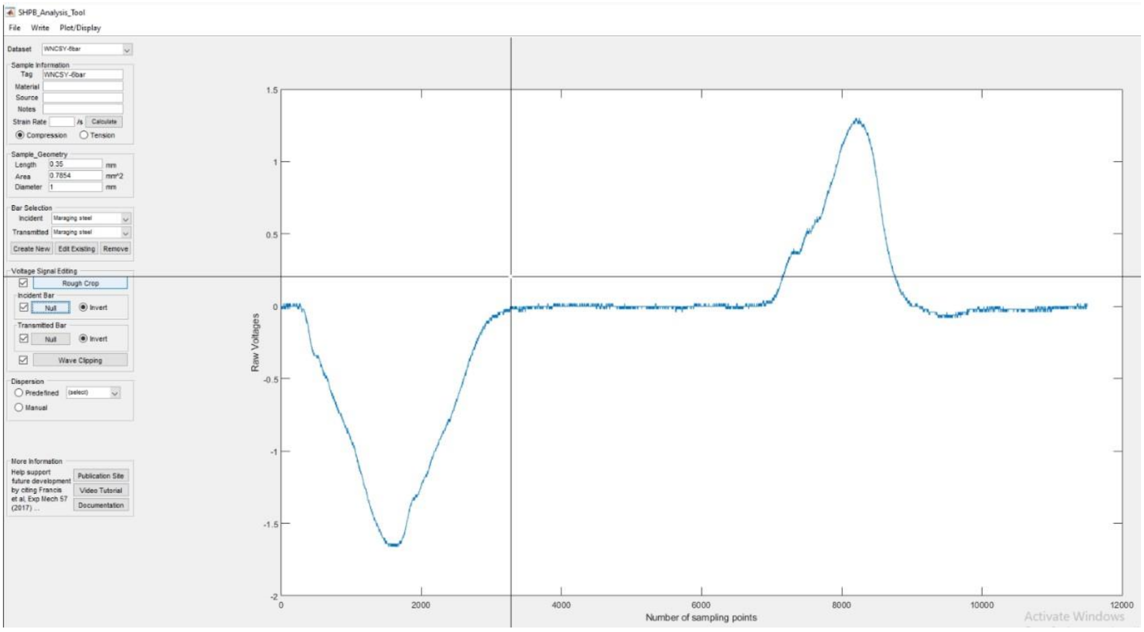

Figure 3.4:The window in the SHPB output analysis tool for defining the null space of the voltage signal

3. To align the incident, transmitted, and reflected waves, the distance between the strain gauge and the specimen can be manually set up using sliders. This distance can be calculated using the relations:

$$
\begin{aligned}
d_I &= \tfrac{1}{2} c_I \times \Delta t \, (Sl_R - Sl_I) \\
d_T &= \Delta t \, (Sl_T c_T - Sl_I c_I) - d_I
\end{aligned}
$$

where c_I= wave speed of the incident bar

c_T = wave speed of the transmitted bar

Δt = period between voltage samples

SL_R, SL_I, and Sl_T are the slider locations for the beginning of the reflected, incident, and transmitted waves.

The strain is expressed as a discrete Fourier series, using dispersion method:

$$
\varepsilon\,(n\Delta t) = \frac{A_0}{2} + \sum_{k=1}^{N} \left[A_k \cos\,(k\omega_0 n \Delta t) + B_k \sin\,(k\omega_0 n \Delta t)\right]
$$

where n = 1, 2, . . . 2N; k = 1, 2, . . . N

Fundamental frequency ω0 = 2π/t = 2π/(2NΔt). The discrete Fourier coefficients are given as

$$
\begin{aligned}
A_0 &= \frac{2}{T}\sum_{n=1}^{2N} \varepsilon\,(n\Delta t)\,\Delta t \\
A_k &= \frac{2}{T}\sum_{n=1}^{2N} \varepsilon\,(n\Delta t)\cos\,(k\omega_0 n\Delta t)\,\Delta t \\
B_k &= \frac{2}{T}\sum_{n=1}^{2N} \varepsilon\,(n\Delta t)\sin\,(k\omega_0 n\Delta t)\,\Delta t
\end{aligned}
$$

The tool uses non – the linear curve fit approach, which calculates wave velocity at each wavelength. The inverse discrete Fourier transformation and the wavelength-dependent wave velocities and phase angles create a properly dispersed signal.

This step can be performed using the Global Optimization toolbox in MATLAB easily.

4. The forces at the incident and transmitted ends F_I (t) and F_T (t) is calculated by

$$
\begin{aligned}
F_I(t) &= A_I E_I\,(\varepsilon_I(t) + \varepsilon_R(t)) \\
F_T(t) &= A_T E_T \varepsilon_T(t)
\end{aligned}
$$

A is the area of bars, and E is the elastic modulus of bar material. ε_I (t), ε_R(t), and ε_T (t) are incident, transmitted, and reflected strain values at time t.

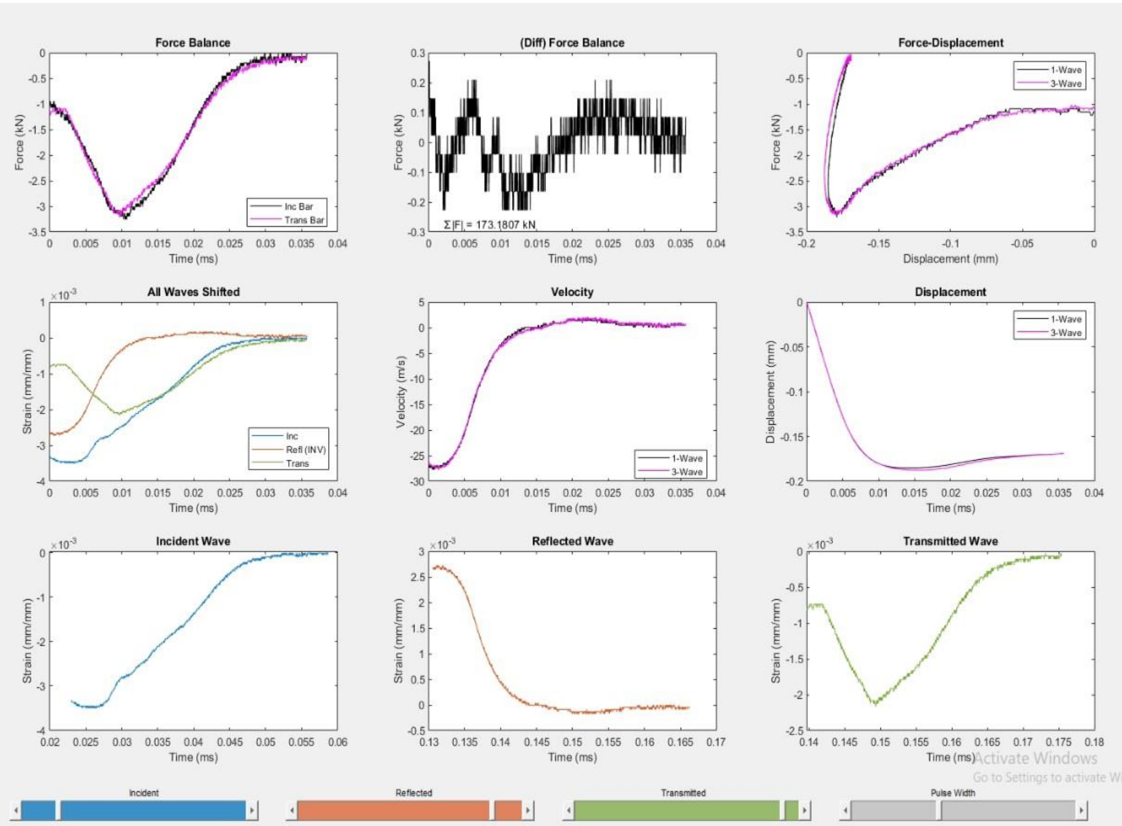

Figure 3.5: User interface in the SHPB output analysis tool calculating force equilibrium

One wave analysis is carried out in this study, and F_T is used for force. The relation calculates velocity: $v_{1\text{wave}}(t) = 2c_I \varepsilon_R(t)$

Where c_{I} = wave speed of the incident bar

Displacement is calculated as: $u_{1\text{wave}}(t) = 2c_{0I} \sum_{t=0}^{t} \varepsilon_R(t)$

All the one wave analysis calculations assume that force is in equilibrium, i.e.,

$$(\varepsilon_I(t) + \varepsilon_R(t) = \varepsilon_T(t)).$$

The graphical user interface for aligning the incident, transmitted, and reflected voltage signals, assuming the forces in equilibrium, using a global optimization tool is shown in figure 3.5.

5. After calculating forces and displacements, stress, strain, and strain rate can be analyzed in another user interface.

From the SHPB data, true stress-true strain curves at different strain rates are plotted, and the JC parameter C (Coefficient of strain rate hardening) is calculated.

3.4. Microstructure Analysis

The powder morphology was analyzed before milling using a JEOL-JSM-6480LV Scanning electron Microscope with 15 kV voltage, and the images were used to measure the particle size. The microstructure of sintered samples was also evaluated using SEM. The deformation of samples after the SHPB test was analyzed by performing optical microscopy and SEM with JSM 7610 FPLus Schottky Field Emission Scanning Electron Microscope. Samples for metallography were prepared by cold mounting. The specimens were then polished using a Double Disc polishing setup with progressively decreasing grit sizes up to 2500. Fine polishing was performed using alumina paste on a soft velvet cloth. The polished samples were then cleaned with acetone using an Ultrasonic cleaning device for 2 minutes. The particle size of powders and grain size of consolidated samples were analyzed from the images using ImageJ and Origin software.

Chapter 4 NUMERICAL MODELLING OF BALLISTIC IMPACT TEST

The ballistic impact is a nonlinear dynamic phenomenon characterized by high deformation (strain), high strain rate, thermal softening, fracture, and continually evolving boundary conditions. Several penetrators and targets have been used in numerous experimental investigations this far. However, the expense and time involved in ballistic tests confine the researcher's reliance on them for all impact-related experiments. The use of closed-form analytical solutions is typically limited by the intricacy of ballistic impact and penetration events. As a result, numerical simulation results are usually used to supplement ballistic testing.

4.1. ABAQUS Structural Solvers

The ABAQUS software offers a single environment for preprocessing, post-processing, and analysis, making it a versatile tool for complex simulations. The key benefits of the ABAQUS platform include the use of FEA and Multiphysics, complex materials, complex assemblies, contact, failure and fracture, high-performance computing, etc., in a single user interface. ABAQUS solvers are of two types: Implicit and Explicit.

The implicit or standard solver is suited for static and low-speed dynamic events and uses implicit integration to solve the linear equations. The explicit solver solves highly non-linear quasi-static and dynamic events by Coupled Eulerian-Lagrangian, Smoothed Particle Hydrodynamics, and Discrete Element Modelling Multiphysics methods.

An ABAQUS computational model was formulated to model the ballistic impact test. The Explicit Dynamics solver was selected, and multiple cores were used parallel to reduce the analysis turnaround time.

4.2. Basic Steps in Finite Element Method (FEM)

Numerical techniques are used in FEA to solve real-world physical phenomena. Partial differential equations are used to describe these phenomena. Such research entails partitioning a continuous domain into a finite number of elements. Approximating functions are employed in the context of the intended nodal values. These nodal values can then recover all the values determined inside the elements. The basic steps of Finite Element Modelling involve:

1. Discretize the solution region into a finite number of subregions or elements.
   In ABAQUS, the mesh module is meant to discretize the continuum domain into a finite number of elements and nodes.
2. Derive the governing equations and find the relation between element properties.
   The part and property module in ABAQUS can be used to input the material properties and geometry. Selecting an appropriate material model in explicit dynamics also develops an interpolation function. The matrix equation for each element should relate the nodal values of the unknown function to other parameters. The variational approach and the Galerkin method are the most used ones.
3. Assemble the equations into a matrix form.
   The elemental matrices should be assembled to form a global matrix for solving the finite element problem.
4. Solve the global matrix system.
   The final step is to specify the boundary conditions and solve the global matrix.

4.3. Modules in ABAQUS

ABAQUS CAE is divided into different modules[33], where each module can be modeled into the essential steps in FEA. Modules can be selected from the dropdown in the context bar. Modeling of ballistic impact was performed as described below using different modules:

4.3.1. Part Module

The desired geometry can be modeled in this module using different drawing tools in the sidebar in the part module. Figures 4.1 and 4.2 show the part module interface. The KEP core and the target plate were designed as 3D, deformable solids. According to the Lanz-Odermatt empirical models on penetration depths and L/D, the rod-like geometry of the penetrator contributes to penetration. The presence of a windshield/tip serves the aerodynamics purpose of reducing drag [34]. Therefore, the penetrator rod was modeled as a right circular cylinder with an L/D ratio (aspect ratio) of 10. Target was a thick circular plate with a diameter of 100 mm and a thickness of 100mm. Since the symmetry of stress wave propagation and reflection (i.e., stress value) in the circumferential direction of the plate can be retained in a circular shape but not in a rectangular shape during the normal impact of the projectile, the plate's boundary is chosen circular instead of other shapes such as a rectangle [35].

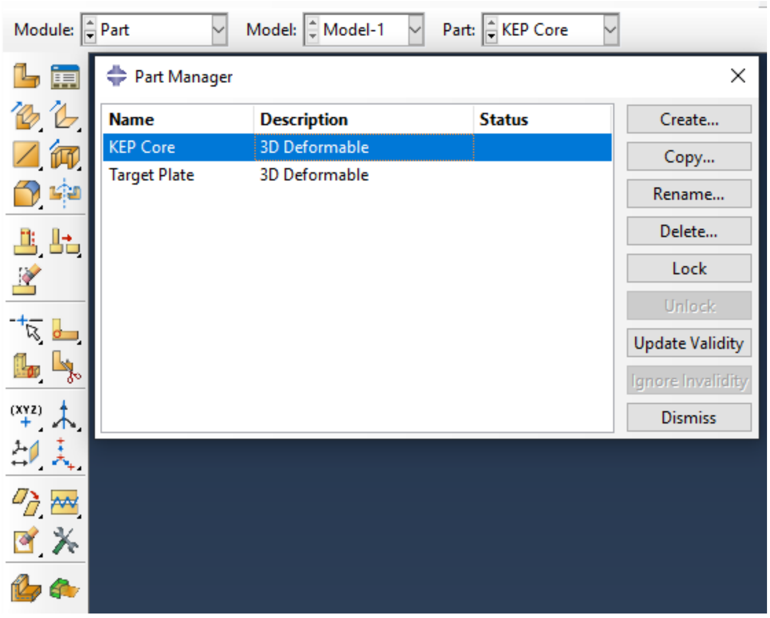

Figure 4.1: Part manager window in ABAQUS

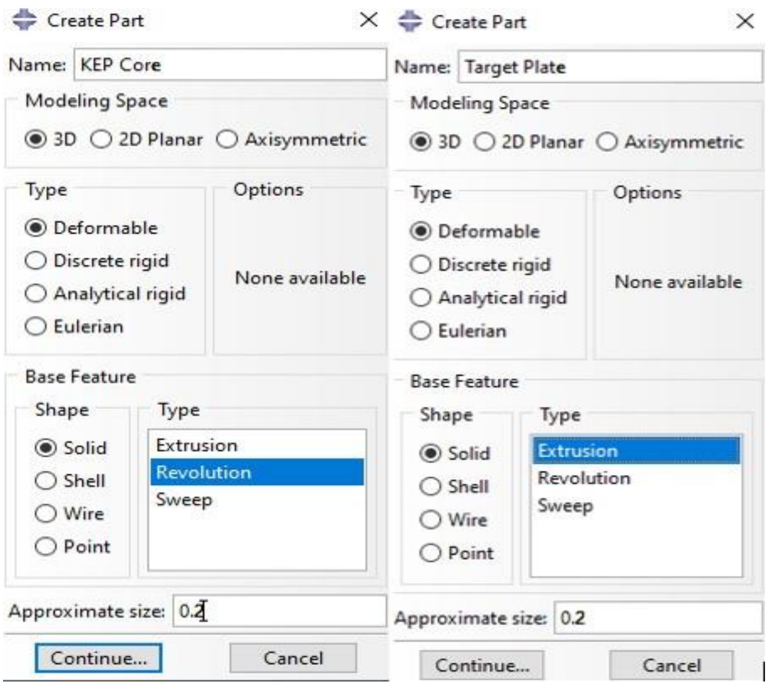

Figure 4.2: Create a Part window in ABAQUS

Assuming an axisymmetric problem having only radial compression, one-fourth of the whole geometry is considered in all simulations. So, the revolution angle for KEP core geometry was given as 90°, and the extrusion depth of the target plate was given as 50mm. The geometries of the KEP core and target plate are shown in figure 4.3.

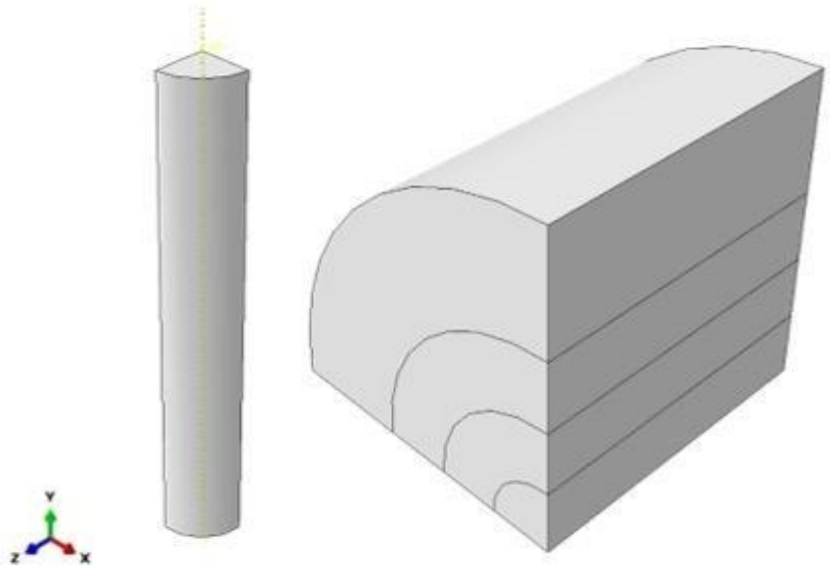

Figure 4.3: Geometries of KEP Core and Target plate

4.3.2. Property Module

In this module, desired materials and their properties can be assigned. If any, the material and damage models can be specified to predict the failure mode after explicit dynamics phenomena accurately. The geometries can be set to each material section in this module.

The KEP core was given the new alloy compositions and assigned to the sections for different simulations of the ballistic impact simulation. Rolled homogeneous Armor Steel is a commonly used armor material. So, the material properties of RHA steel were assigned to the plate. Both the material sections were specified as solid and homogeneous.

Material Model:

The Johnson-Cook material model can explain the flow stress behavior of a material under large deformations, high strain rate, and high temperatures [36]. It demands significantly less effort to determine the parameters and hence is a popular material model to define materials under impact conditions. According to the Johnson-Cook material model, the flow stress(σ) is given by the following relation:

$$\sigma = (A+B\varepsilon^{n})\ (1+C\ln\acute{\varepsilon}^{*})\ (1-T^{*m})\ \ldots.\ (1)$$

where σ is the equivalent flow stress, and ε is the equivalent plastic strain. A B, n, C, and m are the JC parameters. A is the yield strength at the reference strain rate condition, B is the coefficient of strain hardening, n is the strain hardening exponent, C is the coefficient of strain rate hardening, and m is the thermal softening exponent.

Also, $\acute{\varepsilon}^* = \varepsilon/\varepsilon_{ref}$ and $T^* = (T-T_{ref}) / (T_m - T_{ref})$, where $\acute{\varepsilon}^*$ is the dimensionless strain rate, ε_{ref} is the reference strain rate, T^* is the homologous temperature, T is the deformation temperature, T_{ref} is the reference temperature, and Tm is the melting point temperature. In the present study, ε_{ref} is 0.1/sec and T_{ref} is room temperature.

Johnson-Cook parameters A, B, and n can be calculated from the quasi-static compression test data [37], [38]. The yield strength or A value was taken as the 0.2% offset value of the true stress - true strain graph. When the deformation strain rate, $\varepsilon = \varepsilon_{ref}$, and the deformation temperature, $T = T_{ref}$, flow stress (at reference conditions) is given by the relation,

$$\sigma = (A+B\varepsilon^n) \text{ …. } (2)$$

In equation 2, the effect of strain rate hardening and thermal softening is neglected. Rearranging and taking natural logarithm on both sides of equation 2,

$$\ln(\sigma-A) = \ln B + n \ln \varepsilon \text{…. } (3)$$

By substituting flow stress and strain values at reference strain rate conditions, a plot between ln(σ-A) and ln ε can be drawn. The first-order linear regression model can be used to fit the data points. The intercept and slope of this fitted curve will give the values of JC parameters B and n, respectively.

If the temperature, T = Tref, equation 1 can be written as;

$$\sigma = (A+B\varepsilon^n)(1+C\ln\acute{\varepsilon}^*) \text{ …. } (4)$$

Rearranging the above equation;

$$\sigma /(A+B\varepsilon^n) = (1+C \ln\acute{\varepsilon}^*) \text{ …. } (5)$$

Here, the effects of thermal softening are neglected. Substitute the A, B, and n values, and plot the $\sigma /(A+B\varepsilon^n)$ - ($\ln\acute{\varepsilon}^*$) curve at different strain rates. Fit the curves using first-order linear regression, and the slope of the fitted curve will give the value of JC parameter C.

When the strain rate, $\varepsilon = \varepsilon_{ref}$, equation 1 can be rewritten as

$$\sigma = (A+B\varepsilon^n)\,(1-T^{*m}) \;\ldots.\; (6)$$

Rearranging and taking natural logarithm on both sides of equation 6,

$$\ln (1- [\,\sigma /(A+B\varepsilon^n)] = m \ln T^* \ldots.\; (7)$$

Substitute the A, B, and n values, plot the $\ln (1- [\,\sigma /(A+B\varepsilon^n)] - \ln T^*$ graph at different temperatures, and fit the curve using the first-order regression model, the slope of the curve will give them value.

The Johnson-Cook damage model [36] was specified through the VUMAT subroutine. The relation gives the Johnson and Cook failure model:

$$\varepsilon_f = [D_1 + D_2 \exp (D_3\sigma^*)]\,[1 + D_4 \ln (\acute{\varepsilon}p^*)]\,[1 + D_5T^*] \;\ldots.\; (8)$$

where $\varepsilon_f =$ Equivalent strain at failure

D_1-D_5 = Damage parameters or coefficients (varies between 0 and 1, 1 when the material is fully failed.). D is the sum of the ratio of the increment of equivalent plastic strain and equivalent plastic strain at failure. D_1 can be given the value of the strain at the initiation of necking (ultimate point) in cylindrical specimens tested at quasi-static strain rate and room temperature [38].

σ^*= Triaxiality factor = $\sigma_{mean}/\ \sigma_{equivalent}$

$\acute{\varepsilon}_p^* = \acute{\varepsilon}_p /\acute{\varepsilon}_{ref}$ where, $\acute{\varepsilon}_p =$ Plastic strain rate

In this study, temperature effects are not considered due to limitations in the experimental setup. Hence the third parenthesis in equation 1 and equation 8 will be neglected. To find the triaxiality ratio, σ^* at failure, an elastoplastic analysis of specimens having different thicknesses and notch radii has to be found. Due to limitations in making sintered samples for tensile tests, this action cannot be done, and hence D_2 and D_3 are assumed to be zero. D_4 is calculated by finding the variation with the ε_f with $\acute{\varepsilon}_{ref}$. Therefore, Johnson Cook parameters will be input as the material and failure model constants and other variables in the property module.

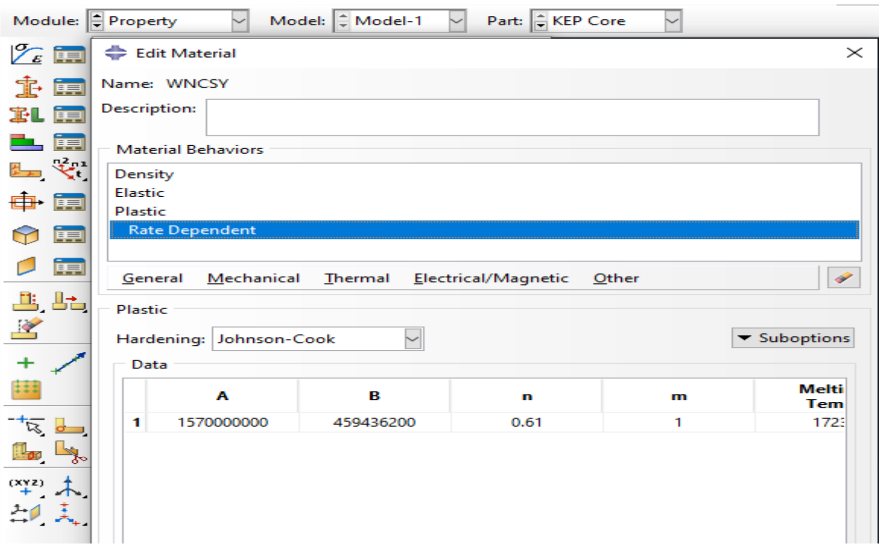

Figure 4.4: Property module window in ABAQUS

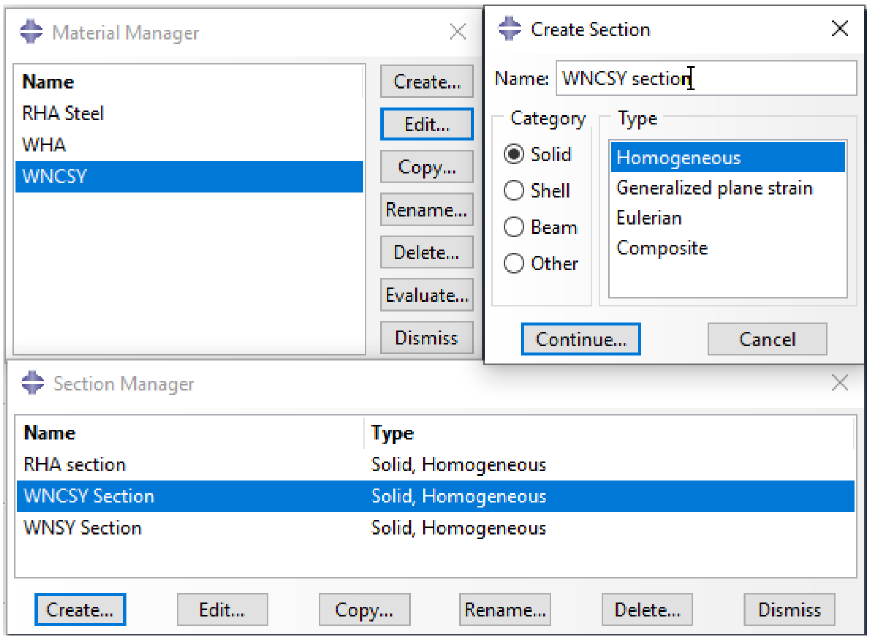

Figure 4.5: Creating and assigning section window in ABAQUS

4.3.3. Assembly module

The model can be assembled, and the assembly module can create sets. The KEP core and target plate were aligned so that the center of both cylindrical geometries met at a single point.

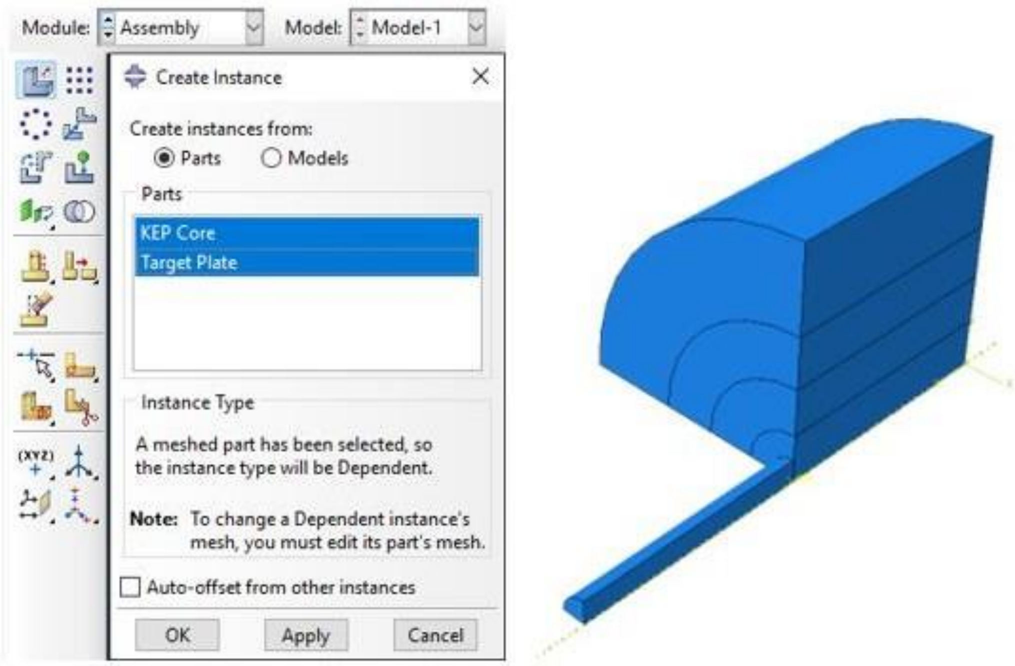

Figure 4.6: Assembly module window showing instances and the assembled geometry

4.3.4. Step Module

The analysis procedure can be configured, and output requests can be specified through the step module. The fixed and automatic methods are two primary ways ABAQUS increments the time step. The fixed method depends on user input. The automatic method utilizes a stable value of time increment for the analysis. The criteria to obtain a stable value of time increment are:

$$\Delta T < \min (L_e / C_d)$$

$$C_d = (E/\rho)$$

L_e is the characteristic length of the element, C_d is the speed of the sound wave in the material, E is the young's modulus, and ρ is the material density. The time increment is dependent on the minimum value of the ratio of L_e and C_d of all the elements [39]. ABAQUS always chooses a value lower than the minimum value of the ratio of L_e and C_d for the simulation to be conditionally stable. A value lower than the stability limit should also be chosen in the fixed time increment method. Otherwise, the simulation will be terminated. Finer meshes with smaller elements take longer job times due to lower time step increment because the size of the smallest element limits the stable time increment.

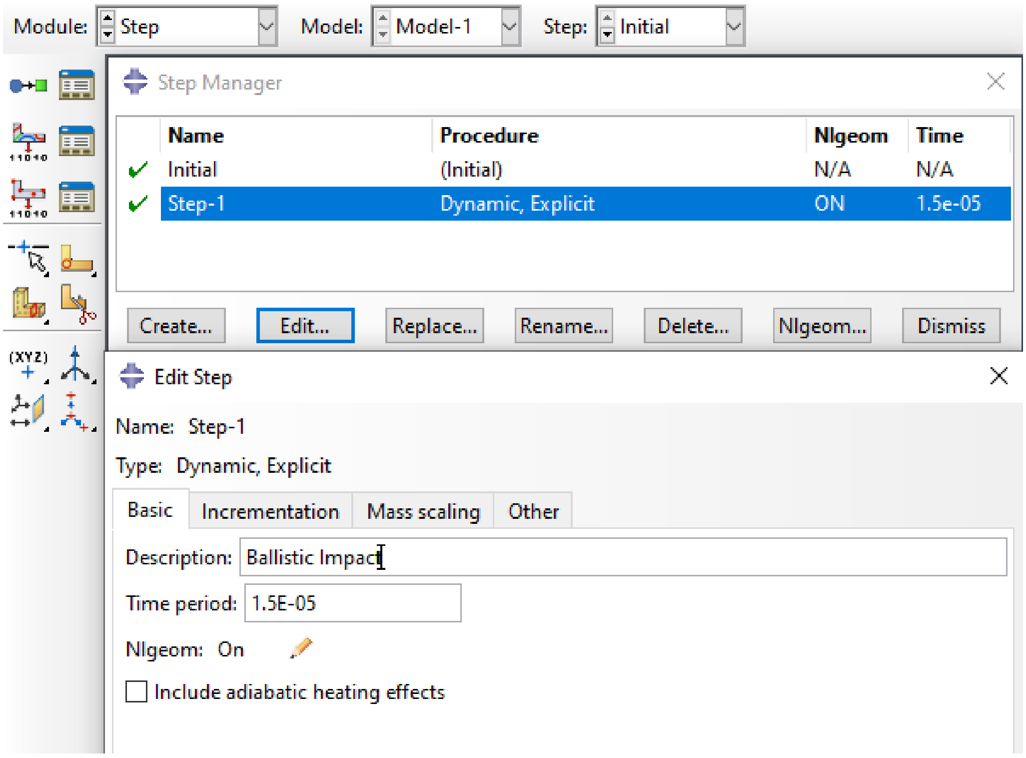

Figure 4.7: Step module window in ABAQUS

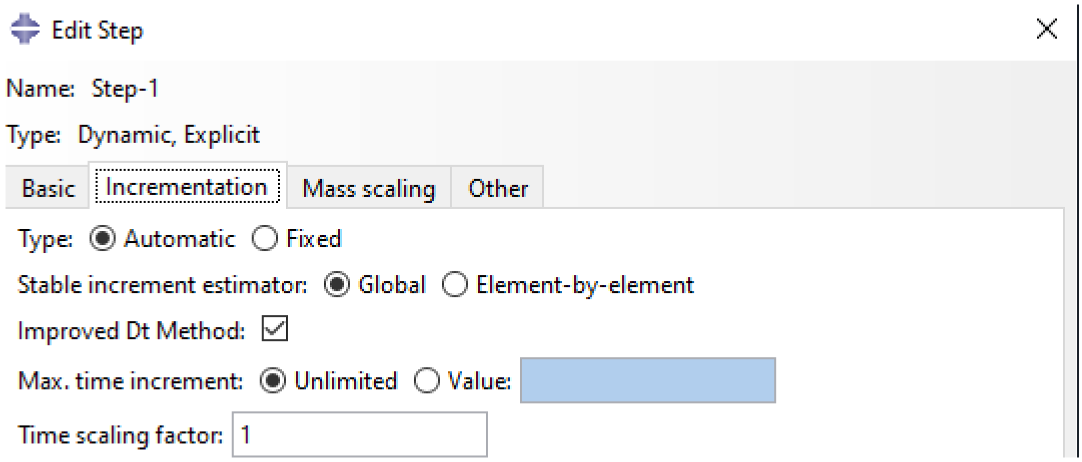

Figure 4.8: Dynamic Explicit step window in ABAQUS showing step incrementation

For the ballistic impact simulation, the automatic time step incrementation method was given, and the period was calculated as a period corresponding to the complete perforation of the plate, using the following relation:

Time for complete perforation of the target plate by KEP core = (Length of KEP core + Thickness of target plate)/ Velocity of KEP core.

The field and history outputs can also be specified in this step module. For the ballistic impact test simulation field outputs S (stress components and invariants), Mises (Mises equivalent stress), PE (Plastic strain components), PEEQ (Equivalent plastic strain), LE (Logarithmic strain components), U (translations and rotations), V (Translational and rotational velocities), A (Translational and rotational accelerations) and, STATUS (Status, some failure and plasticity models) were requested. The result-based criteria for a selected field output variable can be requested using STATUS field output. Under the status field output variable, the elements that meet the specified criteria are considered failed, and they are removed from model plots. The field output request window is shown in figure 4.9.

The kinetic and internal energy evolution output was requested through the history output request window (Figure 4.10). The output data is collected at 1000 evenly spaced time intervals.

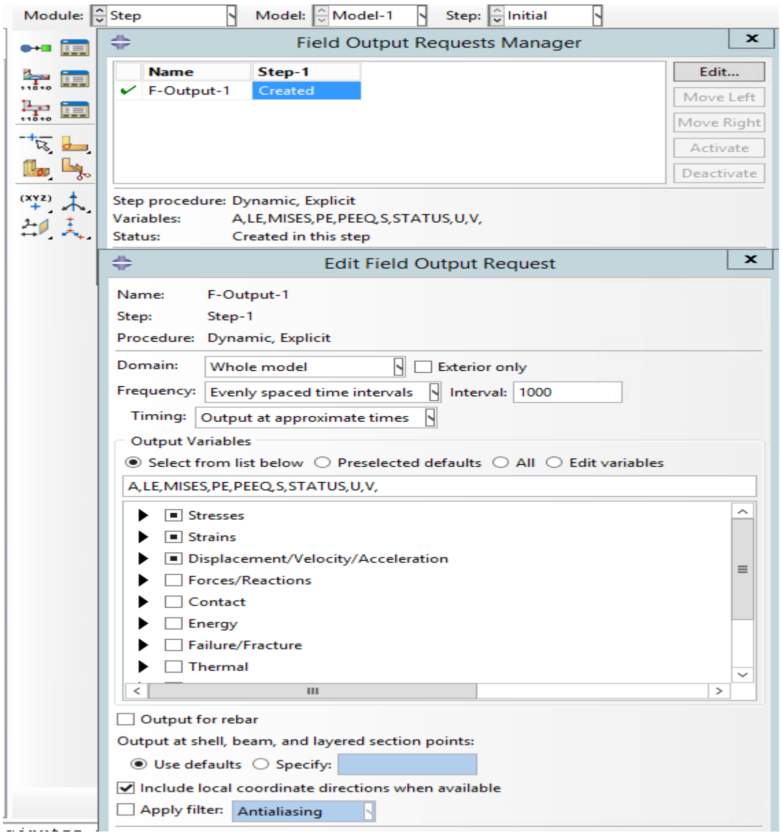

Figure 4.9: Field output window in the step module

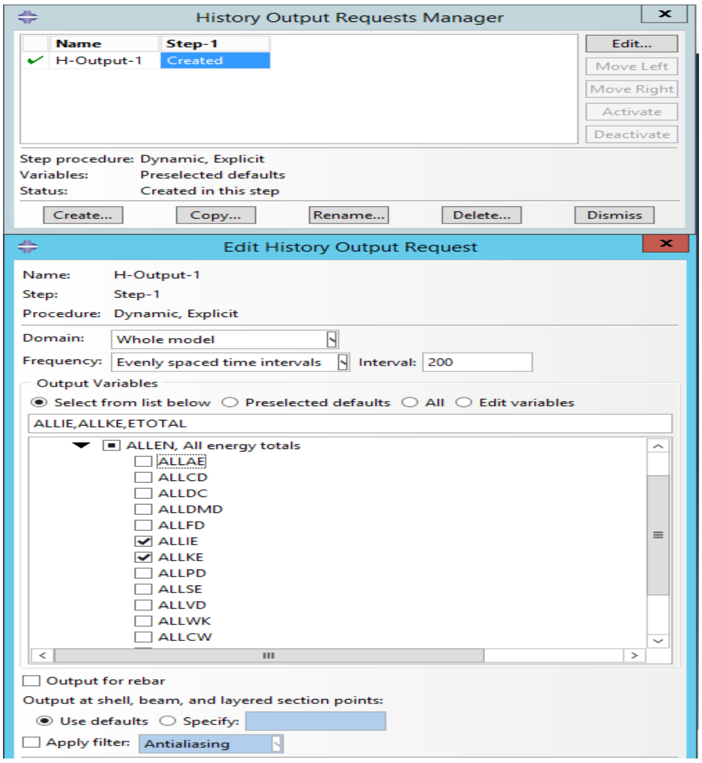

Figure 4.10: History output window in the step module

4.3.5. <u>Interaction Module</u>

The contact properties between elements can be assigned in the interaction module. General contact with normal behavior was set for the impact in one direction. AS the thermal softening effect is not considered in this study, heating effects are neglected.

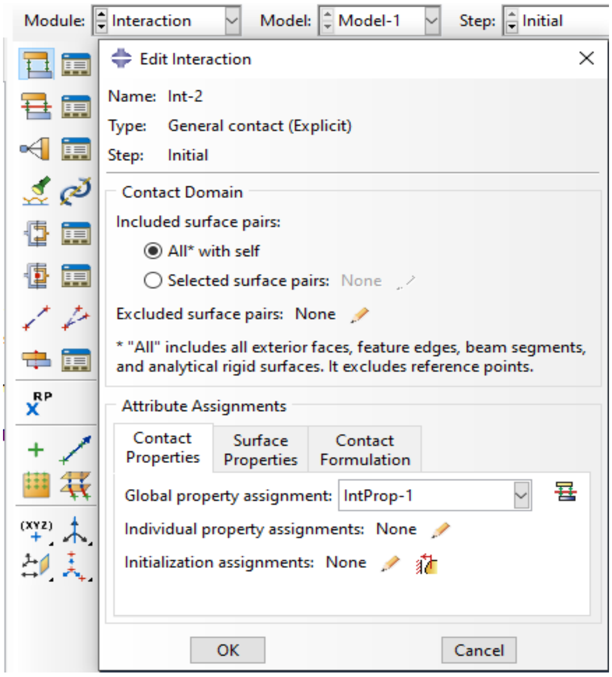

Figure 4.11: Interaction module window in ABAQUS

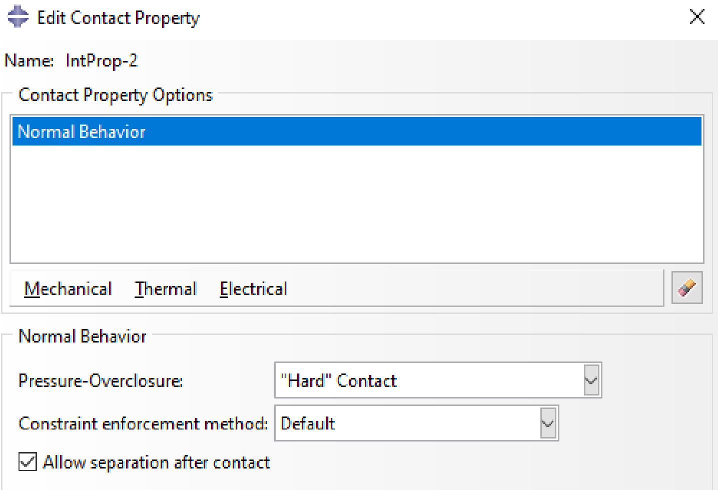

Figure 4.12: Contact property window in interaction module

4.3.6. Load Module

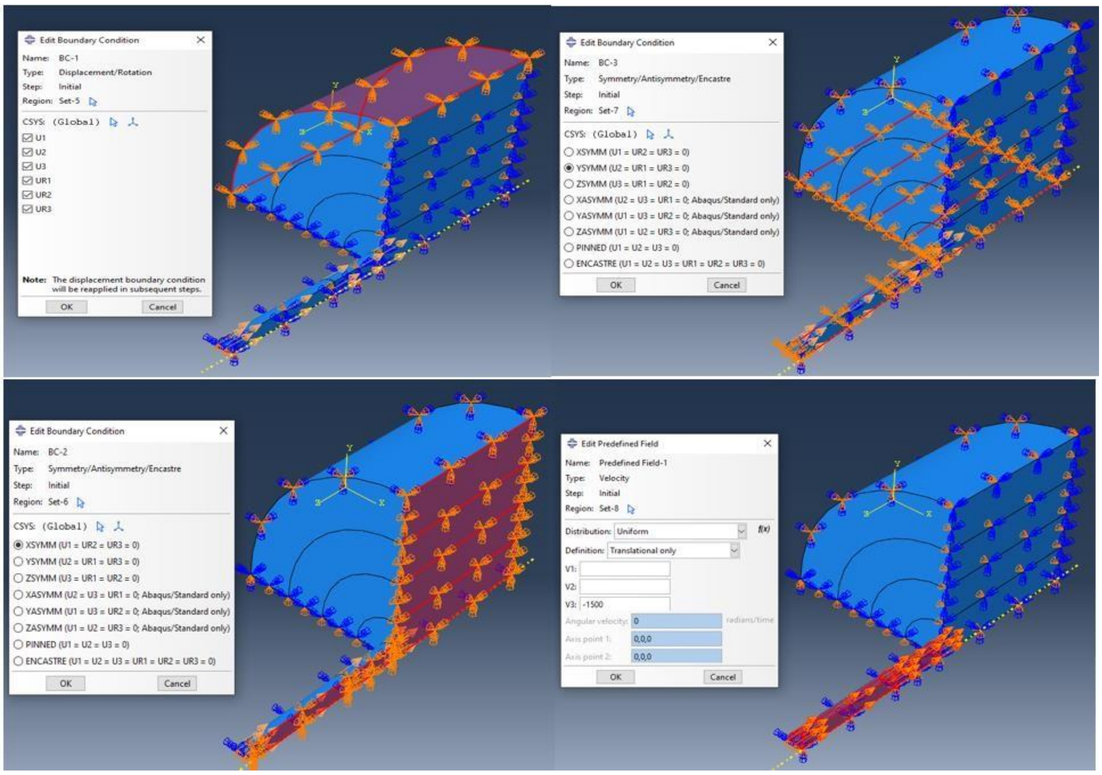

Figure 4.13: Load module showing boundary conditions and predefined field(velocity) applied to the model

Different loads, boundary conditions, and predefined fields can be assigned to the model in this module. Three boundary conditions are given for the KEP core- target plate system and provide velocity to the KEP core in the Z-direction. The outer circumference of the target plate was restricted to zero degrees of freedom in all three directions to ensure that the plate would not displace along with the high-velocity impact of the KEP core. The inner surfaces were restricted movement in their respective axis. The predefined field velocity was given to the KEP core in the negative Z-direction. The penetration performance analysis performed ballistic impact simulations at 1000 m/s, 1500m/s, and 2000m/s. Figure 4.13 shows the boundary conditions and velocity direction given to the model.

4.3.7. Mesh Module

The mesh is used to discretize the continuum into smaller elements. The quality of mesh plays a vital role in any FEM process. The ballistic impact test was modeled with simple cylindrical geometry to the KEP core and target plate. As the complexity

of geometry is less, the C3D8R (Continuum 3-dimensional eight node linear hexahedral brick) element, with reduced integration, which ABAQUS recommends for explicit dynamic problems, can be used.

The KEP core model meshed with a fine hex-structured mesh with an approximate global size of 0.001. The radius of the cylinder was divided into 30 elements. The total number of elements in the KEP core is 33750.

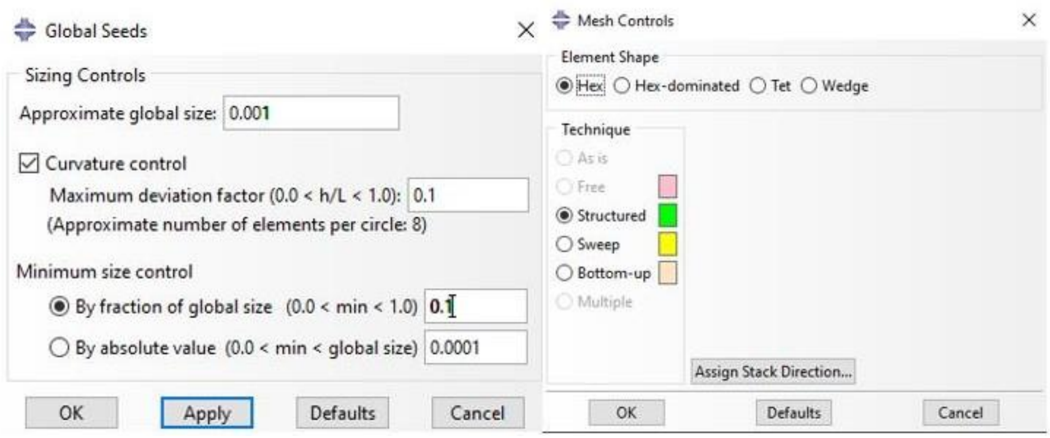

Figure 4.14: Mesh module in ABAQUS showing mesh controls for KEP Core Model

The target plate meshed with a hex-dominated element of the approximate global size of 0.005. The inner area where the impact concentration will happen is given finer mesh than the outer edge. The radial edge is divided into four segments of length 10mm,10mm,10mm, and 20mm from the center. The first edge from the center was divided into 30 elements and the subsequent edges into 20 parts. The segment arc connecting the divided edges was divided into 40 elements each.

The model's total number of elements and nodes is 59350 and 65976, respectively. The total number of variables after meshing and load module is 197928.

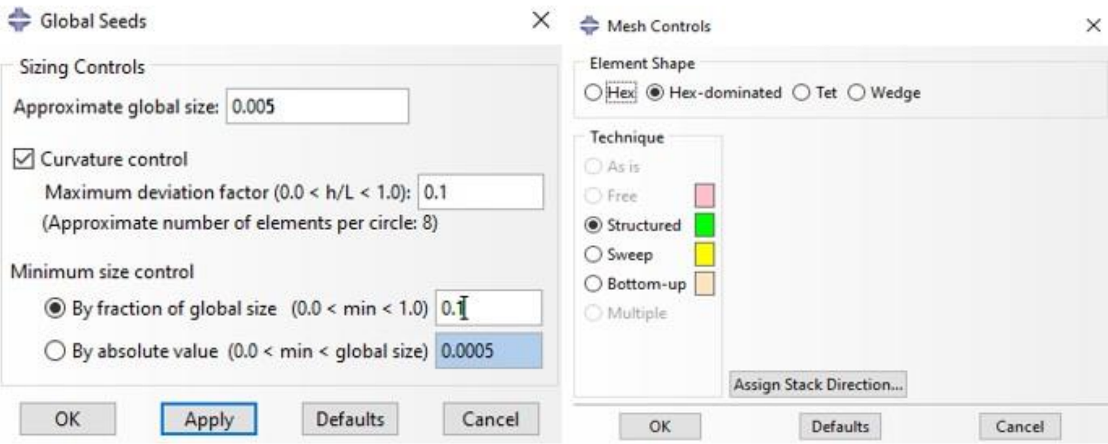

Figure 4.15:Mesh module in ABAQUS showing mesh controls for Target plate mode

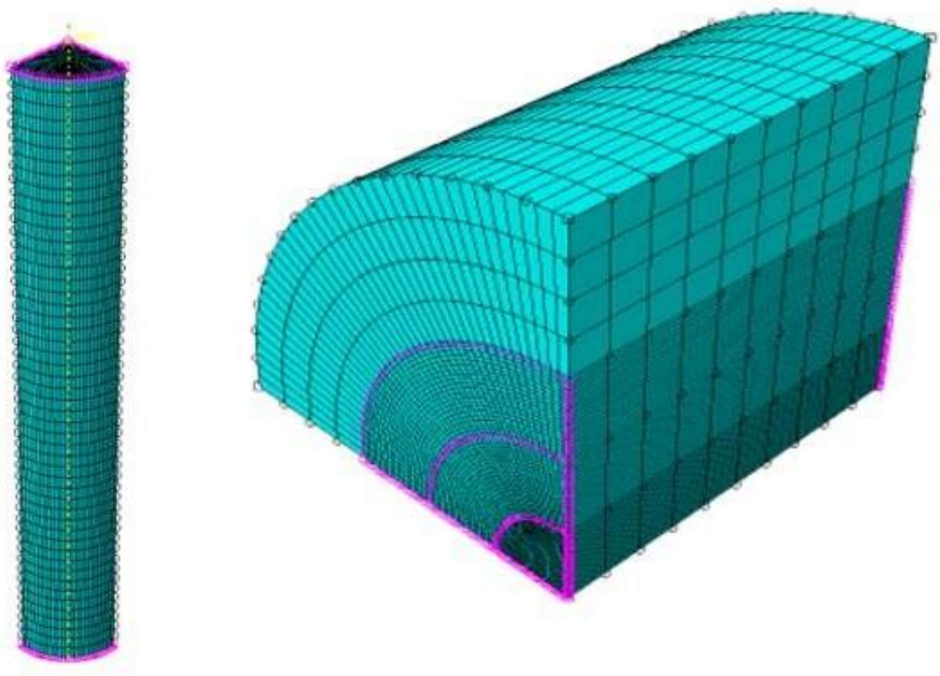

Figure 4.16: KEP Core and Target plate Models after meshing

4.3.8. Job Module

This is the final module that allows the submission of the analysis model. Explicit problems generally involve multiple mathematical models in the background to simulate the material and other damage models. Due to this complexity, such analysis takes a tremendous amount of time for computation. Parallelization is a hardware-dependent method to reduce computation time in ABAQUS. Instead of using a single core for a very complex problem, it allows the user to use multiple core processors simultaneously, reducing the time step. For the ballistic impact test in this work, 18 processors were used for each simulation. Figure 4.17 shows the job module window with the parallelization option.

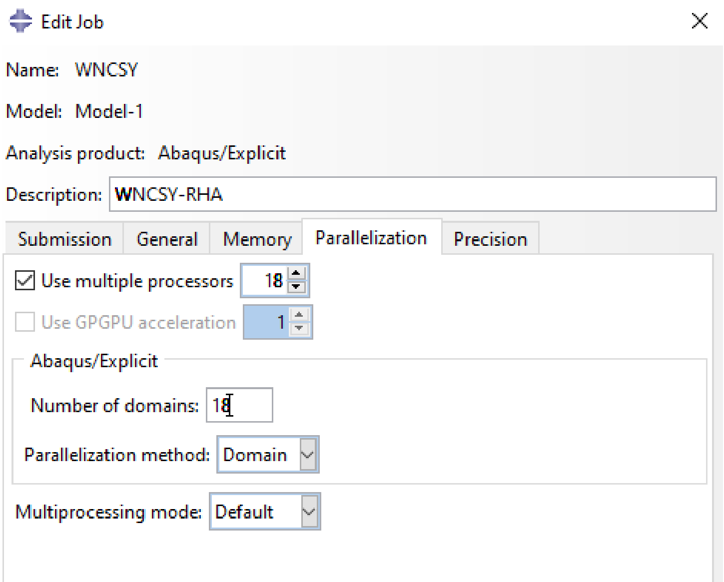

Figure 4.17: Job module in ABAQUS showing parallelization input

4.3.9. Visualization Module

This module displays the results of the analysis according to the user input. The different field outputs and history outputs can be analyzed. Animations of deformation, curve plotting, measurement of deformations, etc., are possible. Von mises stress, equivalent plastic strain, and energy evolution were analyzed for the ballistic impact analysis.

Chapter 5 RESULTS AND DISCUSSION

5.1. Experimental Results

5.1.1. Material Properties

The SEM images of as-received powders showed that the tungsten powders are long and dumbbell-shaped, Ni and Co powders are perfectly spherical, and Si and Y_2O_3 powders are irregular in form. The average size of received W, Ni, Co, and Si powders are 1.5, 50, 60, and 3.5 µm, respectively, as found from the SEM micrographs. Y_2O_3 powder dimension is less than 100 nm. The SEM micrographs of as-received powders are given in figure 5.1.

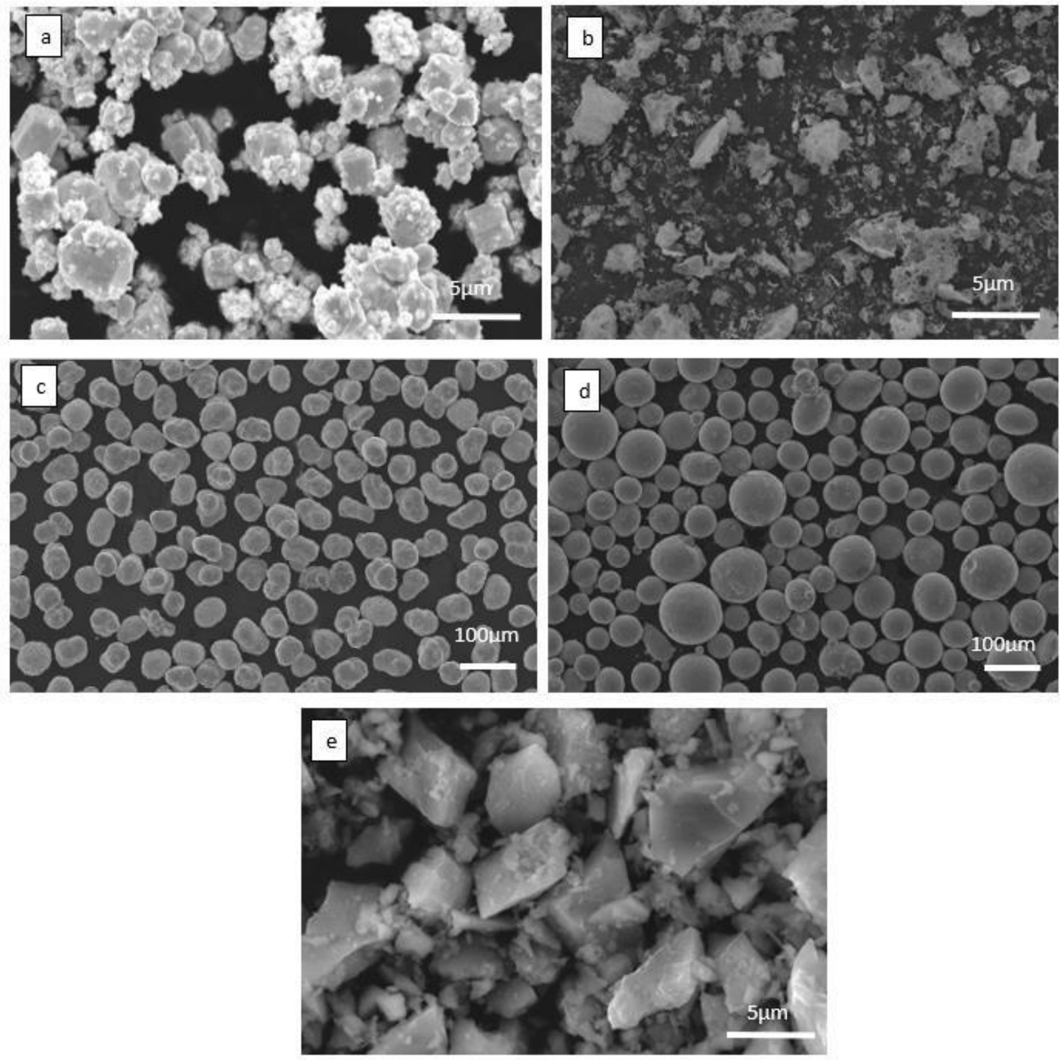

Figure 5.1: Morphology of as-received powders a. W powder, b. Y_2O_3 powder, c. Nickel powder, d. Cobalt powder, e. Silicon powder

From the study conducted by V.Suman et al. to find the effect of Si addition in WY, WNY, and WNCY alloys, the following conclusions were drawn as they are helpful for the intended study:

- Si addition resulted in fine and uniform particles after ball milling. WSY has shown finer particle size than the other two alloys. The powder mixture's crystallite size was reduced due to the strain hardening effect of Si. The ductile behavior of Ni and Co caused extensive plastic deformation to the particles; hence, large flaky particles were formed after milling.
- In WSY alloy, intermetallic WSi_2 formation was observed, while in WNSY and WNCSY, WSi_2 formation did not happen. This is because the particle crystallite size reaches nanocrystalline size in WSY due to "reactive intermixing" at the atomic level due to high strain energy during milling. The high brittleness of W, Si, and Y_2O_3 particles aided this substantial fragmentation. But in WNSY and WNCSY, the strain energy will be transferred to the Ni and Co soft particles, preventing the particle size reduction to the nanocrystal range.
- The intermetallic compound WSi_2 was transformed into W_5Si_3 after sintering in the WSY alloy. In the WNSY and WNCSY, the formation of SiO_2 was observed. The SEM images of sintered samples are shown in figure 5.2.
- Due to the poor compressibility of hard and brittle Y_2O_3, the density of all alloys is lower than pure W. The density of WSY (82.3%) is significantly less than that of WNSY (95.4%) and WNCSY (96.7%). The formation of SiO_2 prevented gas entrapment and blister formation in the WNSY and WNCSY, contributing to the high densification.
- The microstructure of WSY revealed large-sized pores due to the intermetallic compound formation restricting solid-state diffusion. In the WNSY and WNCSY alloys, large W particles are embedded into the Ni or Ni-Co matrix. Ni and Co promote the liquid phase sintering because they have a slightly lower melting point than the sintering temperature (Tm of Ni = 1455°C, Tm of Co = 1460°C).
- The Si addition helped densify alloy with fine and uniform microstructure and gave higher hardness. WSY has the highest hardness because of the intermetallic phase W_5Si_3. Due to the soft Ni and Co matrix, WNSY (4.5GPa) and WNCSY(4.1GPa) alloys have lower hardness compared to WSY(5.4GPa). Also, Si addition caused an increase in compression strength, but on the other side, it

decreased the ductility of alloys. The mechanical properties of all three alloys are given in table 5.1.

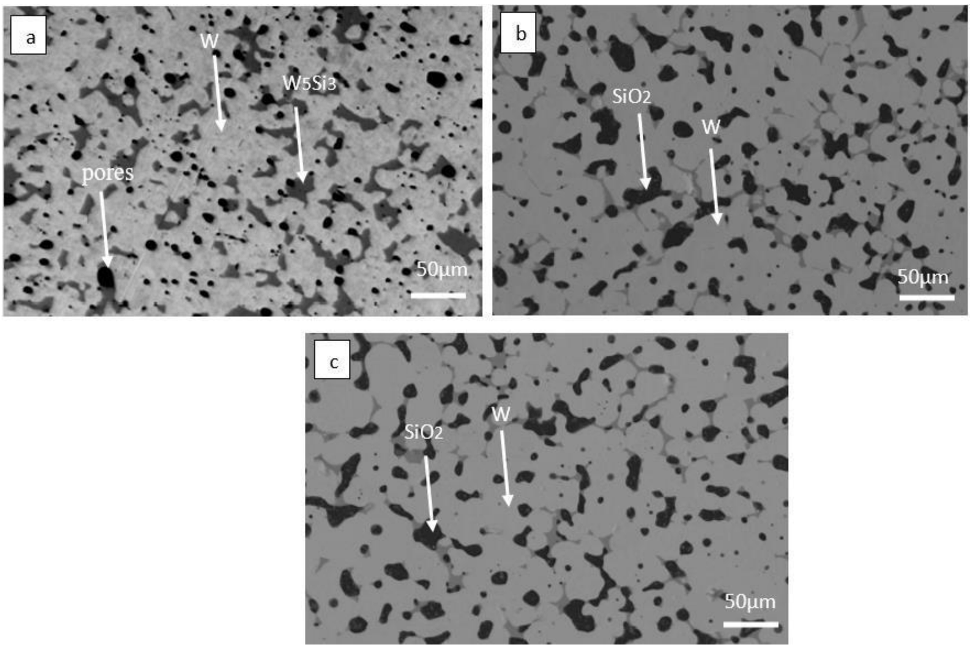

Figure 5.2: SEM images of samples after sintering- a. WSY, b. WNSY, c. WNCSY

Specimen	**Density (%theoretical)**	**Hardness (GPa)**	**Yield Strength (MPa)**	**Compressive strength (MPa)**	**Compressive strain at maximum compressive load (%)**
WSY	82.3	5.4	112	130	2
WNSY	95.4	4.5	1542	1723	15
WNCSY	96.7	4.1	1570	1757	13

Table 5.1: The density, hardness, yield strength, compressive strength, and compressive strain values of WSY, WNSY, and WNCSY alloys

The true stress- true strain graph was plotted from the compression test data, and the yield strength was found from the offset 0.2% strain. Figure 5.3 shows the true stress-true strain curves of three alloys.

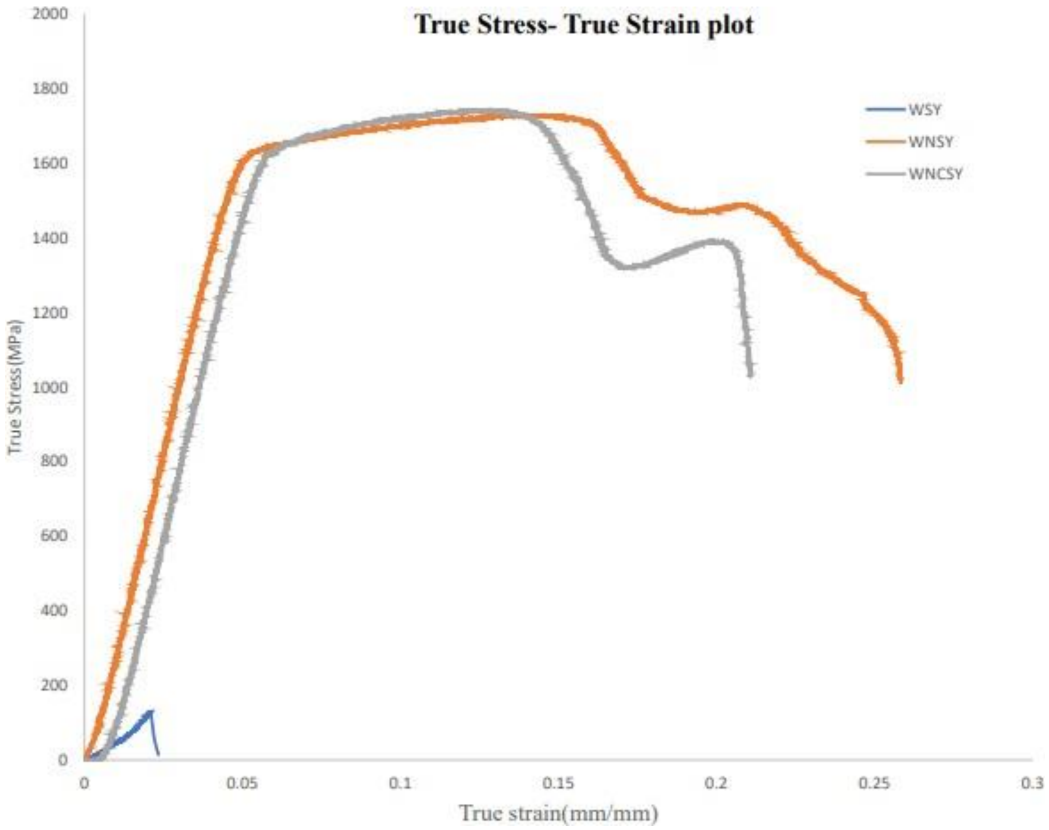

Figure 5.3: True Stress-True Strain plot of WSY, WNSY, and WNCSY alloys

The yield and compressive strength of WSY alloy are significantly less, and the ductility is just 2%. Si and Y_2O_3 addition in tungsten will cause brittleness and high hardness value, but the compression strength and ductility deteriorate. Hence this alloy is not fit to act as a KEP material, as it won't sustain high compressive strain during impact and its brittle nature is not suitable for this application. The addition of ductile Ni and co and Si and Y_2O_3 improved the compression strength with moderate strain. So WNSY and WNCSY can be considered for further high strain rate experiments and simulations as they have very high yield strength and ductility. V Suman. et al. have concluded that the fracture surface after compression test has shown that these alloys have undergone brittle fracture with dimples on the surface.

JC material model parameters must be found from the quasi-static compression and SHPB tests for the numerical simulation. So, for finding the parameters B and n, the ln (σ-A) and ln ε graphs are plotted for WNSY and WNCSY alloys. The curve was fitted using a first-order linear regression trendline, and the slope represents the strain hardening exponent, n, and the intercept is ln (B).

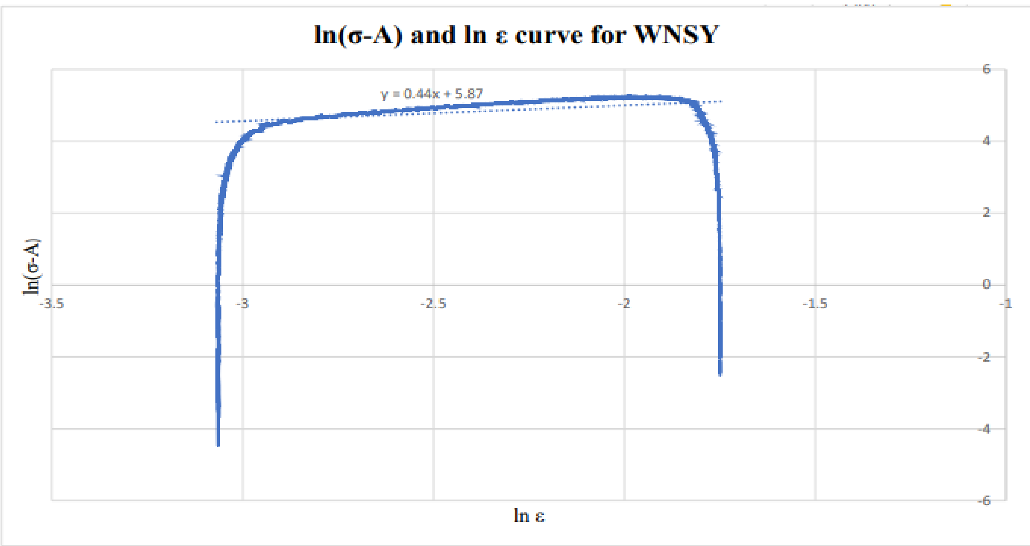

Figure 5.4: ln(σ-A) - ln ε curve for WNSY

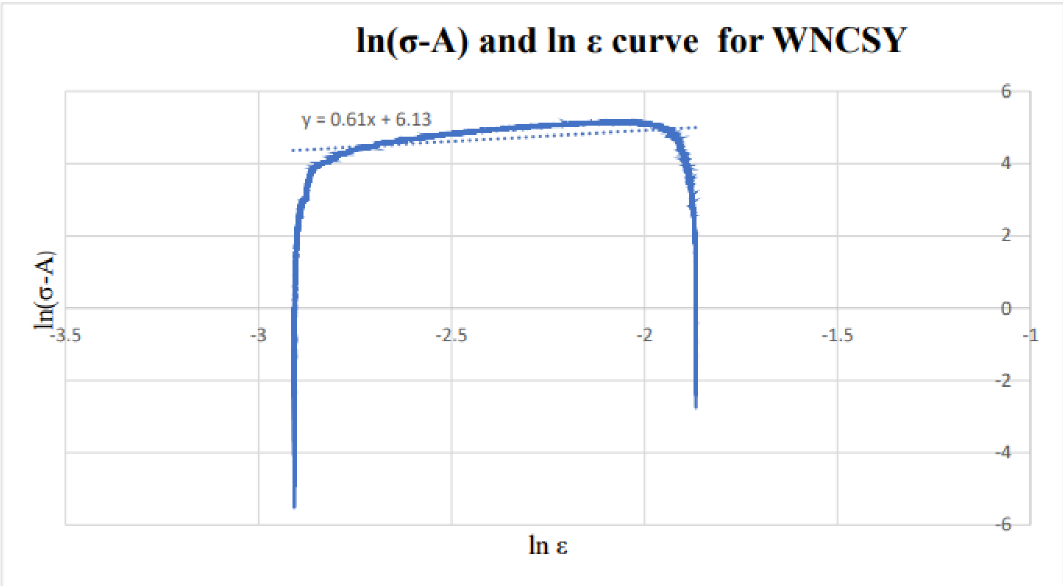

Figure 5.5:ln(σ-A) - ln ε curve for WNCSY

The following (Table 5.2.) JC material constants were thus found from the compression test at reference strain rate, 0.1/sec:

Alloy	A (MPa)	B (MPa)	n
WNSY	1542	354.25	0.44
WNCSY	1570	459.43	0.61

Table 5.2: JC constants obtained from compression test at strain rate 0.1/sec

The JC damage coefficient D_1 was given the strain at failure assuming D_2 and D_3 as zero (neglecting triaxiality dependence).

5.1.2. SHPB Test Results

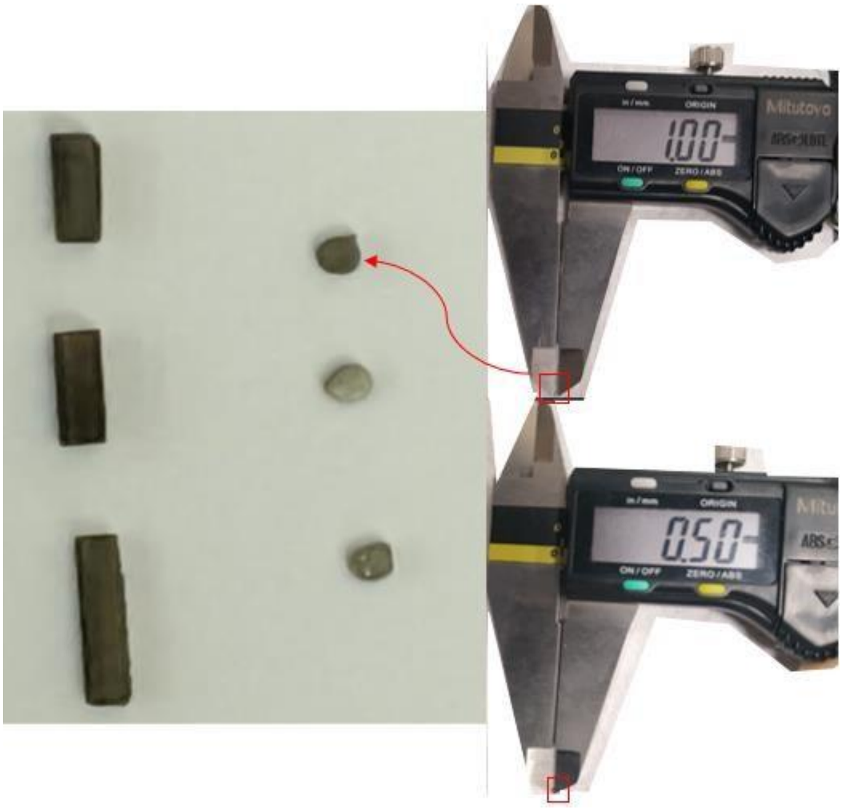

Figure 5.6: Samples cut by using ECOCUT CNC Wire EDM and diamond blade cutter

The samples were prepared according to the specified dimensions for the test. Images of samples used for the SHPB test are shown in figure 5.6. The test was performed on three alloys at three pressures - 2 bar, 4 bar, and 6 bar and each test was performed three times. The voltage output data was collected from the oscilloscope and input into the MATLAB open tool described in the previous section. The bar specifications and calculation parameters used are given in table 5.3:

Bar material	**Density (Kg/m^3)**	**Youngs modulus (MPa)**	**Diameter of bars (mm)**	**Gage factor (ε/V)**	**Sampling frequency (MHz)**
Maraging steel	8100	210000	3	.0021	62.5

Table 5.3: Input parameters to the SHPB analysis tool

The averaged value of strain rates at 2, 4, and 6 bar pressures for each alloy and the True stress -True strain curve, Engineering stress-engineering strain curve, Engineering stress-time curve, Engineering strain – time curve, Engineering strain rate-time curve, and the Engineering strain rate – engineering strain curves are plotted. The results obtained from the SHPB result analysis open tool are given below in figures 5.7-5.12.

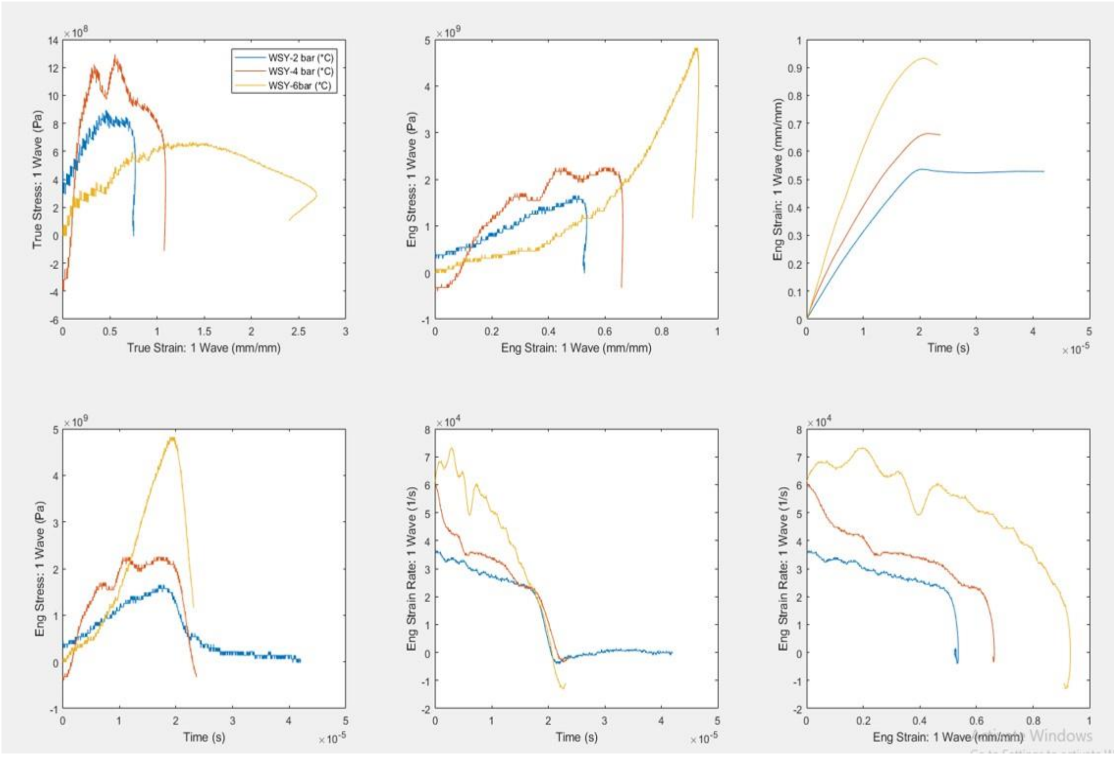

Figure 5.7:True stress -True strain curve, Engineering stress-engineering strain curve, Engineering stress- time curve, Engineering strain – time curve, Engineering strain rate-time curve, and the Engineering strain rate – engineering strain curve of WSY under 2,4 and 6 bar pressure

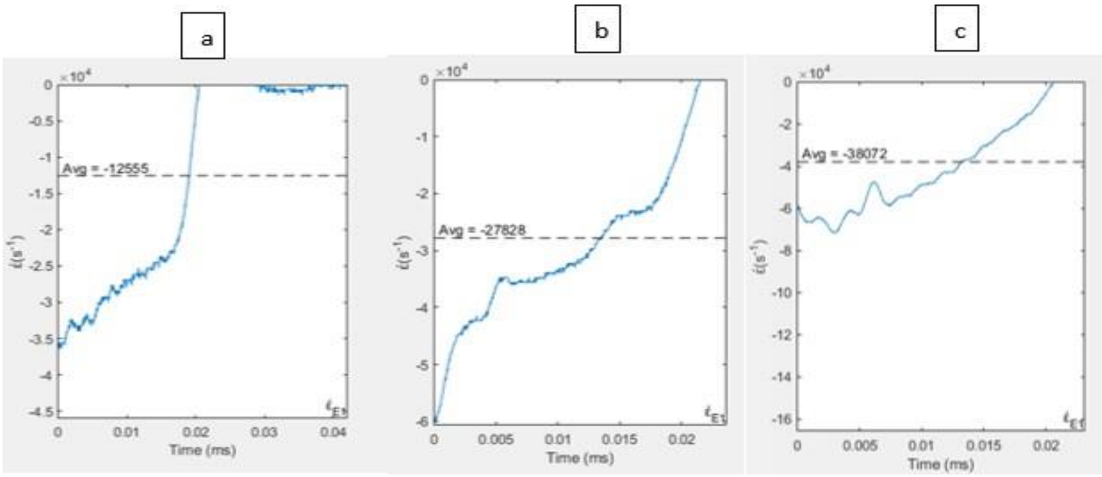

Figure 5.8: Averaged strain rate values at a. 2bar, b. 4bar and c. 6 bar of WSY alloy

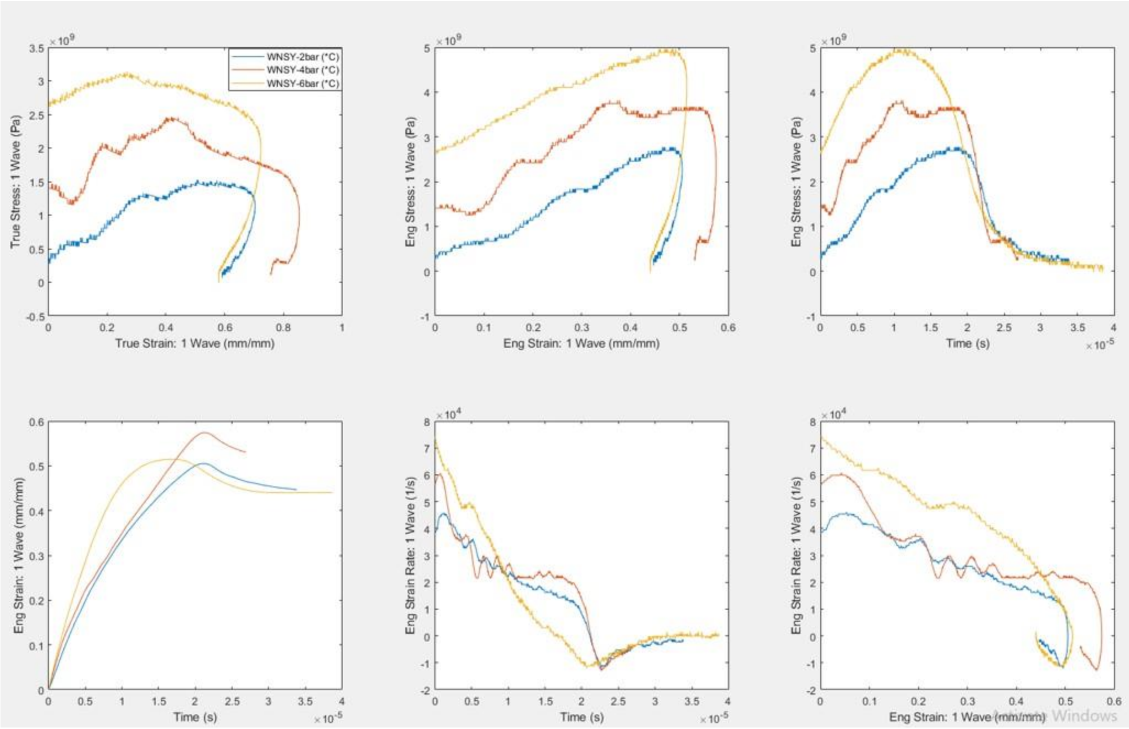

Figure 5.9:True stress -True strain curve, Engineering stress-engineering strain curve, Engineering stress- time curve, Engineering strain – time curve, Engineering strain rate-time curve, and the Engineering strain rate – engineering strain curve of WNSY under 2,4and 6 bar pressure

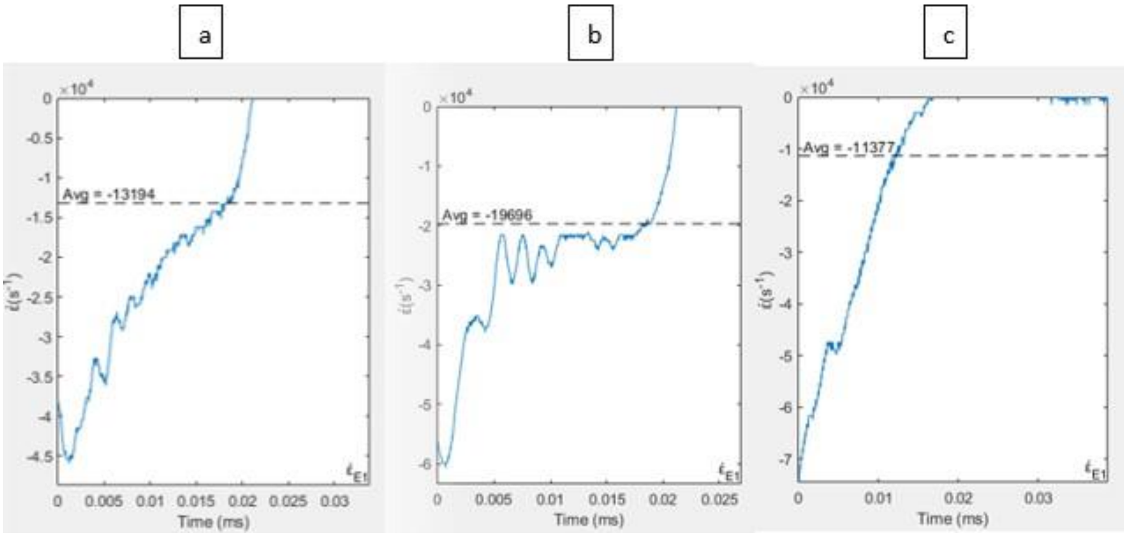

Figure 5.10:Averaged strain rate values at a. 2bar, b. 4bar and c. 6 bar of WNSY alloy

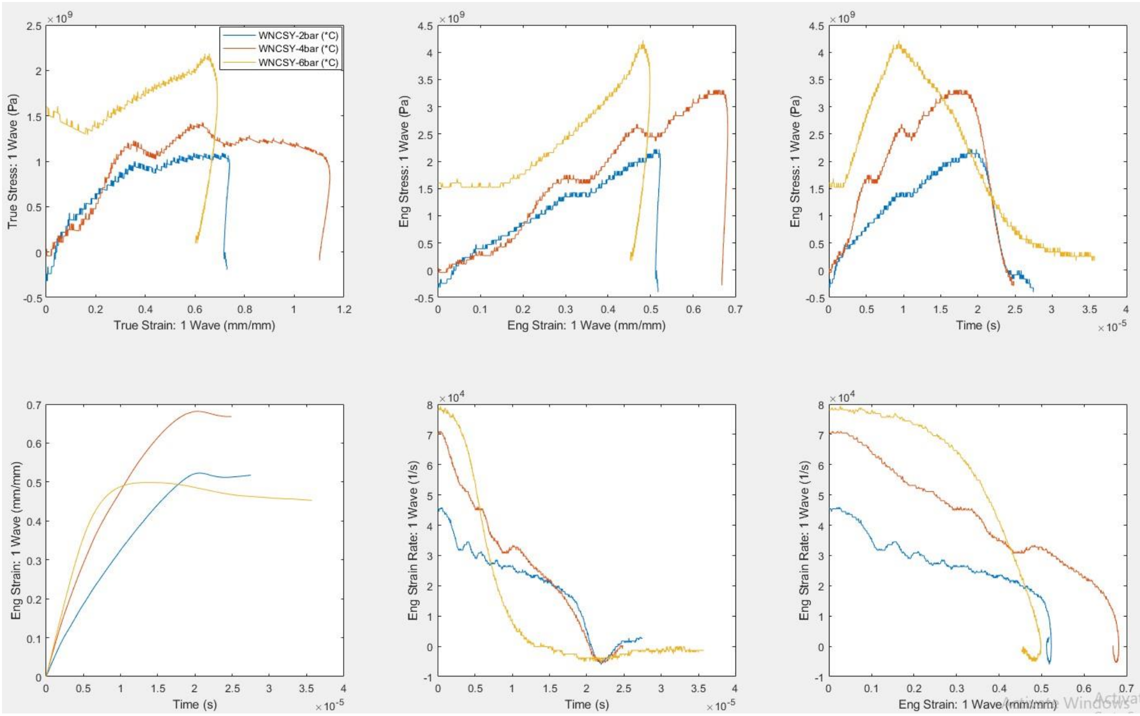

Figure 5.11:True stress -True strain curve, Engineering stress-engineering strain curve, Engineering stress- time curve, Engineering strain – time curve, Engineering strain rate-time curve, and the Engineering strain rate – engineering strain curve of WNCSY under 2,4 and 6 bar pressure

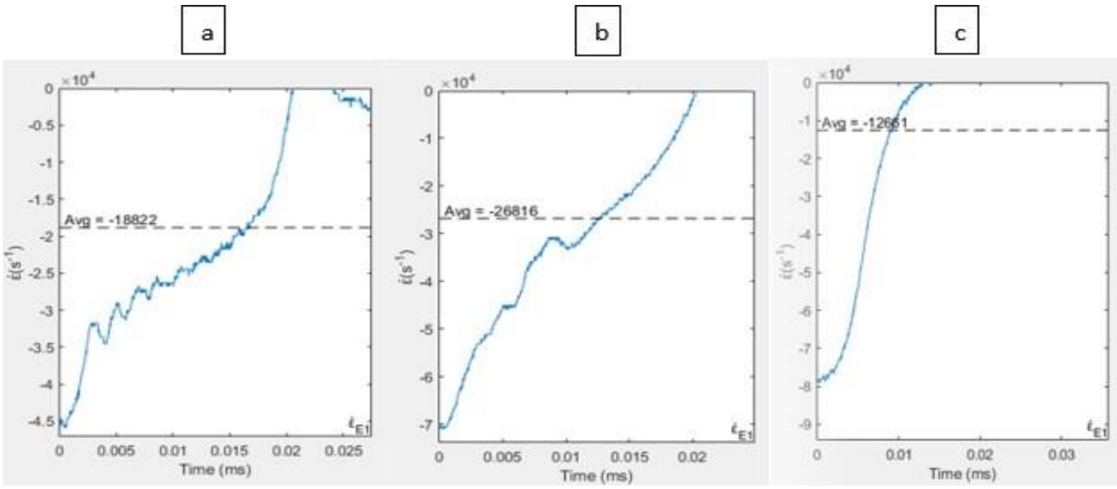

Figure 5.12:Averaged strain rate values at a. 2bar, b. 4bar and c. 6 bar of WNCSY alloy

The uniaxial dynamic compressive stress-strain curves plotted can be analyzed to understand the deformation behavior theoretically. The strain rate is either decreasing or constant at all strain rates for all three alloys, which gives a hint that strain localization is not happening. Only flow softening is happening even at higher strain rates. So the chance of adiabatic shear banding is vesignificantlyess. The dynamic compression strength and failure strain are tabulated below:

Alloy	Averaged Strain rate (s^{-1})	Dynamic compression strength (MPa)	Failure Strain(mm/mm)
WSY	1255	1410	0.58
	27828	2100	0.65
	38072	4800	0.9
WNSY	13194	2960	0.51
	19696	3730	0.57
	11377	4950	0.52
WNCSY	18822	2200	0.51
	26816	3220	0.68
	12661	4350	0.49

Table 5.4: Dynamic compression strength and failure strain data for WSY, WNSY, and WNCSY at different strain rates

The higher dynamic compression strength and lower failure strain exhibited by all three alloys ensure that these materials meet the launch requirement for ballistic impact. As the WSY alloy did not have enough compressive strength and showed brittle nature due to the presence of Si and Y_2O_3, it is not considered further for the application. Hence, the JC parameter C was calculated from the true stress-true strain curves at different strain rates. As explained in section 4.3.2, $\sigma / (A + B\,\varepsilon^n)$ - ($\ln \acute{\varepsilon}^*$) curves at three different strain rates were plotted (Figure5.13-5.14). The slope of the fitted curve is the coefficient of strain rate hardening C.

Hence the C value obtained from the $\sigma / (A + B\,\varepsilon^n)$ - ($\ln \acute{\varepsilon}^*$) curve of WNSY and WNCSY alloys is tabulated below:

Alloy	C (Coefficient of strain rate hardening)
WNSY	0.0243
WNCSY	0.015

Table 5.5: JC parameter C received from SHPB data

The JC damage parameter D_4 is the strain rate dependent coefficient but turns out to be negligible at very high strain rates (of order $>10^4$). So, the value is taken as zero.

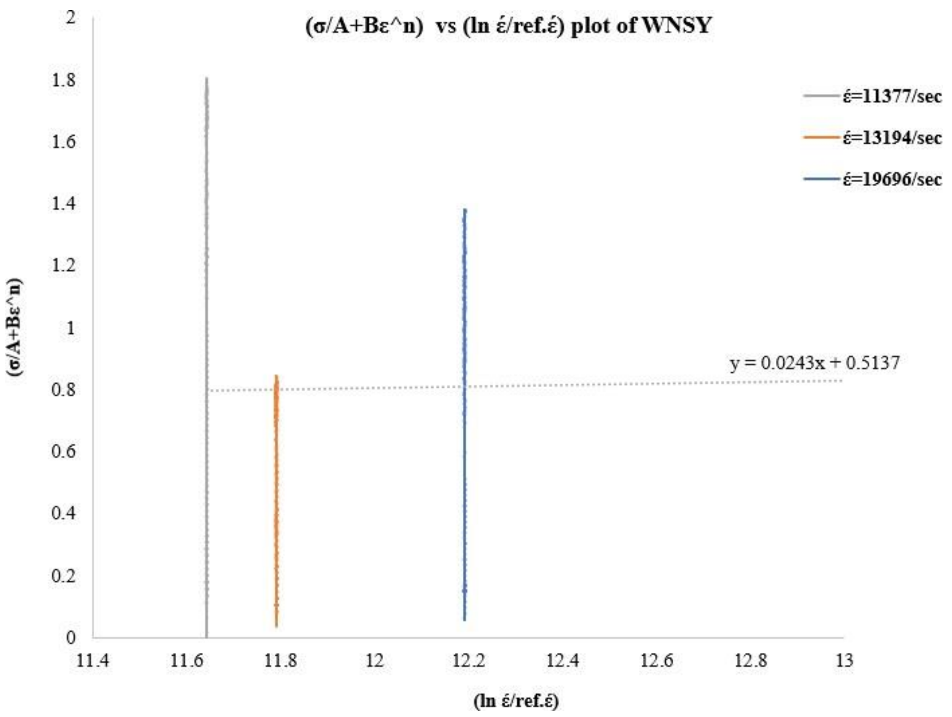

Figure 5.13:σ /(A+Bε^n) - (lnέ*) curve of WNSY

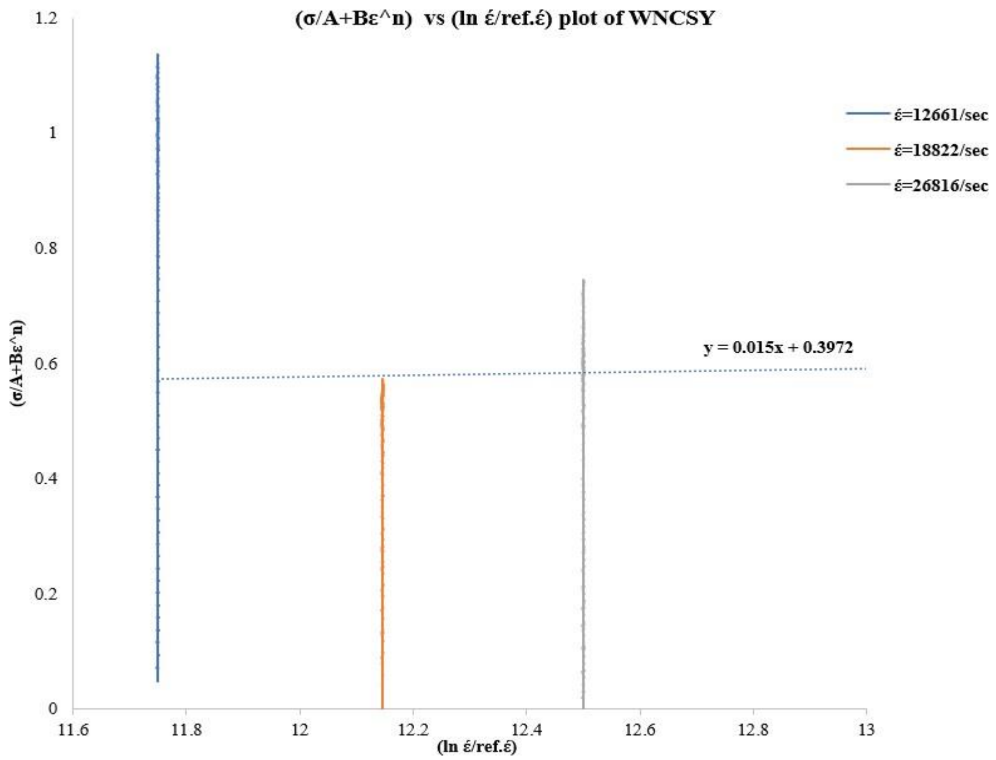

Figure 5.14:σ /(A+Bε^n) - (lnέ*) curve of WNCSY

Microstructure analysis

The microstructure of deformed samples was observed using both optical and SEM micrographs. The micrographs are shown in figures 5.15 - 5.20.

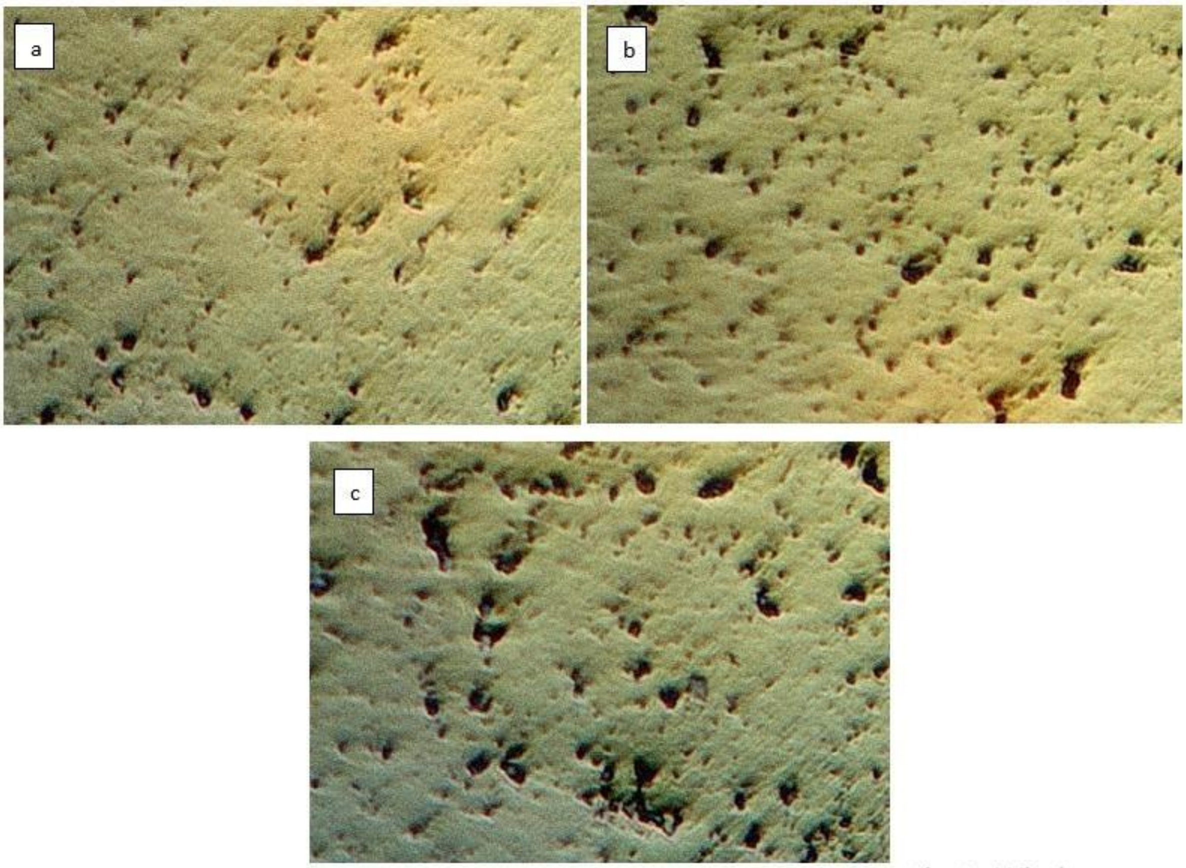

Figure 5.15:Optical micrographs at 40X magnification of WSY after SHPB test under a. 2 bar, b. 4 bar, and c. 6 bar pressure.

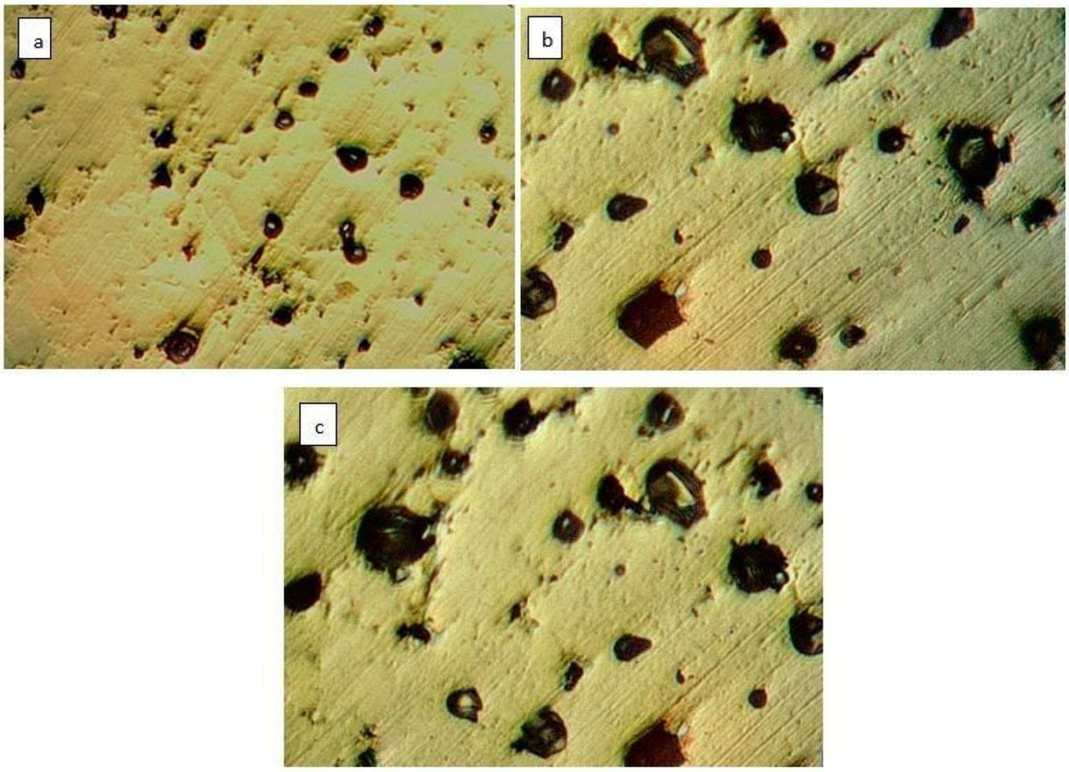

Figure 5.16:Optical micrographs at 40X magnification of WNSY after SHPB test under a. 2 bar, b. 4 bar, and c. 6 bar pressure.

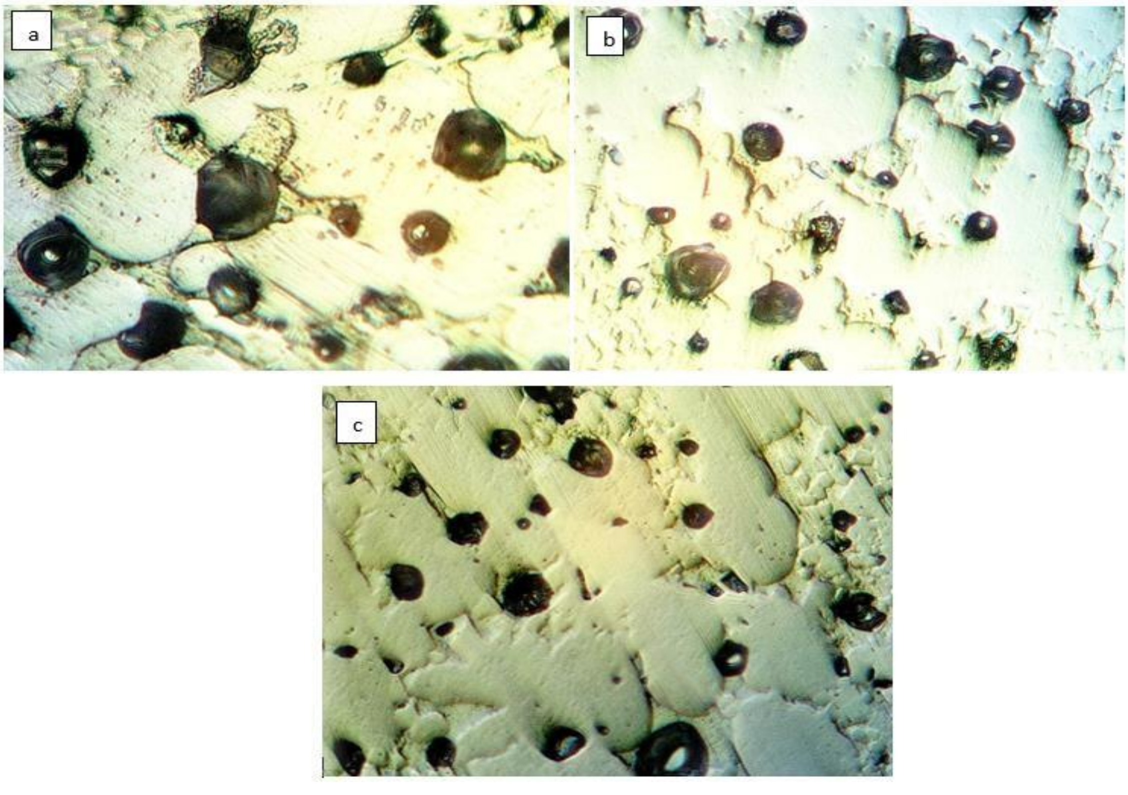

Figure 5.17:Optical micrographs at 40X magnification of WNCSY after SHPB test under a. 2 bar, b. 4 bar, and c. 6 bar pressure.

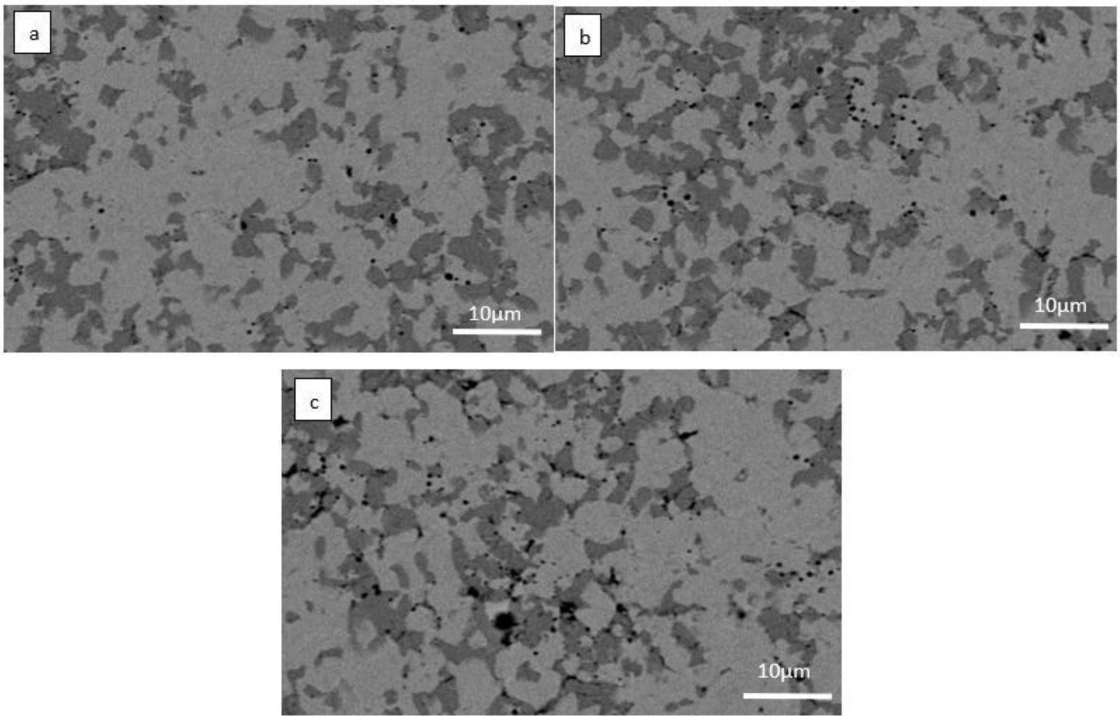

Figure 5.18:SEM micrograph of WSY after SHPB test under a. 2 bar, b. 4 bar, and c. 6 bar pressure.

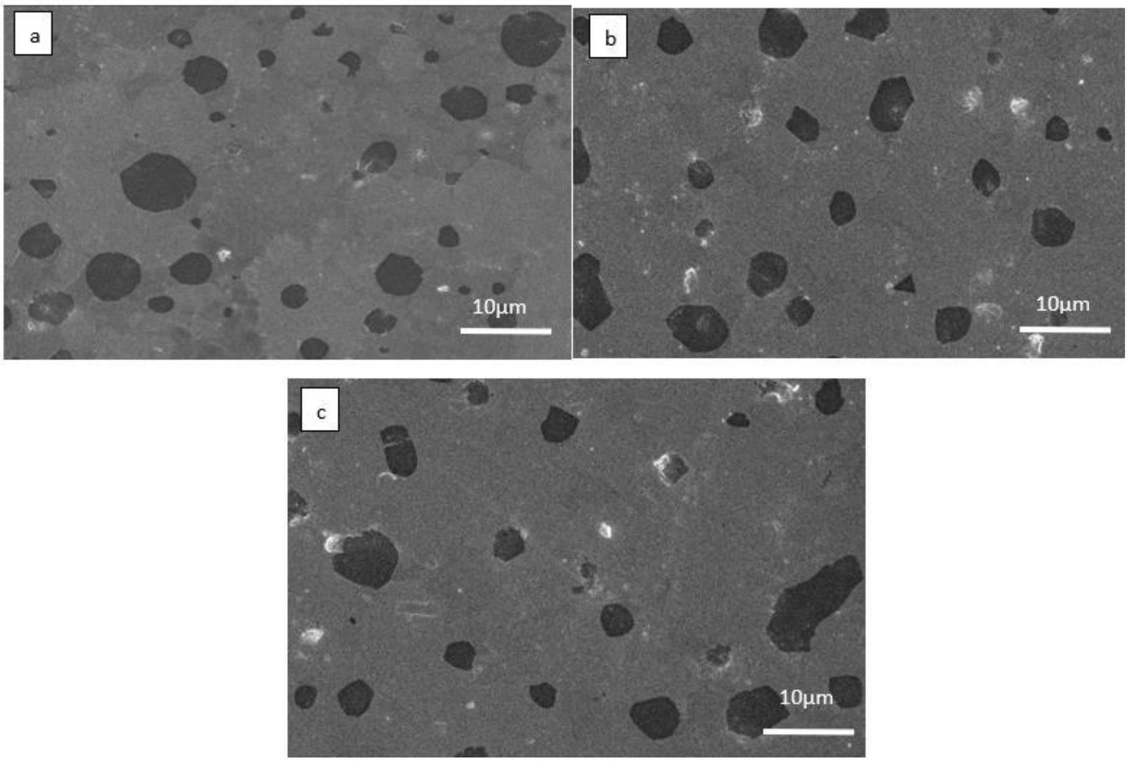

Figure 5.19:SEM micrograph of WNSY after SHPB test under a. 2 bar, b. 4 bar, and c. 6 bar pressure.

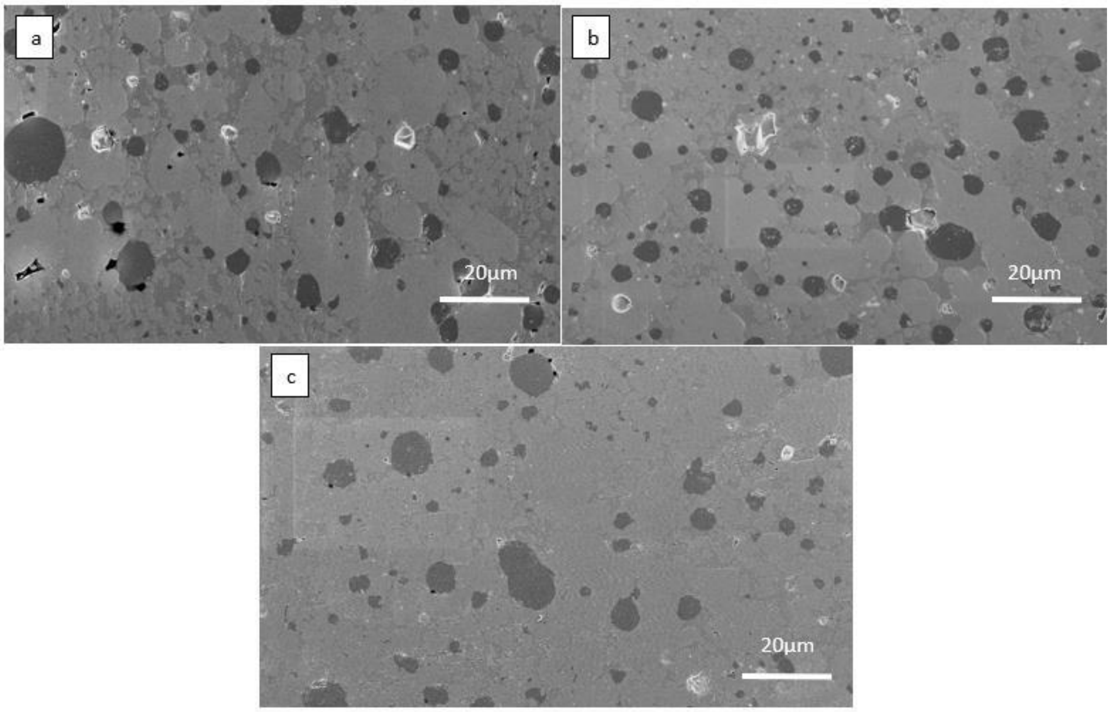

Figure 5.20:SEM micrograph of WNCSY after SHPB test under a. 2 bar, b. 4 bar, and c. 6 bar pressure.

The optical micrographs revealed the deformation on the surface. In WSY alloy, the number and size of pores increased visibly after deformation under higher pressures. This increased number of pores can be the fracture initiation point as it has shown brittle fracture during quasi-static compression and in the SHPB test. From the SEM images (Figure 5.18), it is evident that the pores along with W_5Si_3 intermetallic compound regions are more in the area in the 6-bar pressure applied sample than the other two. But in WNSY and WNCSY alloy's optical micrographs, the black region size increased drastically after high-pressure deformation. The black region can be pores combined with the SiO_2 compound, observed in the SEM image (Figure 5.19,5.20). The Ni and Ni-Co matrix has deformed considerably and seems to be penetrated in between W grains. This will cause interfacial debonding between W particles. After testing at 2 bar pressure, the grain boundaries of the W, Ni, and Ni-Co matrix were distinguishable. But after testing under higher pressures, the boundaries are not separate. The W particles must have deformed considerably and compressed together with the matrix. The matrix phase increases in area as the pressure increases, indicating that it took up the load and exhibited a ductile deformation. No fractures or cracks were observed in the three alloys, even though the WSY alloy fractured into pieces after the SHPB test. Pores must have initiated the sudden rupture. But the conclusion cannot be justified without performing elemental distribution study post deformation. As supported by the SHPB test plots, any sign of strain localization or adiabatic shear banding was not observed in the microstructure. Hence the possibility of adiabatic shear failure in these alloys can be eliminated. As the WNSY and WNCSY alloys sustained high pressure with a ductile deformation behavior, they are considered for the further simulation study.

5.2. Ballistic Impact Test Simulation Results and Analysis

The ballistic impact simulation was performed with the modeled geometry and the following (Table 5.6) material properties. The WSY alloy was not considered as it has proven to be not fit for the intended application from the quasi-static compression test itself.

	RHA Steel	**WNSY**	**WNCSY**
Density (Kg/m^3)	7830	17217	17149
A(MPa)	792	1542	1570
B(MPa)	510	354.25	459.43
n	0.26	0.44	0.61
C	0.014	0.0243	0.015
m	1	1	1
D1	0.05	0.26	0.23
D2	3.44	0	0
D3	2.12	0	0
D4	0.002	0	0
D5	0.61	0	0

Table 5.6: Material properties used for simulation of ballistic impact

The ballistic impact simulation was performed for both the alloys taking RHA Steel [40] as the target plate, under the following velocity and step time (Table 5.7):

Simulation no.	KEP Core material	Velocity (m/s)	Step time (microseconds)
Simulation 1	WNSY	1000	100
Simulation 2	WNSY	1500	66.6
Simulation 3	WNSY	2000	50
Simulation 4	WNCSY	1000	100
Simulation 5	WNCSY	1500	66.6
Simulation 6	WNCSY	2000	50

Table 5.7: Simulations performed with velocity and step times used

All the simulations resulted in the combined deformation of both the KEP Core and the target plate. After the simulations, the stress (Von mises) and equivalent plastic strain contours are given in figures 5.21-5.32. The kinetic and internal energy evolution, Stress (Von mises)-Time, and Equivalent plastic strain- time plots are shown in Figures 5.33-5.38. Stress value is the averaged value from all the elements (33750 elements) of KEP Core. The equivalent plastic strain of the centermost element (element 22515) of KEP Core is considered.

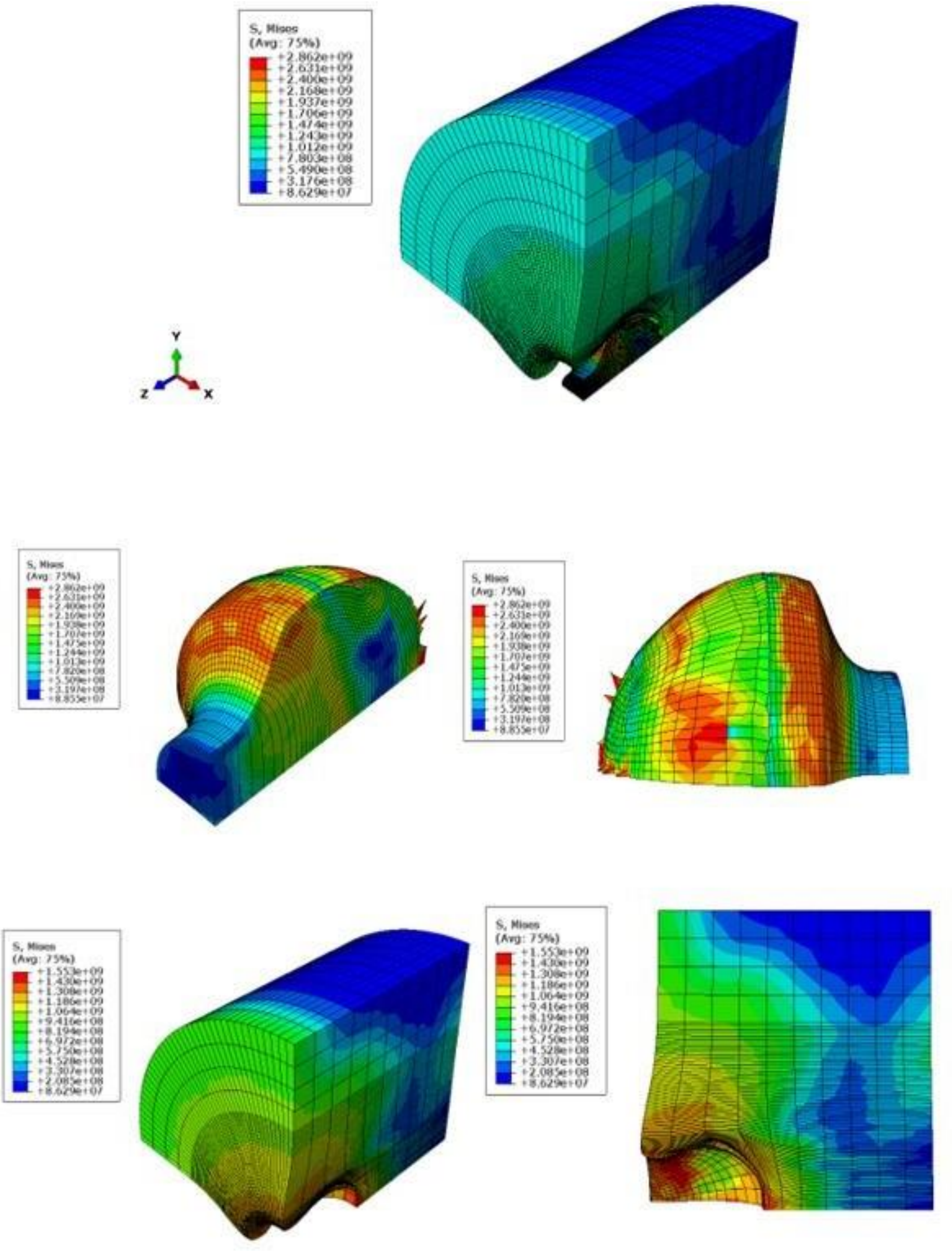

Figure 5.21:Von Mises stress contour generated after WNSY KEP Core and RHA Steel target plate at 1000m/s

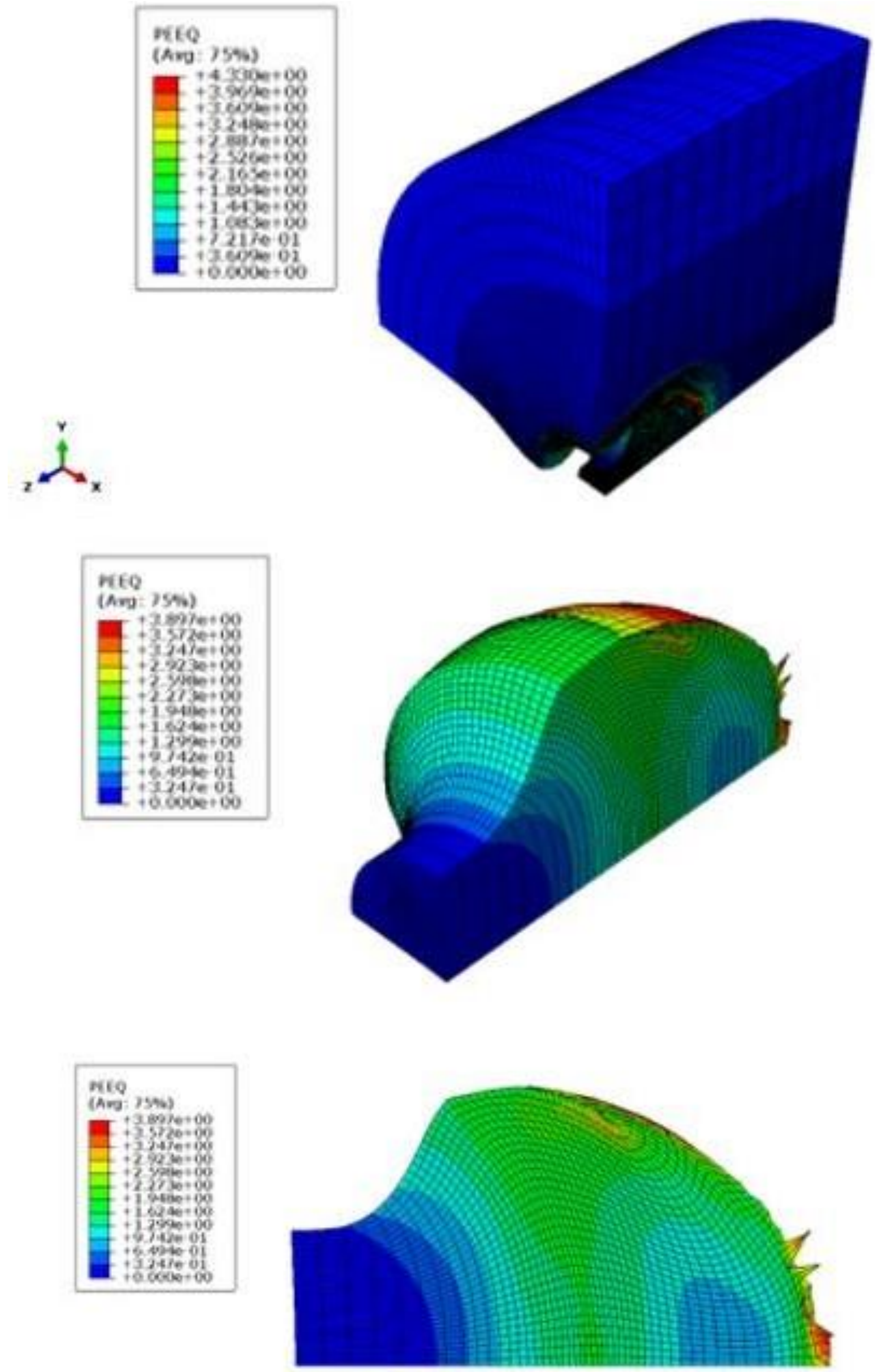

Figure 5.22:Equivalent plastic strain profile after WNSY KEP Core and RHA Target plate at 1000/s

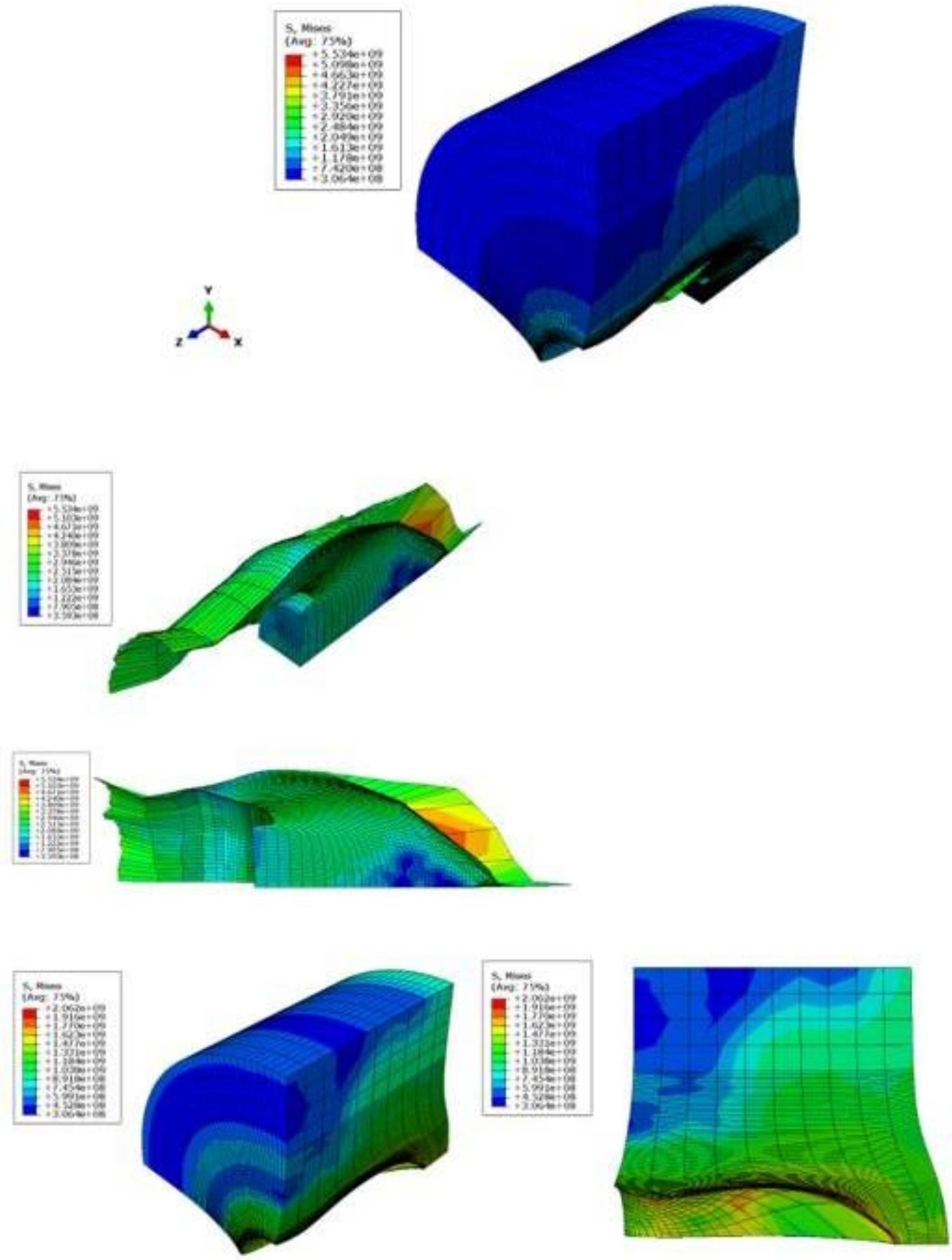

Figure 5.23:Von Mises stress contour generated after WNSY KEP Core and RHA Steel target plate at 1500m/s

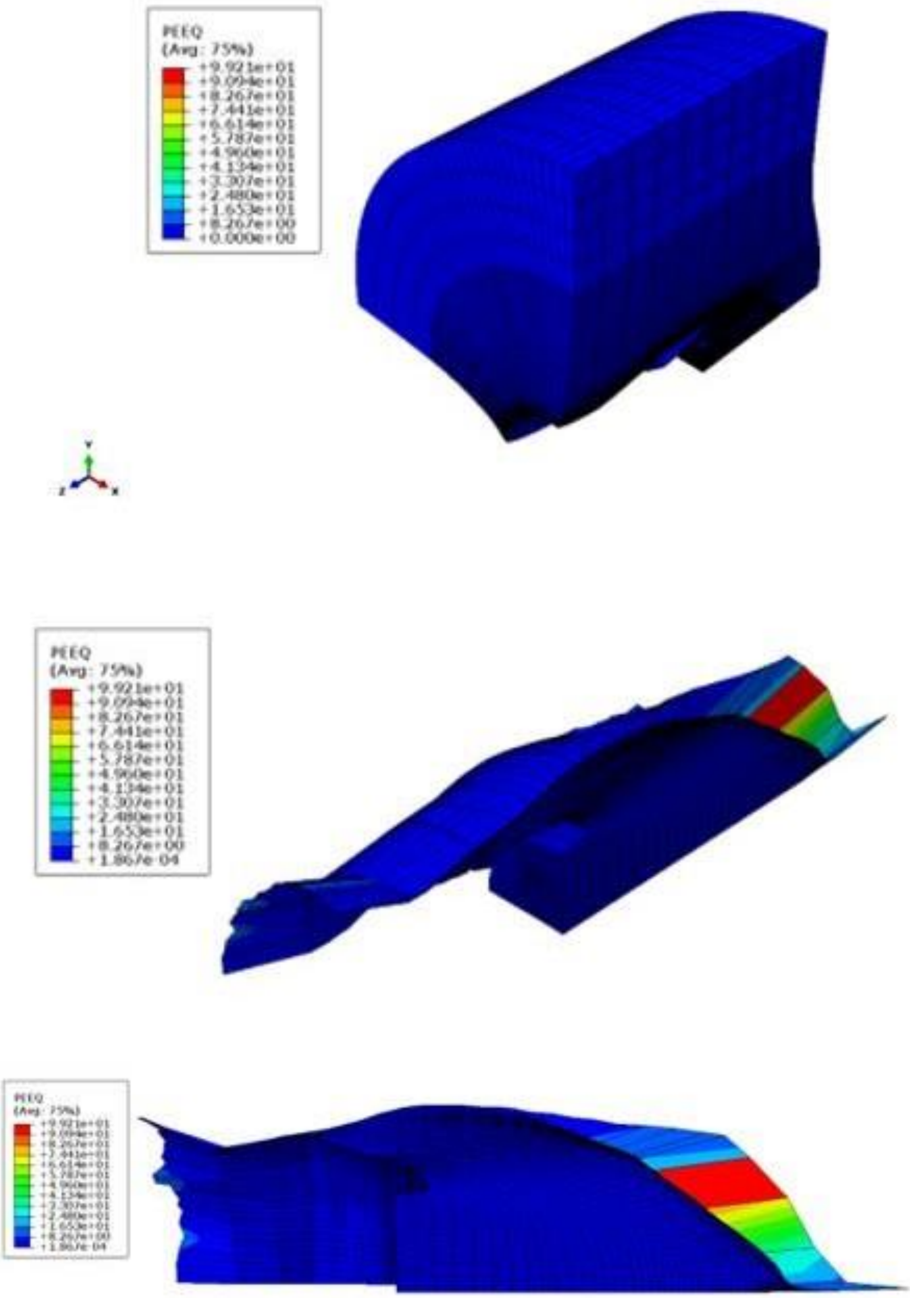

Figure 5.24:Equivalent plastic strain profile after WNSY KEP Core and RHA Target plate at 1500m/s

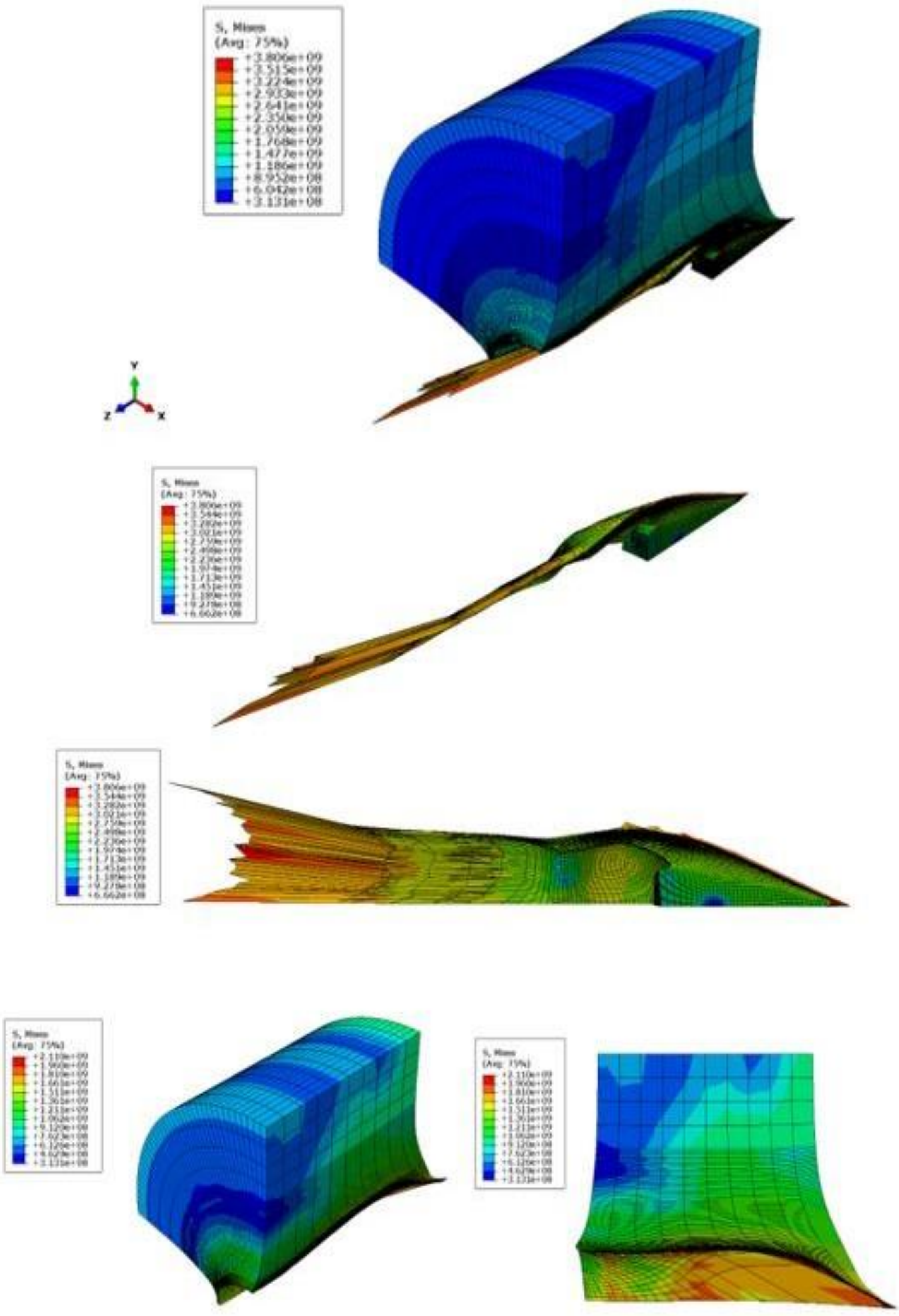

Figure 5.25:Von Mises stress contour generated after WNSY KEP Core and RHA Steel target plate at 2000m/s

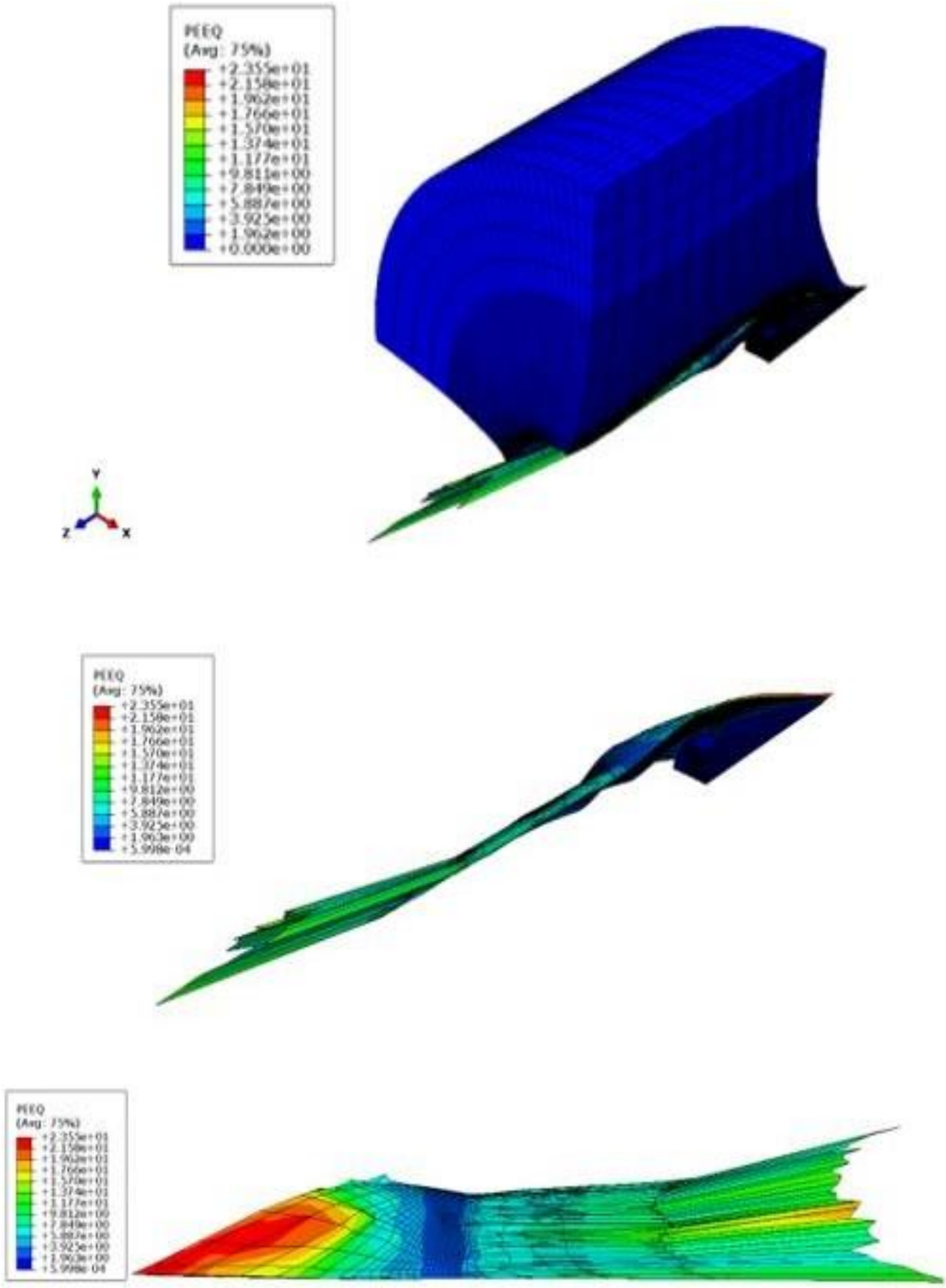

Figure 5.26:Equivalent plastic strain profile after WNSY KEP Core and RHA Target plate at 2000m/s

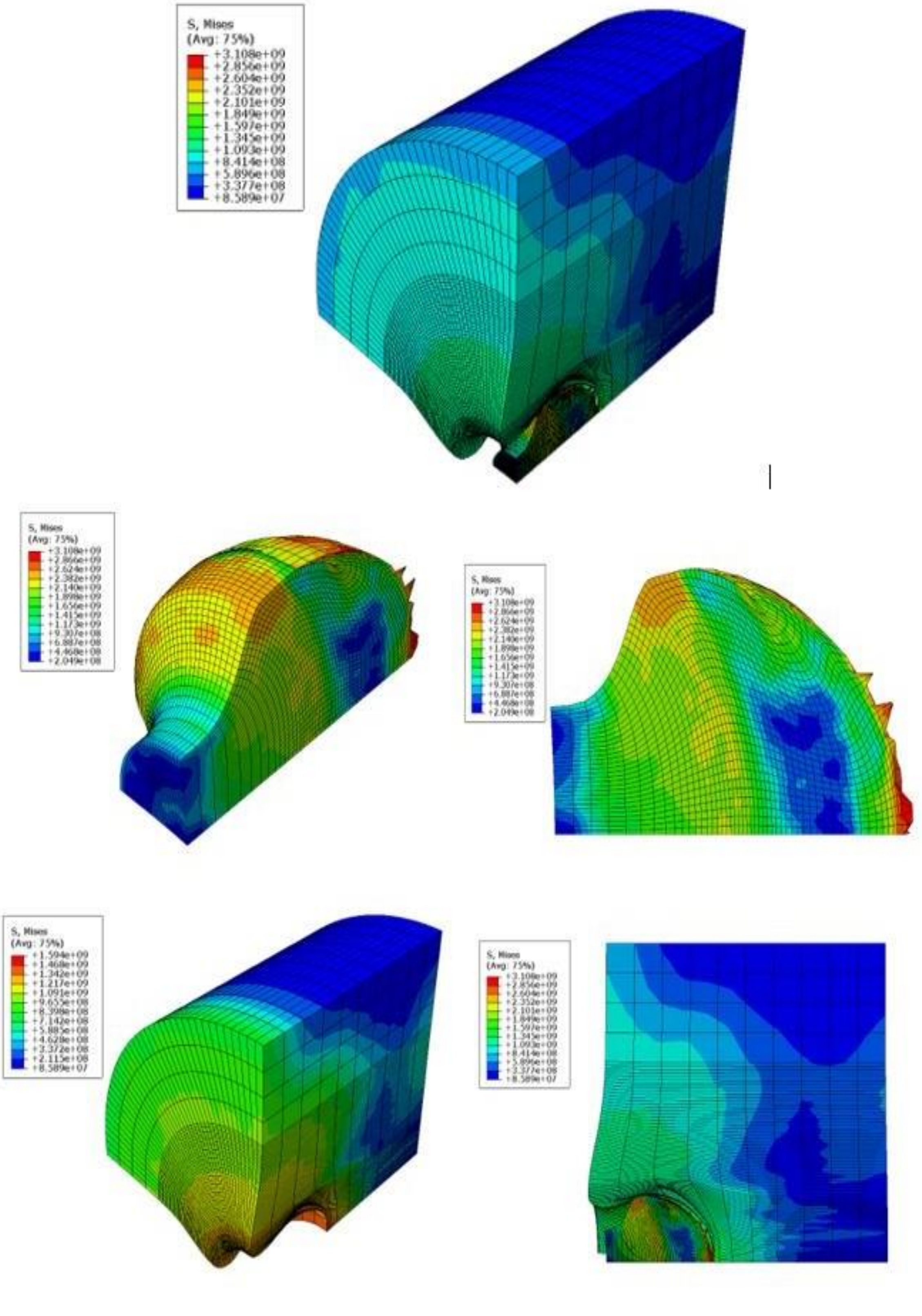

Figure 5.27: Von mises stress contour generated after WNCSY KEP Core and RHA Steel target plate at 1000m/s

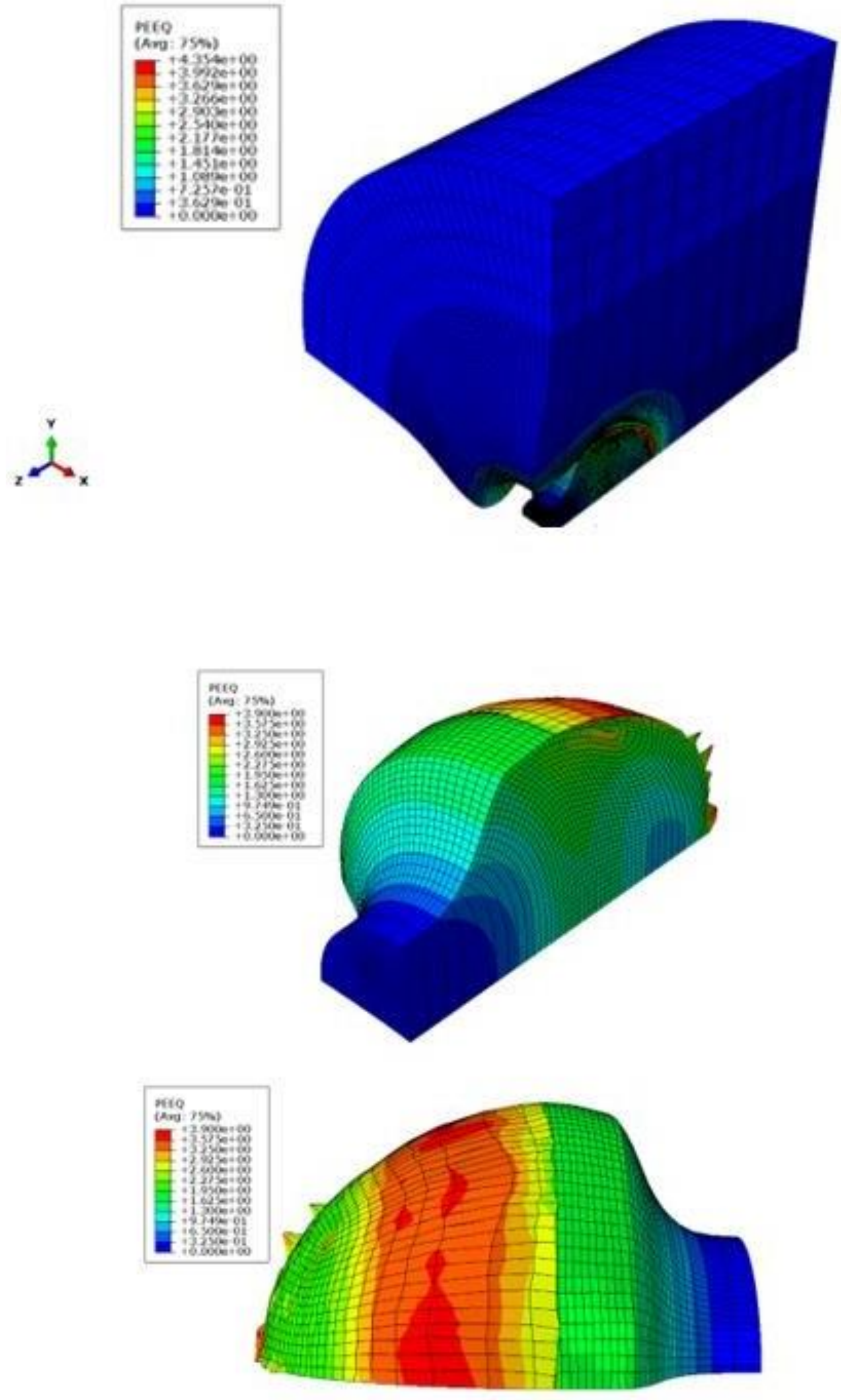

Figure 5.28: Equivalent plastic strain profile after WNCSY KEP Core and RHA Target plate at 1000m/s

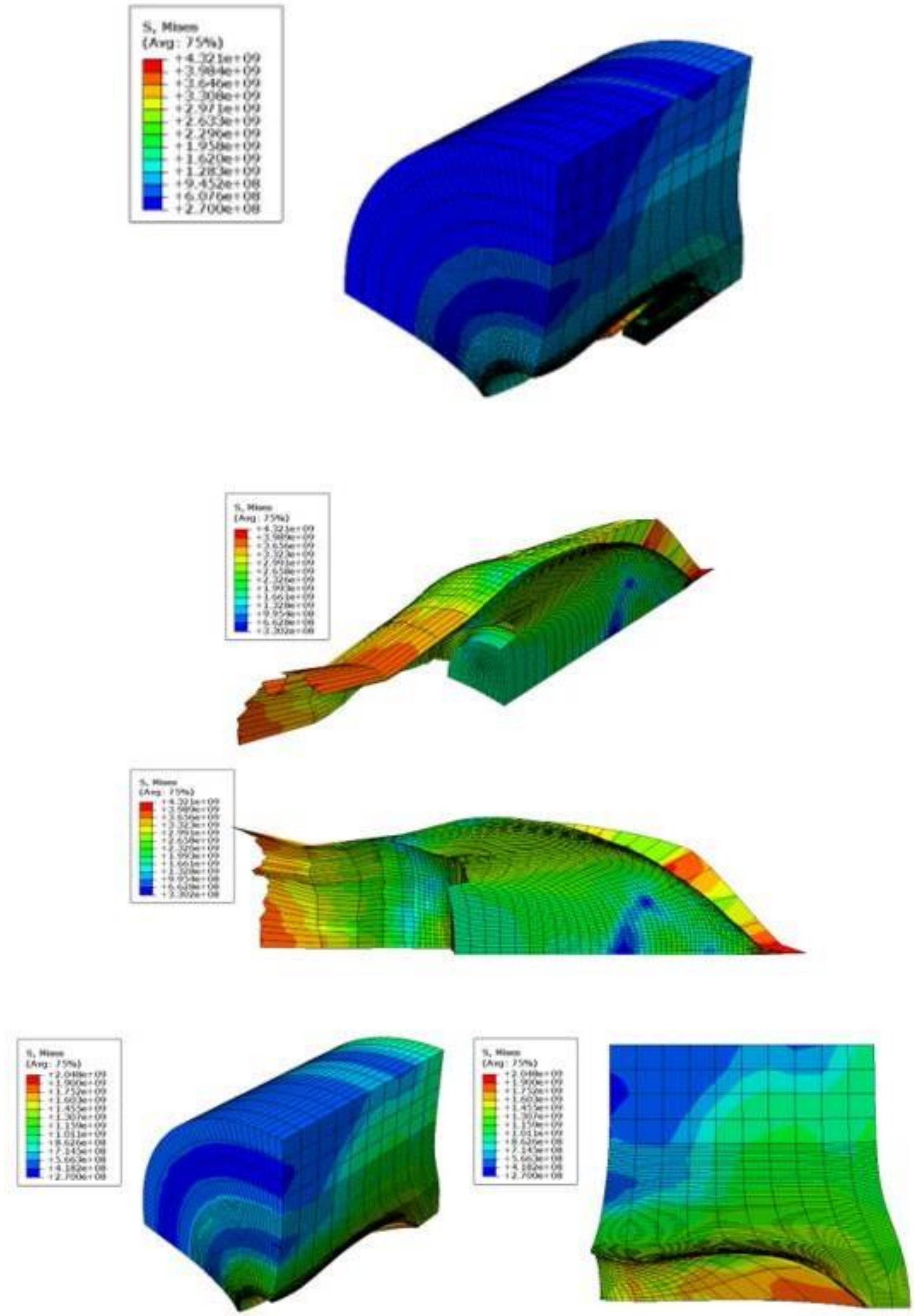

Figure 5.29:Von Mises stress contour generated after WNCSY KEP Core and RHA Steel target plate at 1500m/s

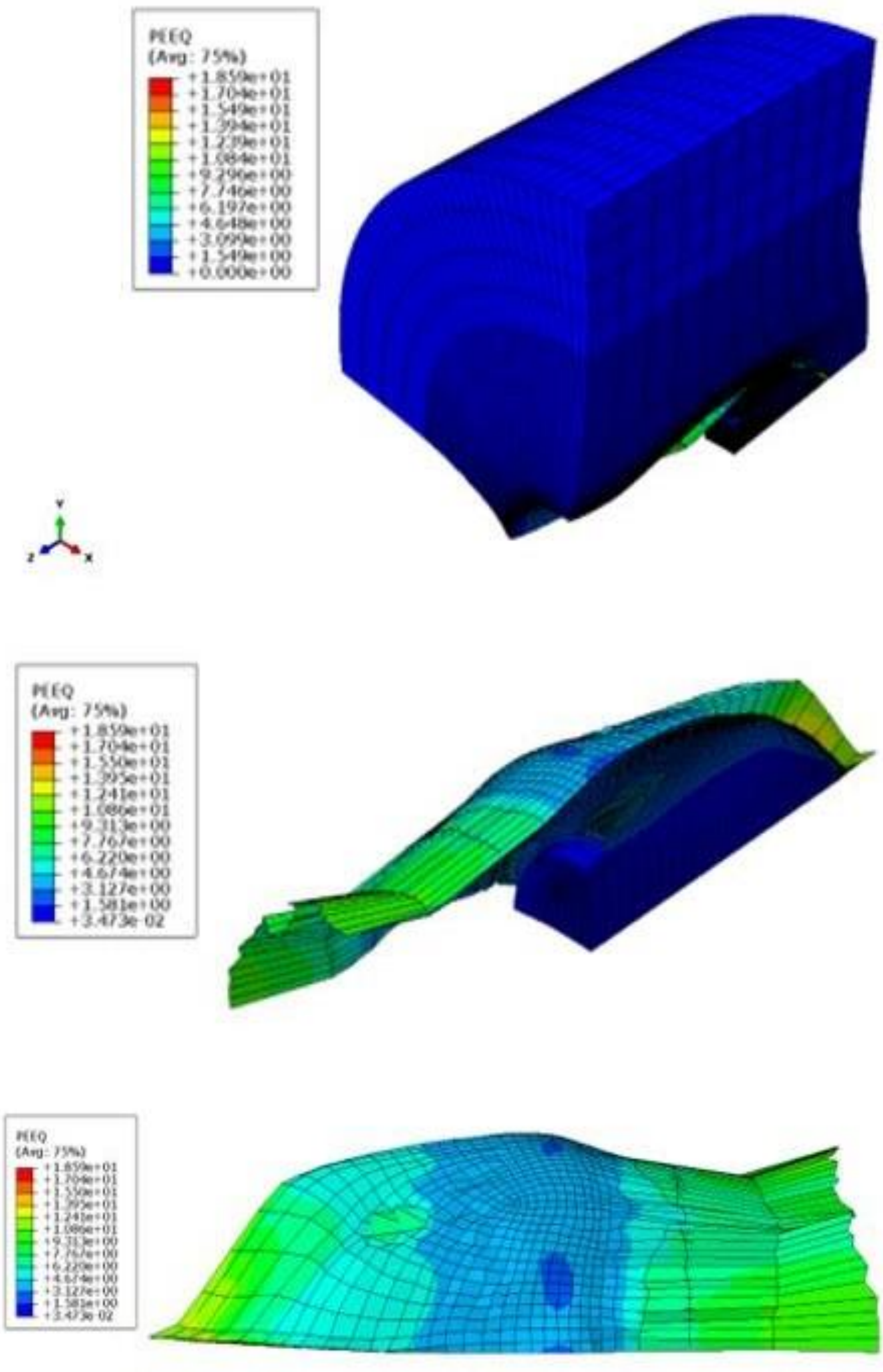

Figure 5.30:Equivalent plastic strain profile after WNCSY KEP Core and RHA Target plate at 1500m/s

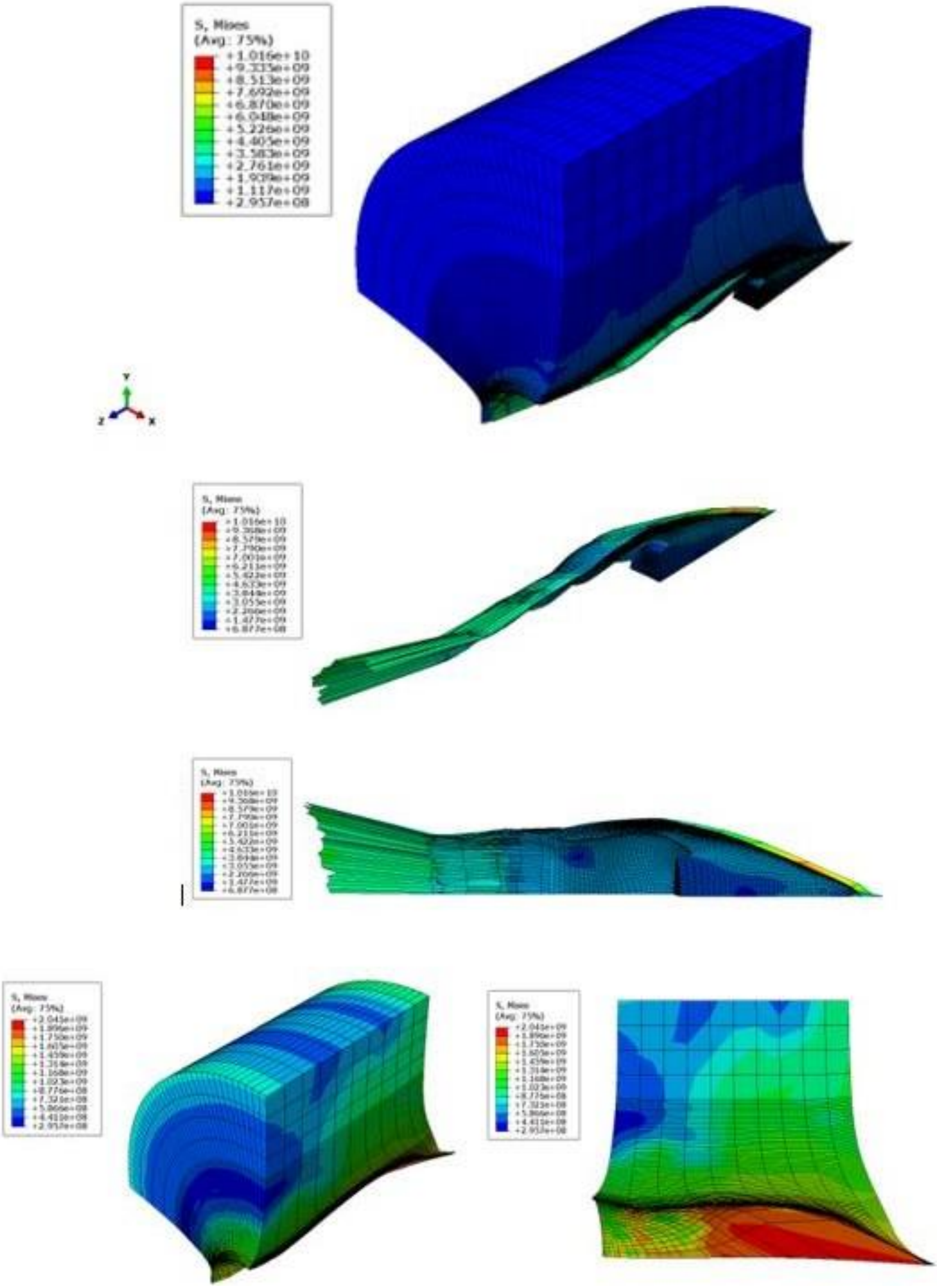

Figure 5.31:Von Mises stress contour generated after WNCSY KEP Core and RHA Steel target plate at 2000m/s

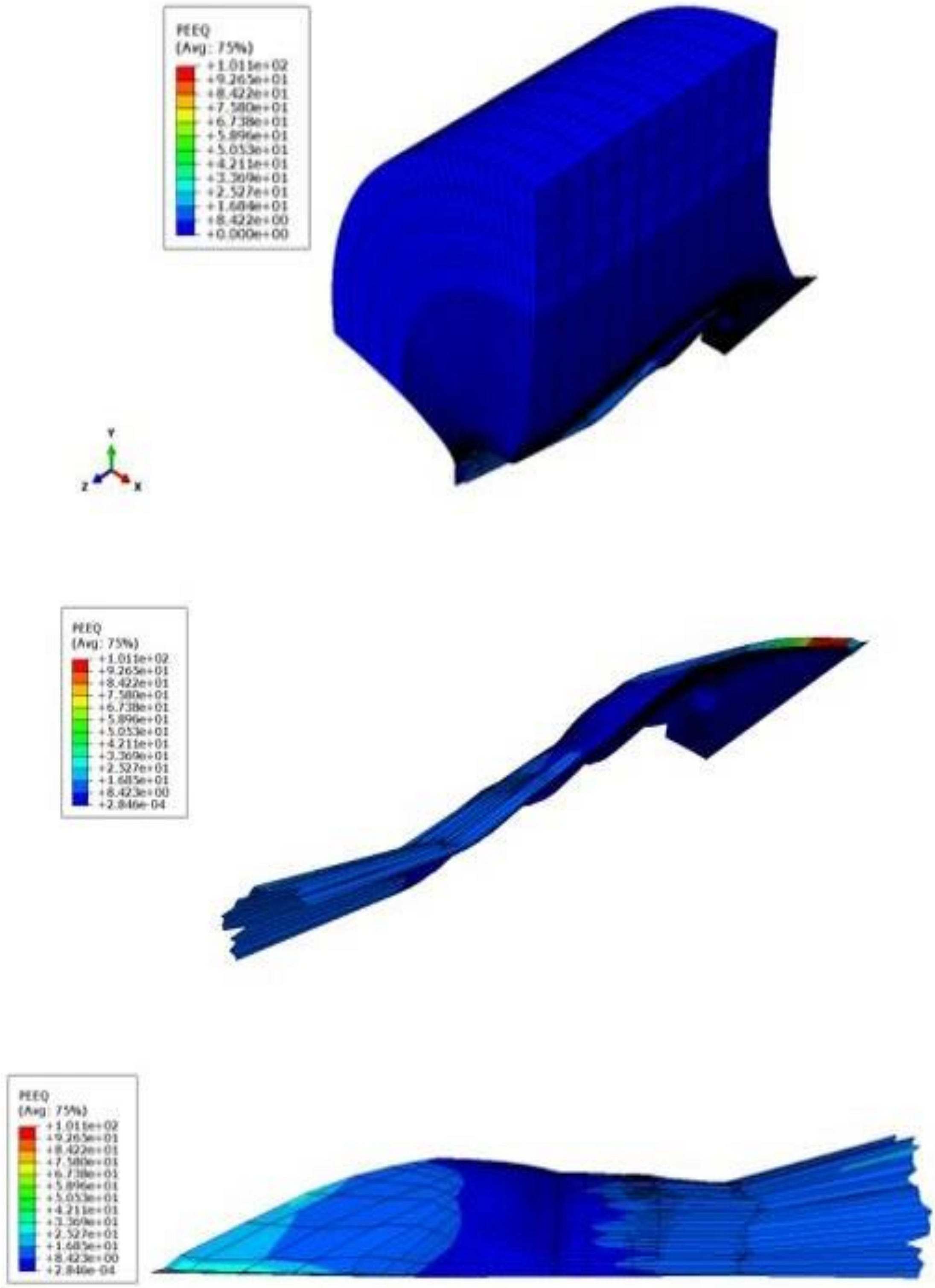

Figure 5.32:Equivalent plastic strain profile after WNCSY KEP Core and RHA Target plate at 2000m/s

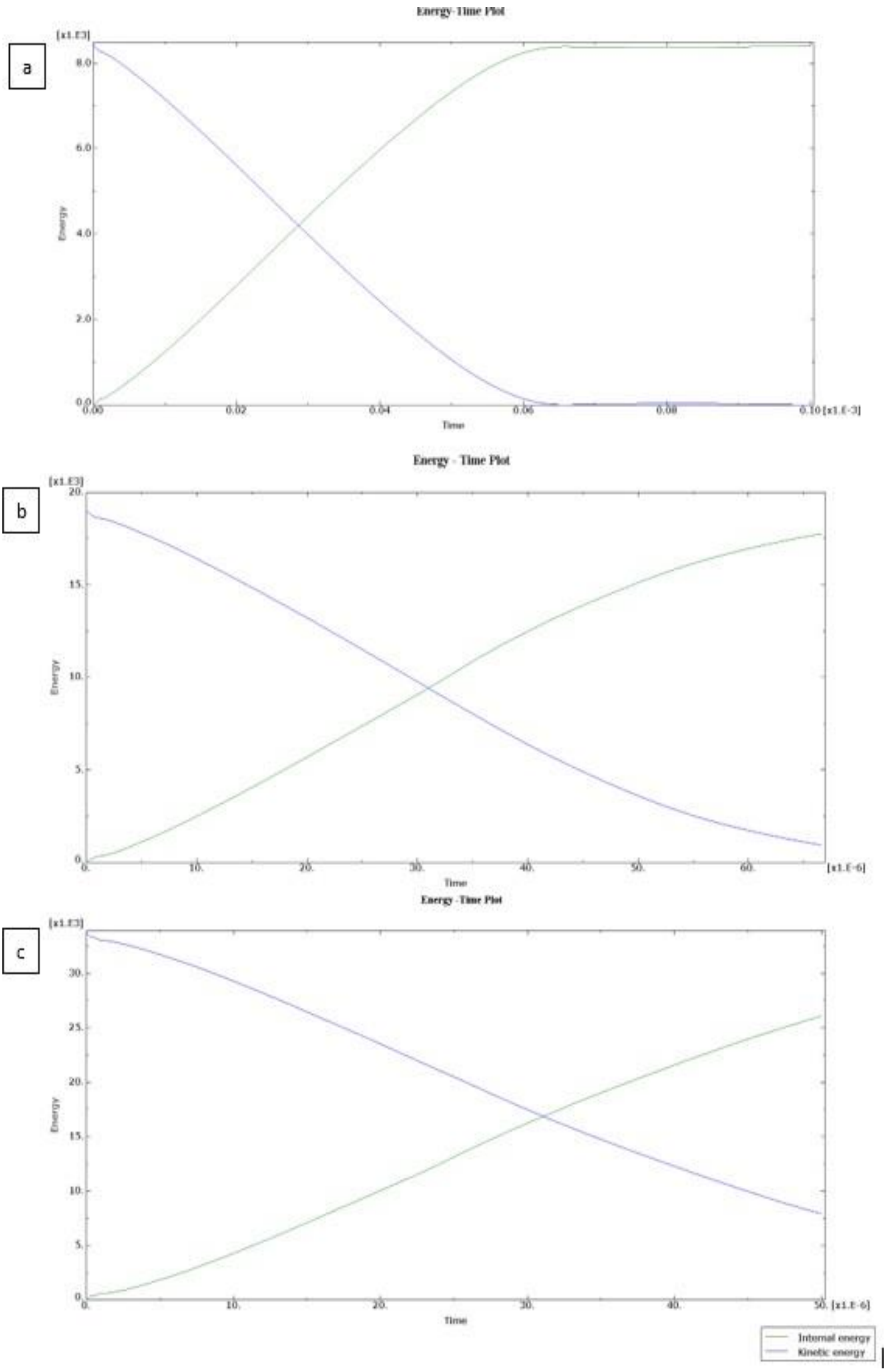

Figure 5.33: Energy-Time plot for WNSY KEP Core and RHA Target plate at - a. 1000m/s, b. 1500m/s, c. 2000m/s

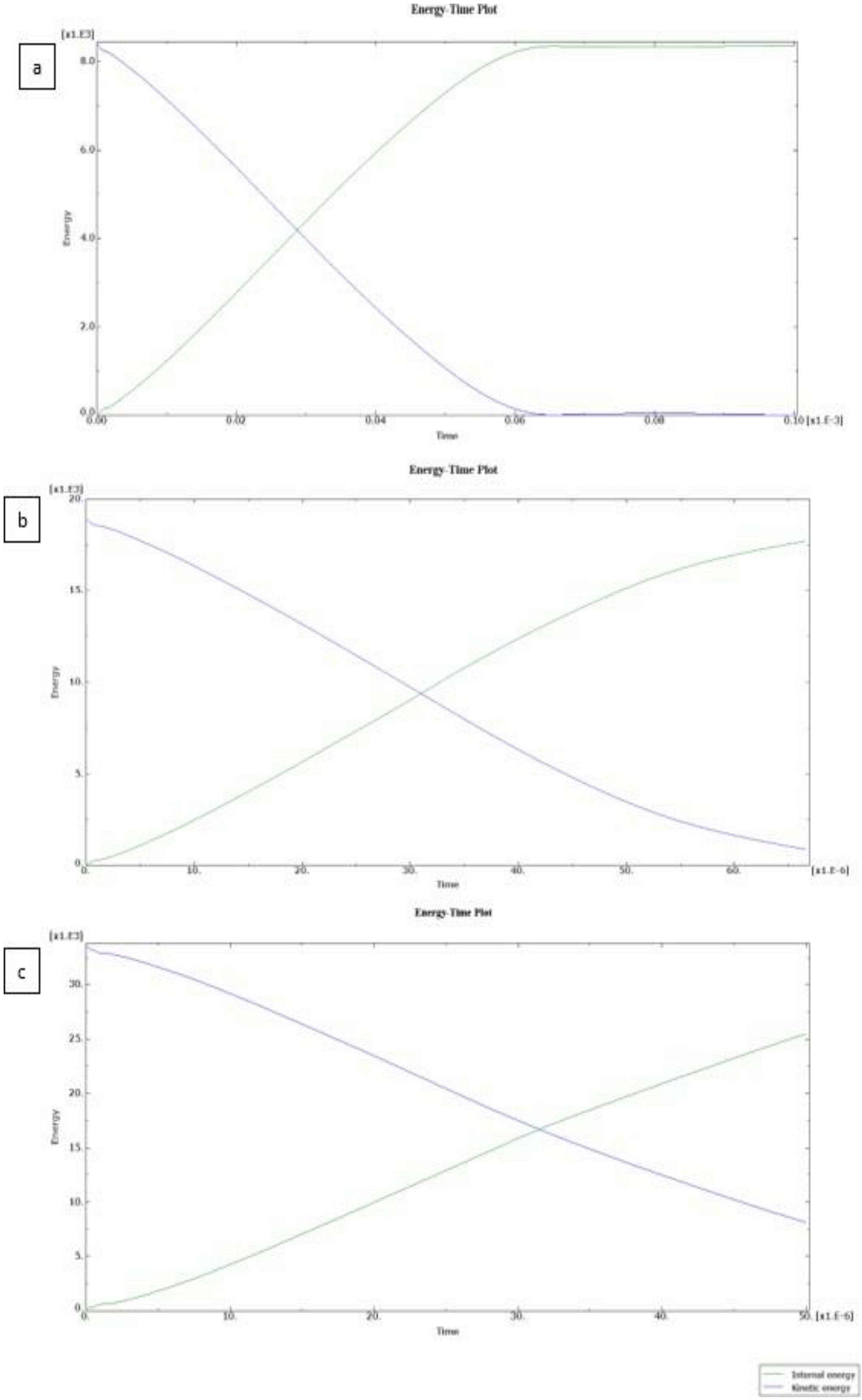

Figure 5.34:Energy-Time plot for WNCSY KEP Core and RHA Target plate at - a. 1000m/s, b. 1500m/s, c. 2000m/s

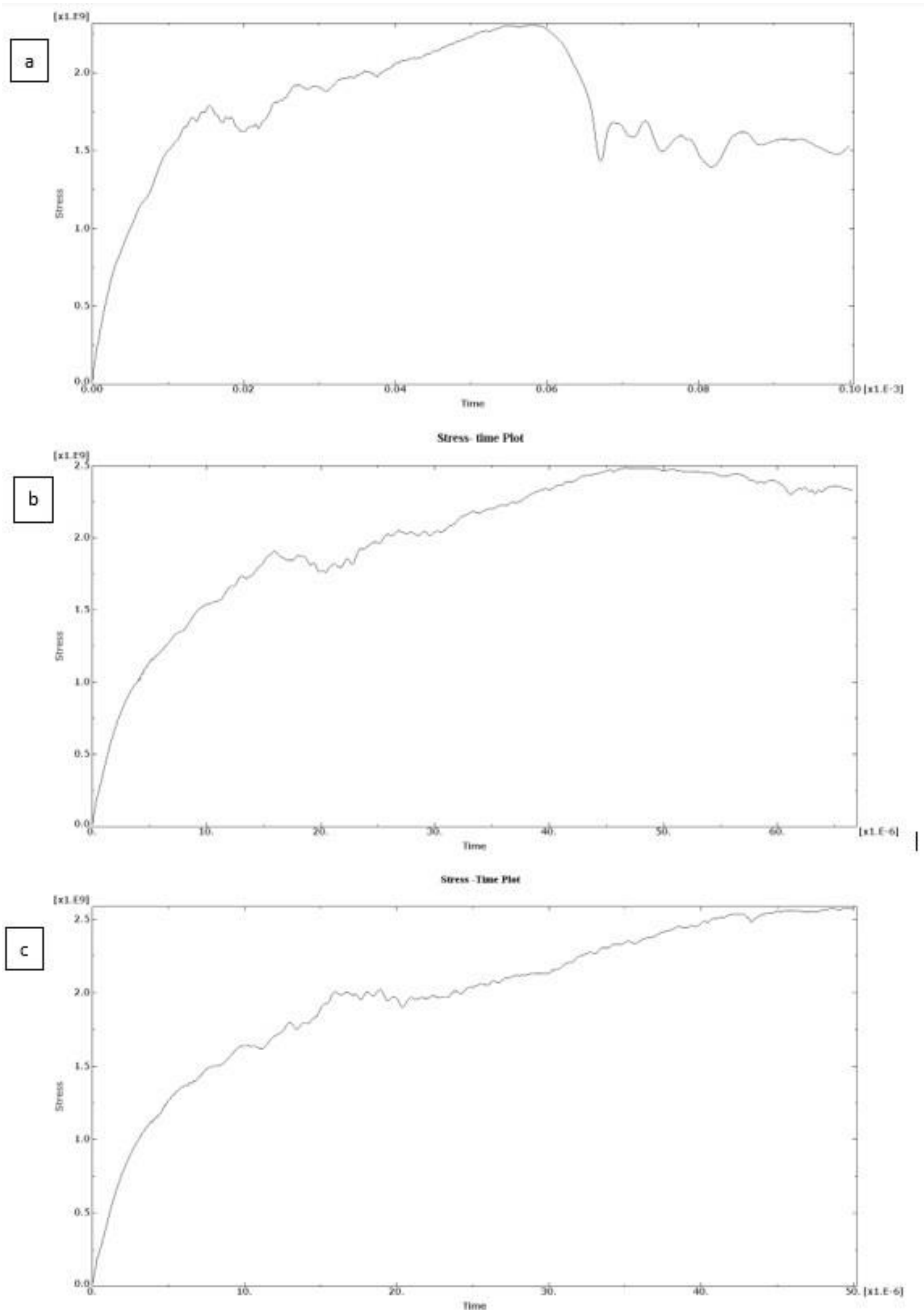

Figure 5.35:Stress(Von mises) (Pa)-Time(sec) plot for WNSY KEP Core and RHA Target plate at - a. 1000m/s, b. 1500m/s, c. 2000m/s

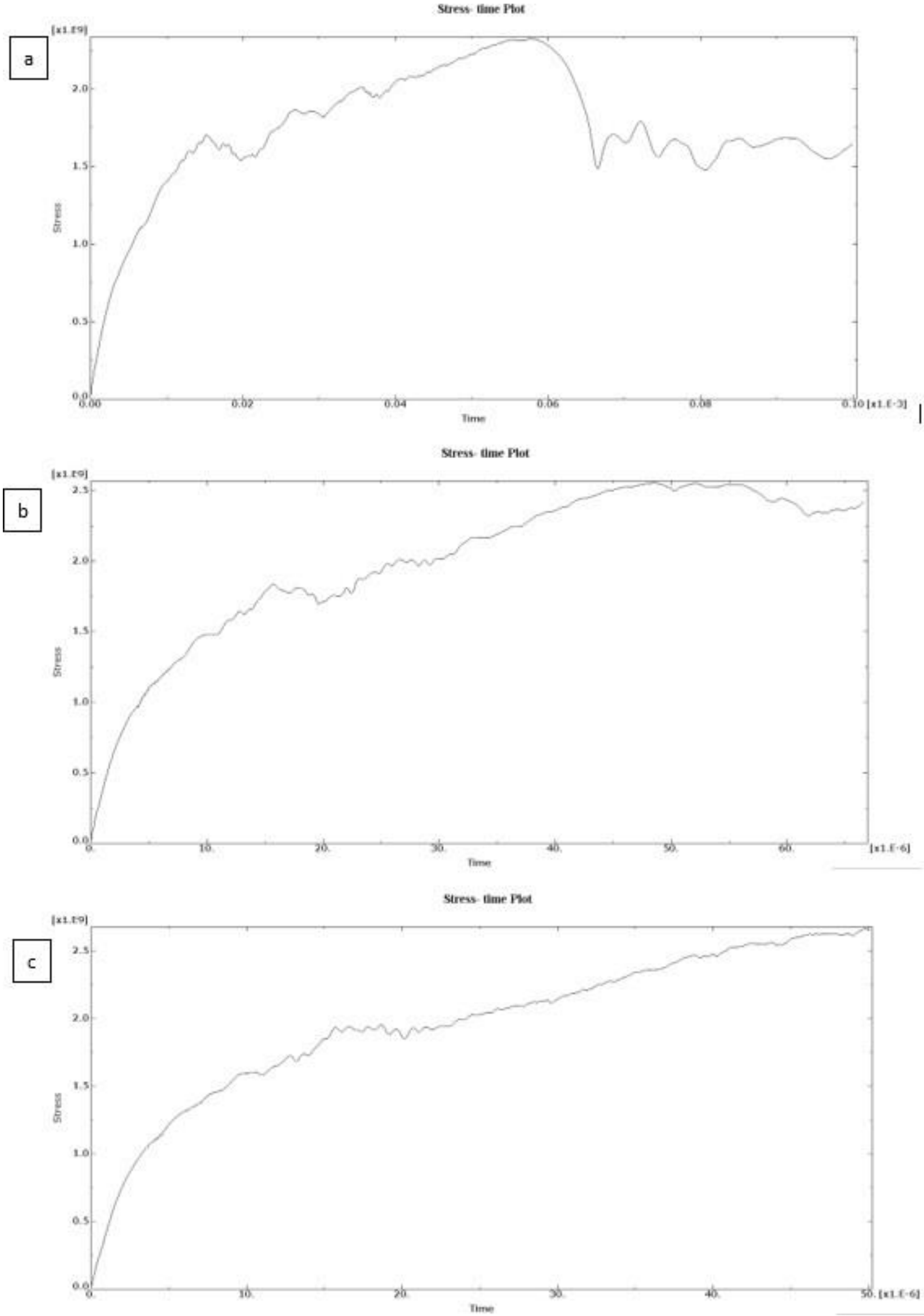

Figure 5.36:Stress(Von mises) (Pa)-Time(sec) plot for WNCSY KEP Core and RHA Target plate at - a. 1000m/s, b. 1500m/s, c. 2000m/s

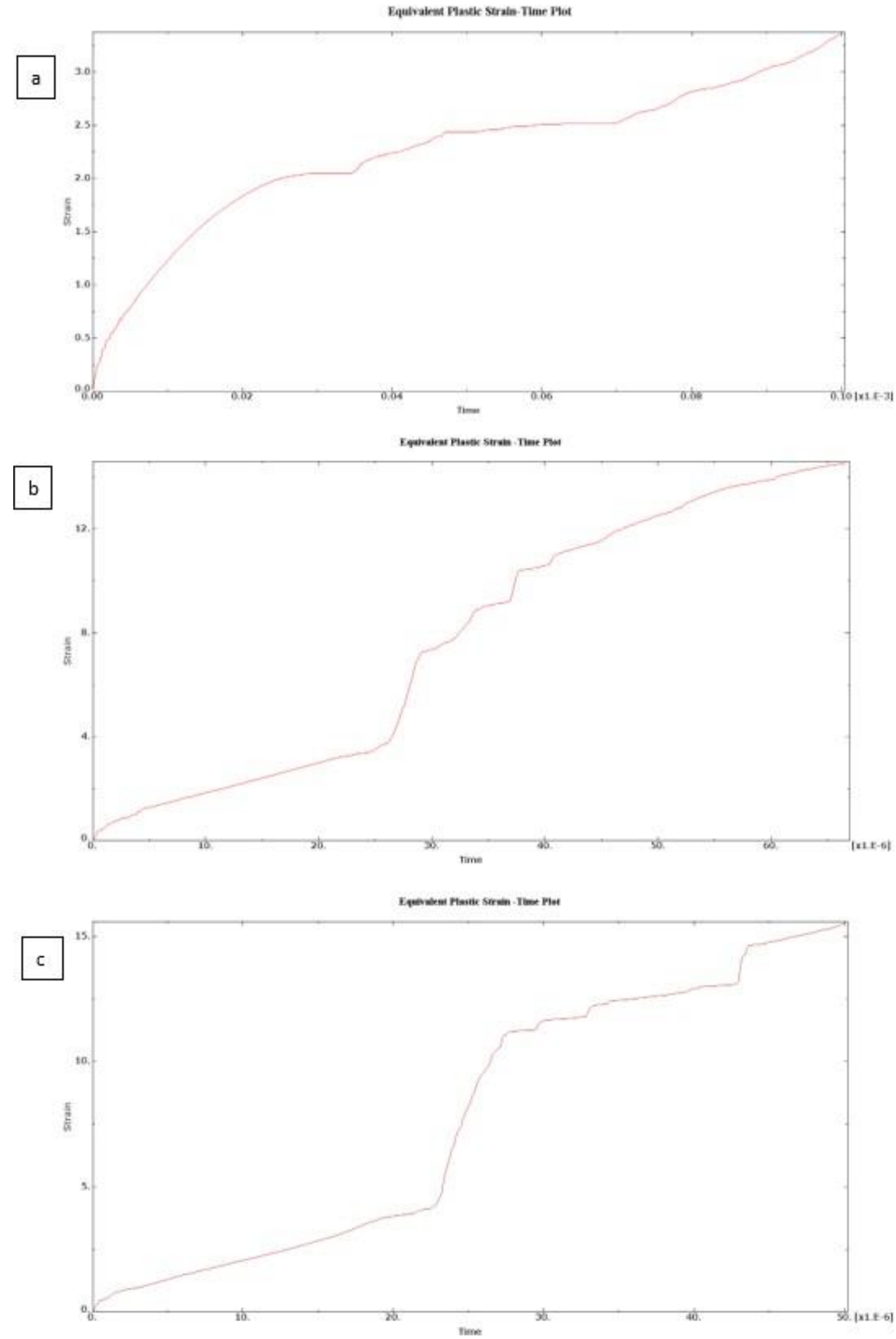

Figure 5.37:Equivalent plastic strain-Time(sec) plot for WNSY KEP Core and RHA Target plate at - a. 1000m/s, b. 1500m/s, c. 2000m/s

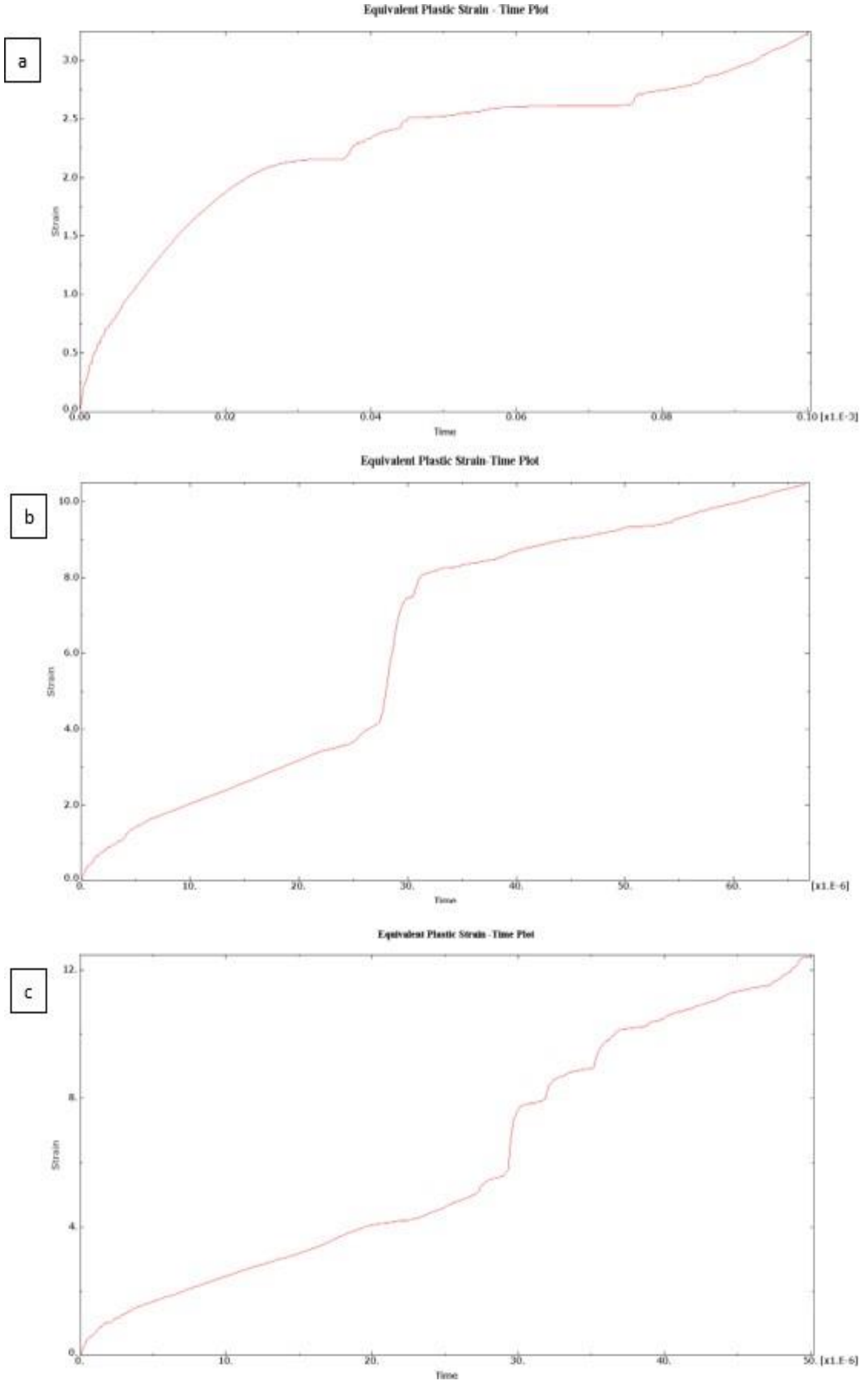

Figure 5.38:Equivalent plastic strain-Time(sec) plot for WNCSY KEP Core and RHA Target plate at - a. 1000m/s, b. 1500m/s, c. 2000m/s

Figures 5.21 and 5.22 show that at 1000 m/s velocity, the head of both KEP cores blunts into a "mushroom" shape after penetration due to the high plasticity of W. Some elements flow backward from the KEP head. The rod head deformation causes a big crater hole in the target plate with a diameter more significant than the rod shaft. The blunted nose increases the rod's resistance, which reduces penetration depth. Conversely, this mushrooming effect has reduced at higher velocities, and a chisel-like shape of the KEP head can be observed.

The energy-time plots in Figures 5.33 and 5.34 indicate that the initial kinetic energy of the KEP is the total energy due to its mass and initial velocity. It is used for deforming the target plate. At 1000m/s, the kinetic energy and the initial rate in the KEP gradually decrease during the penetration, and it remains almost constant after the penetration is completed. The kinetic energy lost in this process is responsible for the rise in the target plate's internal energy, plastic deformation, and perforation. Even the center of the target plate experiences an increase in kinetic energy till crack initiation due to the particles in the target plate being accelerated by the kinetic energy of the KEP. A part of the kinetic energy of the KEP is then spent penetrating the plate. The target plate shows an initial resistance for bending, and this imparts a rise in the internal energy of the KEP to an extent. The internal energy of the plate rises steadily at a higher rate than that of the rod till a crack is initiated. The rate of rising in the internal energy of the KEP due to its work done is almost negligible after the crack initiation.

At 1000m/s, both alloys initially show an increase in stress and then decrease further. Strain increases originally and always are on the higher side because of the plastic deformation.

The penetration performance is evaluated in terms of penetration depth at a given velocity and time and the crater hole radius. At 2000m/s, the KEP cores penetrated entirely through the target plate thickness. A similar trend of penetration depth and crater hole radius was observed for both the alloy cores. But the mushroom head formed during simulations 1 and 4 is not desired. At higher velocities, plastic deformation occurred at lower strains, and hence arrow-like head formation and material fragment separation was observed. But due to material flowing backward, the crater hole radius is large. The observations from the simulations 1-6 are given in table 5.8:

Simulation no.	KEP Core Alloy	Impact Velocity(m/s)	Time (µs)	Depth of penetration (mm)	Crater hole radius (mm)
Simulation 1	WNSY	1000	100	21.3	10
Simulation 2	WNSY	1500	66.6	47	12.2
Simulation 3	WNSY	2000	50	>50	14
Simulation 4	WNCSY	1000	100	20.2	10.1
Simulation 5	WNCSY	1500	66.6	47.8	11.9
Simulation 6	WNCSY	2000	50	>50	15.1

Table 5.8: Penetrating data of WNSY and WNCSY KEP cores

Chapter 6 CONCLUSION

Nanostructured oxide dispersion strengthened tungsten heavy alloys- 98.7W-1Si-0.3Y_2O_3 (WSY), 88.7W-10Ni-1Si-0.3Y_2O_3 (WNSY), and 85.7W-10Ni-3Co-1Si-0.3Y_2O_3 (WNCSY) were fabricated by mechanical alloying and conventional sintering. Microstructural characteristics and quasi-static mechanical properties of these three alloys were analyzed. Dynamic deformation behavior was studied after testing under very high strain rates using a miniature Split Hopkinson Pressure bar test to determine the suitability of the newly developed alloys as kinetic energy penetrator material. All three alloys have very high dynamic compression strength and low failure strain. But the strain rate seems to be either decreasing or constant with increasing strain till fracture. This indicates that no strain localization occurs even at very high strain values, but flow softening is significant. No shear bands or localized strain regions were observed in the SEM micrographs of WSY, WNSY, and WNCSY. From these conclusions, the possibility of adiabatic shear failure in these alloys can be eliminated. The WSY alloy failed at a very low load in the compression test due to a large amount of porosity. Also, Si and Y_2O_3 makes the WSY alloy brittle, while the other two alloys, the Ni and Ni-Co matrix phase, take up the load and deformed significantly.

The Johnson-Cook material and damage model parameters were calculated from the quasi-static compression and SHPB tests at various strain rates. The ballistic impact test was simulated in ABAQUS software at 1000, 1500, and 2000 m/s. The KEP core exhibited mushroom-like head deformation at lower velocity, which is undesirable. At higher velocities, better penetration performance was observed in terms of penetration depth.

Chapter 7 FUTURE SCOPE OF WORK

- The SHPB test was conducted on different strain rates but not at different temperatures. The study neglects the effect of temperature, so the analysis can be performed at various temperatures to analyze the dynamic deformation behavior in a real scenario.
- The ABAQUS simulation was optimized to get the results in less time, so time step data was collected from 1000 intervals. This can be even increased to get precise results and contours.
- The Johnson-Cook material and damage model parameters were manually found from limited data using numerical calculations. The values can be optimized by performing the quasistatic and dynamic compression tests at different conditions and numerical optimization.
- The tungsten heavy alloys were manufactured using a conventional sintering process. But nowadays, Spark Plasma sintering and microwave sintering cost-effectively produce near full-density alloys. So, the study can be extended to samples manufactured through other efficient powder metallurgy techniques.

Special acknowledgment: This work is a part of the following projects:

(i) SERB Project No. ECR/2018/000164

(ii) CSIR Project No. 22 (0842)/20/EMR II

REFERENCES

[1] X. Fang, J. Liu, X. Wang, S. Li, and W. Guo, “Investigation on the penetration performance and ‘self-sharpening’ behavior of the 80W-14Cu-6Zn penetrators.”

[2] A. Upadhyaya, “Processing strategy for consolidating tungsten heavy alloys for ordnance applications,” 2001.

[3] Y. Şahin, “Recent Progress in Processing of Tungsten Heavy Alloys,” *Journal of Powder Technology*, vol. 2014, pp. 1–22, Dec. 2014, DOI: 10.1155/2014/764306.

[4] G. Prabhu, R. Arockia Kumar, and T. K. Nandy, “Effect of yttrium oxide dispersion on the microstructure and properties of tungsten heavy alloys,” *Defence Science Journal*, vol. 68, no. 4, pp. 406–411, Jul. 2018, DOI: 10.14429/dsj.68.12255.

[5] L.S. Magness, “Tungsten and Refractory Metals,” in, vol. 3, A. Bose and R.J. Dowding, Eds. Princeton, NJ: Metal Powder Industries Federation, 1996, pp. 133–144.

[6] V. Suman, R. S. Maurya, M. Debata, and D. Chaira, “Effect of Si addition on phase evolution and microstructure in Y2O3 dispersed tungsten (W) and W-based alloys synthesized via mechanical alloying and consecutive conventional sintering,” *Materials Today Communications*, vol. 31, Jun. 2022, DOI: 10.1016/j.mtcomm.2022.103341.

[7] C. Suryanarayana, “Mechanical alloying and milling.” [Online]. Available: www.elsevier.com/locate/pmatsci

[8] S. Sharma, V. M. Chavan, R. G. Agrawal, R. J. Patel, R. Kapoor, and J. K. Chakravartty, “SPLIT-HOPKINSON PRESSURE BAR: AN EXPERIMENTAL TECHNIQUE FOR HIGH STRAIN RATE TESTS.”

[9] J. Venkatesan, M. A. Iqbal, and V. Madhu, “Experimental and numerical study of the dynamic response of B4C ceramic under uniaxial compression,” *Thin-Walled Structures*, vol. 154, Sep. 2020, DOI: 10.1016/j.tws.2020.106785.

[10] K. T. Ramesh and R. S. Coates, “Microstructural Influences on the Dynamic Response of Tungsten Heavy Alloys.”

[11] D. Kim, S. Lee, H. Jin Ryu, S. Hyung Hong, and J. Noh, “Correlation of Microstructure with Dynamic Deformation Behavior and Penetration Performance of Tungsten Heavy Alloys Fabricated by Mechanical Alloying.”

[12] L.S. Magness, “Tungsten Refractory Metals and Alloys,” in *Tungsten Refractory Metals and Alloys*, vol. 4, Princeton, NJ: Metal Powder Industries Federation, 1998, pp. 41–58.

[13] B. H. Rabin and R. M. German, “Microstructure Effects on Tensile Properties of Tungsten-Nickel-Iron Composites.”

[14] H. C. A. B. R. M. G. J. Lankford, “Tungsten and Tungsten Alloys — Recent Advances,” in *Tungsten and Tungsten Alloys — Recent Advances*, Warrendale, PA: TMS, 1991, pp. 151–161.

[15] S. Park, D. Kim, S. Lee, H. Jin Ryu, and S. Hyung Hong, “Dynamic Deformation Behavior of an Oxide-Dispersed Tungsten Heavy Alloy Fabricated by Mechanical Alloying.”

[16] R. Luo, D. Huang, M. Yang, E. Tang, M. Wang, and L. He, “Penetrating performance and ‘self-sharpening’ behavior of fine-grained tungsten heavy alloy rod penetrators,” *Materials Science and Engineering A*, vol. 675, pp. 262–270, Oct. 2016, DOI: 10.1016/j.msea.2016.08.060.

[17] X. Gong, J. L. Fan, B. Y. Huang, and J. M. Tian, “Microstructure characteristics and a deformation mechanism of fine-grained tungsten heavy alloy under high strain rate compression,” *Materials Science and Engineering A*, vol. 527, no. 29–30, pp. 7565–7570, Nov. 2010, DOI: 10.1016/j.msea.2010.07.102.

[18] D. Kim, S. Lee, H. Jin Ryu, S. Hyung Hong, and J. Noh, “Correlation of Microstructure with Dynamic Deformation Behavior and Penetration Performance of Tungsten Heavy Alloys Fabricated by Mechanical Alloying.”

[19] J. L. Fan *et al.*, “Dynamic failure and adiabatic shear bands in fine-grain 93W-4.9Ni-2.1Fe alloy with Y2O3 addition under lower high-strain-rate (HSR) compression,” *Mechanics of Materials*, vol. 42, no. 1, pp. 24–30, Jan. 2010, DOI: 10.1016/j.mechmat.2009.08.006.

[20] S. Park, D. Kim, S. Lee, H. Jin Ryu, and S. Hyung Hong, “Dynamic Deformation Behavior of an Oxide-Dispersed Tungsten Heavy Alloy Fabricated by Mechanical Alloying.”

[21] H. J. Ryu and S. Cha, “Development of Advanced Oxide Dispersion Strengthened Tungsten Heavy Alloy for Penetrator Application.” [Online]. Available: https://www.researchgate.net/publication/277786142

[22] Z. Xiaoqing, L. Shukui, L. Jinxu, W. Yingchun, and W. Xing, “Self-sharpening behavior during the ballistic impact of the tungsten heavy alloy rod penetrators processed by hot-hydrostatic extrusion and hot torsion,” *Materials Science and Engineering A*, vol. 527, no. 18–19, pp. 4881–4886, Jul. 2010, DOI: 10.1016/j.msea.2010.04.050.

[23] X. Fang, J. Liu, X. Wang, S. Li, and L. Zheng, “Study on improving ‘self-sharpening’ capacity of W-Cu-Zn alloy by the pressureless infiltration method,” *Materials Science and Engineering A*, vol. 607, pp. 454–459, 2014, DOI: 10.1016/j.msea.2014.04.015.

[24] C. E. and B. S. R. Anderson Jr, “Ballistic impact: the status of analytical and numerical modeling.,” *International Journal of Impact Engineering*, vol. 7(1), pp. 9–35, 1988.

[25] N. K. Gupta, M. A. Iqbal, and G. S. Sekhon, “Effect of projectile nose shape, impact velocity and target thickness on deformation behavior of aluminum plates,” *International Journal of Solids and Structures*, vol. 44, no. 10, pp. 3411–3439, May 2007, DOI: 10.1016/J.IJSOLSTR.2006.09.034.

[26] M. A. Iqbal, P. K. Gupta, V. S. Deore, S. K. Tak, G. Tiwari, and N. K. Gupta, “Effect of target span and configuration on the ballistic limit,” *International Journal of Impact Engineering*, vol. 42, pp. 11–24, Apr. 2012, DOI: 10.1016/j.ijimpeng.2011.10.004.

[27] G. Tiwari, M. A. Iqbal, P. K. Gupta, and N. K. Gupta, “The ballistic resistance of thin aluminum plates with varying degrees of fixity along the circumference,” *International Journal of Impact Engineering*, vol. 74, pp. 46–56, Dec. 2014, DOI 10.1016/J.IJIMPENG.2014.01.007.

[28] S. Chocron, C. E. Anderson, D. J. Grosch, and C. H. Popelar, “Impact of the 7.62-mm APM2 projectile against the edge of a metallic target,” 2001.

[29] R. S. J. Corran, P. J. Shadbolt, and C. Ruiz, “Impact loading of plates — An experimental investigation,” *International Journal of Impact Engineering*, vol. 1, no. 1, pp. 3–22, Jan. 1983, DOI: 10.1016/0734-743X(83)90010-6.

[30] G. T. Camacho and M. Ortiz, “Adaptive Lagrangian modeling of ballistic penetration of metallic targets,” *Computer Methods in Applied Mechanics and Engineering*, vol. 142, no. 3–4, pp. 269–301, Mar. 1997, DOI: 10.1016/S0045-7825(96)01134-6.

[31] T. Borvik, M. Langseth, O. S. Hopperstad, and K. A. Malo, “Perforation of 12 mm thick steel plates by 20 mm diameter projectiles with flat, hemispherical and conical noses: Part I: Experimental Study,” *International Journal of Impact Engineering*, vol. 27, no. 1, pp. 19–35, Jan. 2002, DOI: 10.1016/S0734-743X(01)00034-3.

[32] D. K. Francis, W. R. Whittington, W. B. Lawrimore, P. G. Allison, S. A. Turnage, and J. J. Bhattacharyya, “Split Hopkinson Pressure Bar Graphical Analysis Tool,” *Experimental Mechanics*, vol. 57, no. 1, pp. 179–183, Jan. 2017, DOI: 10.1007/s11340-016-0191-9.

[33] Understanding Abaqus/CAE modules, “https://abaqus-docs.mit.edu,” 2017.

[34] B. R. A. S. A. M. U. S. M. A. N. Quratulain, “Design and Analysis of Armour-Piercing Fin-Stabilized Discarding Sabot,” 2020.

[35] H. Kurtaran, M. Buyuk, and A. Eskandarian, “Ballistic impact simulation of GT model vehicle door using finite element method,” *Theoretical and Applied Fracture Mechanics*, vol. 40, no. 2, pp. 113–121, 2003, DOI: 10.1016/S0167-8442(03)00039-9.

[36] G. R. Johnson and W. H. Cook, “A Constitutive Model and data for metals subjected to large strains, high strain rates, and high temperatures.”

[37] M. Murugesan and D. W. Jung, “Johnson cook material and failure model parameters estimation of AISI-1045 medium carbon steel for metal forming applications,” *Materials*, vol. 12, no. 4, Feb. 2019, DOI: 10.3390/ma12040609.

[38] A. Banerjee, S. Dhar, S. Acharyya, D. Datta, and N. Nayak, "Determination of Johnson cook material and failure model constants and numerical modeling of Charpy impact test of aarmorsteel," *Materials Science and Engineering A*, vol. 640, pp. 200–209, Jul. 2015, DOI: 10.1016/j.msea.2015.05.073.

[39] Z. P. Hao, F. F. Ji, Y. H. Fan, and N. N. Zhang, "Failure feature and characterization of material of shear band in cutting Inconel718," *Journal of Manufacturing Processes*, vol. 45, pp. 154–165, Sep. 2019, DOI: 10.1016/j.jmapro.2019.06.016.

[40] H. W. Meyer and D. S. Kleponis, "An Analysis of Parameters for the Johnson-Cook Strength Model for 2-in-Thick Rolled Homogeneous Armor," 2001.